



Effective Power System Control Center Visualization

Final Project Report

Power Systems Engineering Research Center

*A National Science Foundation
Industry/University Cooperative Research Center
since 1996*





Power Systems Engineering Research Center

Effective Power System Control Center Visualization

Final Report

Research Team Members

Thomas. J. Overbye, Project Leader and Esa Rantanen
University of Illinois at Urbana-Champaign

Sakis Meliopoulos and George Cokkinides
Georgia Institute of Technology

Research Team Graduate Students

Charles Davis
Steve Judd
David Savageau
Joseph Tate
University of Illinois at Urbana-
Champaign

George Stefopoulos
Ramiz Alaileh
Abhishek Venkatesh
Evangelos Farantatos
Renge Huang
Georgia Institute of Technology

PSERC Document 08-12

May 2008

Information about this Project

For information about this project contact:

Tom Overbye
University of Illinois at Urbana-Champaign
Department of Electrical and Computer Engineering
1406 W. Green St.
Urbana, IL 61801
Phone: 217 333 4463
Fax: 217 333 1162
Email: overbye@ece.uiuc.edu

Power Systems Engineering Research Center

This is a project report from the Power Systems Engineering Research Center (PSERC). PSERC is a multi-university Center conducting research on challenges facing the electric power industry and educating the next generation of power engineers. More information about PSERC can be found at the Center's website: <http://www.pserc.org>.

For additional information, contact:

Power Systems Engineering Research Center
Arizona State University
577 Engineering Research Center
Box 878606
Tempe, AZ 85287-8606
Phone: 480-965-1643
FAX: 480-965-0745

Notice Concerning Copyright Material

PSERC members are given permission to copy without fee all or part of this publication for internal use if appropriate attribution is given to this document as the source material. This report is available for downloading from the PSERC website.

© 2008 University of Illinois at Urbana-Champaign. All rights reserved.

Acknowledgements

The Power Systems Engineering Research Center (PSERC) sponsored the work described in this final report for PSERC project S-25, *Effective Power System Control Center Visualization*. Some of the work was also supported with supplemental funding provided by Concurrent Technologies Corporation (CTC) under grant 060300023 as part of the U.S. DOE Center for Grid Modernization. The authors acknowledge this support, as well as the support provided by PSERC's industry members, and the support of the National Science Foundation (NSF) under grants NSF EEC-0120153 (University of Illinois at Urbana-Champaign) and EEC-0080012 (Georgia Institute of Technology) received under the NSF Industry/University Cooperative Research Center Program. The authors also thank the PSERC Industry Advisory Board (IAB) members who served as project advisors.

The authors wish to recognize their postdoctoral researchers, programmers, and graduate students that contributed to the research and creation of the reports: Matt Davis, Steve Judd, David Savageau, John Sivier and Zeb Tate at the University of Illinois at Urbana-Champaign; and George Stefopoulos, Ramiz Alaileh, Apurva Mohan, Renge Huang, Abhishek Venkatesh, Evangelos Farantatos and George Cokkinides at the Georgia Institute of Technology.

Any opinions, findings, and conclusions or recommendations expressed in this publication are those of the authors and do not necessarily reflect the views of any of the sponsoring agencies or any other entity.

Executive Summary

Visualization of power system conditions can help power system operators maintain adequate situational awareness. This project's purpose was to perform research to increase the effectiveness of power system visualizations, with a particular emphasis on visualization used in the control center environment. Six areas where specific research accomplishments were attained in this project include:

- A new power system visualization approach, known as geographic data views, to provide better visualizations for use during operator initiated power system control and for engineering analysis
- Two new approaches to reduce the time needed to produce power system contours
- A technique for using phasor measurement unit (PMU) data to determine status changes of devices such as transmission lines and generators
- Direct visualization of the voltage angle information being provided by PMUs
- Insight and analysis on the human factors aspects of power system visualization
- Use and visualization of GPS synchronized data for power system stability assessment.

Each of these accomplishments is briefly described below.

1. A new power system visualization approach, known as geographic data views, to provide better visualizations for use during operator initiated power system control and for engineering analysis

The first accomplishment of the project was the development of geographic data views (GDVs) to dynamically show wide-area power system information. The idea behind GDVs is to create power system visualizations “on-the-fly” by combining information derived from a power system model with geographic information that is embedded within the power system model. The resultant visualizations usually contain graphical symbols to represent power system quantities, with the location of the graphical symbols determined from the embedded geographic information. Typically one or more symbol attributes are dependent upon the values for the underlying power system data.

2. Two new approaches to reduce the time needed to produce power system contours

Currently one of the most numerically intensive aspects of modern power system control center visualizations is the display of contours, usually for bus-based values. The first approach uses the concept of creating a unique influence distance for each data point (e.g., a bus-based value such as voltage magnitude). The distance is based on a specified closest number of buses, instead of previous methods that use the same influence distance for each bus. Significant speed improvements are possible by a factor of five in some situations, often with improved pictorial quality of the resultant contours. The second approach takes advantage of the highly parallel structure of the graphics processing unit (i.e., the display card) to significantly speed up an existing algorithm. Prototype results with contouring speeds of up to 30 frames per second were demonstrated.

3. A technique for using PMU data to determine status changes of devices such as transmission lines and generators

The increased deployment of PMUs in the power grid has led to a significant increase in a new type of data available to power system operators. To make sense of this new data, and to use it to increase situational awareness, new analysis techniques need to be developed. A new algorithm was developed to use this data to detect single-line outages based on voltage and current phasor angles obtained from PMUs. The algorithm accurately detected a line outage that occurred on the TVA system based on data obtained from TVA's PMUs.

4. Direct visualization of the voltage angle information being provided by PMUs

Currently the ratio of PMU buses to buses without PMUs is quite small. This presents a challenge because there is no way to estimate the entire system state with these limited data. One way of handling this challenge is to reduce the system to an equivalent system consisting entirely of PMU buses. After the system reduction, the voltage angles may be displayed directly or the differences may be displayed. Displaying differences is useful in a wide-area because it alerts operators that something has changed. It is also possible to use the equivalent system to convert the angles into injections. This is useful because injections are easier to interpret than angles. To demonstrate the equivalent system approach, a test case was developed using power flow cases from the August 14, 2003 blackout.

5. Insight and analysis on the human factors aspects of power system visualization

Human factors analyses were used to evaluate a correct generation control tool with geographic data views. They were also used to develop a prototype demonstrator display that incorporated key human factors principles in its design. The main challenge in design of wide-area power system displays is the mapping of a large number of relevant system variables into a limited number of graphical variables on the visual display. We approached this problem by surveying operators on the most important variables they need to see, and by reviewing research literature for guidelines and principles for display design. We also performed a detailed task analysis of solving line overloads using the highly automated solver tool that we developed. These systems were evaluated by a modified human factors checklist as well as by interviews of several experienced reliability coordinators at the TVA Regional Operations Center. The results indicated that the systems did not need much improvement. These results were carefully documented with suggestions for future upgrades. Specifications for and user comments on the prototype display were also documented.

6. Use and visualization of GPS synchronized data for power system stability assessment

GPS synchronized data can be used for monitoring system stability. Of particular interest in this project was enabling an operator to quickly determine the loss of synchronism of individual generators using direct visualization of PMU data along with monitoring the total energy of the system. This approach requires streaming data from PMUs and real-time data processing to extract the true dynamic system state. The SuperCalibrator approach was adopted to filter the streaming data from GPS synchronized equipment using a high fidelity dynamic state estimator. Using our approach, the dynamic system state can be calculated at each substation independently without requiring remote information. This avoids the complication of communications and transmitting data from other parts of the system. Time latencies are limited to local communications only.

Table of Contents

1.0	Introduction.....	1
2.0	Geographic Data Views	3
2.1	The Need for Geographic Data Views.....	3
2.2	Overview of Geographic Data Views	5
2.3	GDV Implementation.....	8
2.4	Application of GDVs to the Line Overload Problem	14
3.0	Improved Power System Contouring.....	23
3.1	Contouring Basics.....	23
3.1.1	Shepard's Method	24
3.1.2	Mapping Virtual Values Into A Color Scheme.....	25
3.2	Influence Distance	26
3.3	Adaptive Influence Region Algorithm.....	28
3.4	Adaptive Algorithm Testing	30
3.4.1	Experimental Setup.....	30
3.4.2	Contouring Time – Theoretical Results.....	30
3.4.3	Contouring Times – Experimental Results	32
3.4.4	Contouring Images.....	35
3.5	GPU-based Contouring.....	38
3.5.1	Advantage and disadvantages of GPU contouring	38
3.5.2	Preliminary results	39
4.0	Line Outage Detection Using PMU Data	40
4.1	Problem Formulation and Theory	40
4.2	Line Outage Detection Algorithm	43
4.3	Test Case.....	44
4.4	Future Work	47
5.0	PMU Voltage Angle Visualization	49
5.1	Problem Overview	49
5.2	Equivalent Circuit Theory.....	49
5.3	Difference Contours.....	55
5.4	Blackout Case Results.....	55
5.5	Conclusions.....	58
5.6	Future Work	58
6.0	Human Factors Testing.....	59
6.1	Human factors challenges in display design.....	59
6.2	Human factors principles in display design	60
6.2.1	Basic display design principles.....	61
6.2.2	Design principles for the use of color in visual displays	62
6.2.3	Ecological interface design principles.....	63
6.3	Evaluation of Line Overload Correction Form (LOCF).....	65
6.3.1	Task analysis.....	65
6.3.2	Display evaluation	68
6.4	Design of the prototype display.....	72
6.4.1	Specifications for a Prototype Wide-Area Power Transmission Display	73
6.4.2	Future Directions	74

7.0	Utilization and Visualization of GPS-synchronized Data for Stability Monitoring	75
7.1	Method Description	76
7.2	Generating Substation State Estimation.....	77
7.3	Description of the Dynamic State Estimator	80
7.4	Implementation	81
7.5	Applications	82
7.5.1	Stability Monitoring.....	82
7.5.2	Out of Step Relaying.....	85
8.0	Conclusion	91
Appendix A:	Basic Problem in Dynamic State Estimation	92
A.1	Description of the transmission line model	92
A.2	States definition and Measurements definition.....	93
A.3	Estimation model	94
Appendix B:	Triangulation Methods for Visualization of Power System Data	97
B.1	Rendering the IsoSurface.....	100
B.2	Delaunay Triangulation	100
B.3	Data Structure used for the insertion algorithm.....	102
B.4	Finding the triangle containing the new inserted point (see Figure B.8).....	104
B.5	Inserting the new point into an existing triangle.....	104
B.6	Flipping an edge of the triangle	105
B.7	Butterfly Subdivision	105
B.8	Smoothing	107
Project Publications	108
References	109

List of Figures

Figure 2.1: TVA Regional Operations Center Display.....	3
Figure 2.2: Eastern Interconnect One-Line Diagram.....	4
Figure 2.3: GDV of Eastern Interconnect Operating Areas with Size Proportional to Area Generation.....	6
Figure 2.4: Display with Rectangle Color Based on Area Interchange.....	7
Figure 2.5: Substation Case Information Display Showing Entergy, Southern and TVA Generation Substations (intentionally blurred for data confidentiality)	8
Figure 2.6: Geographic Data View Customization Dialog, Common Options Page.....	9
Figure 2.7: Geographic Data View Customization Dialog, Class/Field Options Page	10
Figure 2.8: A Default Geographic Data View Showing the 163 Generation Substations	10
Figure 2.9: Geographic Data View Customization Dialog, First Field Formatting Page.....	11
Figure 2.10: Visualization with Size Proportional to Substation Generation.....	12
Figure 2.11: Geographic Data View Customization Dialog, Second Field Formatting Page	13
Figure 2.12: Visualization with Fill Color Proportional to Generator Q/P Ratio	13
Figure 2.13: Visualization with Fill Color Proportional to Reactive Reserves	14
Figure 2.14: Visualization of Available Generation in TVA Footprint Using Kites (intentionally blurred for data confidentiality)	15
Figure 2.15: One-line Diagram Showing Overloaded Transmission Line (intentionally blurred for data confidentiality).....	16
Figure 2.16: Line Overload Correction Form (LOCF) Showing Text-Based Option (intentionally blurred for data confidentiality)	17
Figure 2.17: Line Flow Correction Dialog (intentionally blurred for data confidentiality)	18
Figure 2.18: Proposed Line Corrections Portion of LOCF (intentionally blurred for data confidentiality).....	19
Figure 2.19: LOCF After Changes (intentionally blurred for data confidentiality)	20
Figure 2.20: Line Overload Correction Form (LOCF) Showing GDV Option (intentionally blurred).....	21
Figure 3.1: Virtual Value Calculation.....	24
Figure 3.2: Color Mapping for Red = High, Blue = Low	25
Figure 3.3: Ten-Color Discrete Scale	26
Figure 3.4: Bus Influence Distance.....	27
Figure 3.5: Zoom Level vs. Time for $g = \infty$, $\beta_0 = 75\%$	34
Figure 3.6: Contour with $g = \infty$	35
Figure 3.7: Contour with $g = 5$	36
Figure 3.8: Contour with $g = 10$	36
Figure 3.9: Contour with $g = 30$	37
Figure 3.10: Contour with $g = 60$	37
Figure 3.11: GPU-Based Contouring for 37 Bus System.....	39
Figure 4.1: Normalized Angle Difference	42
Figure 4.2: Voltage Phasor Angles at PMU Buses.....	45
Figure 4.3: Voltage Phasor Angles at PMU Buses, Filtered.....	46
Figure 5.1: 7-bus sample case.....	51
Figure 5.2: 7-bus sample case row contour	52
Figure 5.3: Large case row contour	53

Figure 5.4: 7-bus sample case row contour	54
Figure 5.5: Large case row contour	54
Figure 5.6: 7-bus injection contours	55
Figure 5.7: 7-bus injection difference contours	56
Figure 5.8: August 14, 2003 Blackout Case 1 - 15:05 to 15:00 difference	56
Figure 5.9: August 14, 2003 Blackout Case 2 - 15:45 to 15:05 difference	57
Figure 5.10: August 14, 2003 Blackout Case 3 - 15:45 to 16:05 difference	58
Figure 6.1: Illustration of display design problem.....	59
Figure 6.2: Line overload indications	72
Figure 6.3: Prototype Wide Area Display.....	74
Figure 7.1: Inputs and Outputs of the Super-Calibrator as Dynamic State Estimator	77
Figure 7.2: Breaker-Oriented Three-Phase Generating Substation Model.....	78
Figure 7.3: Conceptual Illustration of the SuperCalibrator	82
Figure 7.4: Visualization of Generator Real Time State.....	83
Figure 7.5: 3-D Visualization of System Phase Angles during a Transient Swing	83
Figure 7.6: 3-D Visualization of System Voltage Magnitude During a Transient Swing	84
Figure 7.7: 2-D Visualization of Generator Operating Point and Potential Energy	85
Figure 7.8: Test System Illustration.....	85
Figure 7.9: Total and potential system energy-stable case	88
Figure 7.10: Total and potential system energy-unstable case	88
Figure 7.11: Test System Total Energy Trajectory.....	89
Figure 7.12: Visualization and Comparison of the Impedance Trajectory	90
Figure A.1: The Transmission Line Model.....	92
Figure B.1: Bounded Butterfly subdivision	97
Figure B.2: Delaunay Triangulation of Points.....	98
Figure B.3: After Bounded Butterfly subdivision and Smoothing	98
Figure B.4: 3D Iso-Surface with 8 levels.....	99
Figure B.5: Flat Iso-Surface with 8 levels	99
Figure B.6: Inserting points one-by-one	101
Figure B.7: Delaunay Triangulation - Inserting points.....	102
Figure B.8: Corner Table operations	103
Figure B.9: Traversing the triangle mesh	104
Figure B.10: Inserting a point in an existing triangle	105
Figure B.11: Flipping a triangle edge using the corner table operators.....	105
Figure B.12: Butterfly subdivision	106
Figure B.13: Butterfly Mask	106
Figure B.14: Example butterfly subdivision.....	106

List of Tables

Table 3.1: Timing Data for $\beta_0 = 50\%$ of Allowable Range	32
Table 3.2: Timing Data at Zoom Level = 10%	33
Table 3.3: Timing Data for $\beta_0 = 75\%$ of Allowable Range	33
Table 3.4: Average Time Comparison for Zoom Level = 30%	34
Table 3.5: Worst Case Time Comparison for Zoom Level = 30%	34
Table 4.1: Algorithm Results Using All Phasor Angles	46
Table 4.2: Algorithm results using reduced phasor angle set	47
Table 4.3: Algorithm results using all phasor angles, without line cut-off checks	47
Table 6.1 Ranking of power systems variables	60
Table 7.1: Applications and Required Accuracy	76
Table 7.2: List of Measurements	79
Table 7.3: Test System Parameters	86
Table 7.4: Generators' Torque Angles & Speeds at Fault Clearing time	87

Effective Power System Control Center Visualization

1.0 Introduction

The research effort described in this report deals with useful visualization of large amounts of real time data. Electric power systems are characterized by large amounts of data. The general goal of this project is to continue the development of innovative methods to assist players in the electricity industry to extract and visualize usable information from this large set of power system data, with a particular emphasis on control room applications. Previous projects resulted in the developments of useful visualizations. In particular, UIUC and Georgia Tech were both involved in the previous PSERC project, “Visualization of Power Systems and Components” (S18, which began in June 2002 and finished in May 2005). Under the previous project, The Georgia Tech team developed visualization engines for complex components of electric power systems including HVDC components, transformers, generators, etc. A unique characteristic of that work was to be able to monitor not only the electric performance of a component but also the thermal performance of a component. These visualizations are important for monitoring the thermal loading of components in real time and therefore provide useful information to operators. This work has been extended in this project to provide more in-depth visualizations. In particular in this project we focused on monitoring the effect of component loading and transients on the stability of the system. The visualization of the system stability is assisted by the presence of GPS synchronized measurements in the system.

The work under this project was separated in several subtasks which were allocated to the University of Illinois and Georgia Tech. The work in the University of Illinois focuses on determining what information needs to be visualized using a method known in the human factors domain as Cognitive Task Analysis (CTA) and then on the development of system-level visualizations. CTA is a very effective technique for determining a wealth of information about operators’ strategies and decisions associated with the performance of various tasks. In addition the issue of visualizing critical information as well the reactive power support of the system has been addressed. The results of this work and all related developments are presented in the first part of the work. The Georgia Tech team focused on the use of GPS-synchronized data, filtered or unfiltered, for visualization of system oscillations/swings, visualization and animation of the motion of generators and monitoring the stability of the system.

GPS-synchronized data, filtered or unfiltered, provide new dimensions and opportunities for visualization of system oscillations/swings, visualization and animation of transient stability indicators and possibly characterizing the swings as stable/unstable. We have investigated the utilization of data streams that are becoming available from projects such as the EIPP (Eastern Interconnection Phasor Project) and data from relays that are GPS-synchronized in addition to the standard SCADA data. The task of developing meaningful visualizations of system swings and transient stability indicators is very difficult because of two reasons: (a) the data throughput and refresh frequency is quite high generating the issue of response time, and (b) meaningful indicators of transient stability require substantial computational processing of raw data before meaningful visualizations can occur. For example PMU data provide streaming data of phasors and therefore of phase angles. It is well known that phase angles alone do not provide useful information about the transient stability of the system. We propose the following approaches for the purpose of developing meaningful visualizations of transient stability indicators and system swings. First, it is important that the data be filtered from error and inconsistencies. Since the

application is real time, we propose to experiment filtering the data with local state estimators that will operate on a model consisting of a generator under consideration and the circuits to the next substation. The state estimation filtered GPS-synchronized data will provide the phasors of the voltages, the frequency of the waveforms and the rate of frequency change. This information will be useful in the visualizations. Second, we will build on previous visualizations of phase angles that have been developed in S18 to somehow include the rate of change of phase angles (frequency) so that the operator can visualize the speed by which system conditions are changing. These visualizations should be 3-D and it will require substantial experimentation for becoming effective in conveying the information. Thirdly, we propose to utilize ideas developed in out of step relaying for developing visualizations of transient stability indicators. Specifically, out of step relays include logic that decides whether a system oscillation/swing is going to be stable or unstable. The advantage of this approach is that it requires only local information which is used to trace the movement of the impedance trajectory. We propose to mimic various out of step relays and develop visualizations of the logic output. One idea for these visualizations is to represent the generator as a mass suspended by an elastic string that stretches and compresses as the apparent impedance changes, it changes colors as the impedance enters the out of step relay blinders and “breaks” when the out of step relay trips. Finally, we also propose to use energy function ideas for developing visualizations of transient stability indicators. The local state estimator approach to filter the data fits very well with this idea. Specifically, using the results of the local state estimator, energy functions can be defined for each generator, i.e. kinetic energy, potential energy or total energy. One potential method for visualizing these energy functions will be a 3-D surface plot. Methodologies for determining stability regions will be reviewed and applied. The information from these analyses could be potentially added to the visualization graphs, for example regions of instability can be colored red, etc. This approach in itself is a difficult research project without well established and proven methods. It will be very interesting to try this approach and see how successful it will be. It is important to note that there is another proposed project to use PMU data for the purpose of determining transient stability. The approach there is to use pre-simulated results and identify the operational point by interpolating real time measurements into pre-simulated results. It is expected that if both projects are approved, the results from one project will be useful to the other project and vice versa.

The report is organized as follows. Chapter 2 presents a new power system visualization approach, known as geographic data views, that was developed for this project with the goal of providing better visualization for operator initiated power system control. Chapter 3 discusses how the performance on an existing visualization technique, contouring, can be substantially improved. Chapters 4 and 5 then focus on the use of PMU data, with Chapter 4 discussing how PMU data can be used to determine power system device status, while Chapter 5 focuses on the use of voltage phase angles. In Chapter 6 the results from the human factor evaluation are given. Finally, Chapter 7 presents our work in the use of GPS-synchronized data. Please note, in order to maintain confidentiality of the actual electric system data used with this project, the results presented a number of Figures has been deliberately blurred (Figures 2.5, 2.14, 2.15, 2.16, 2.18, 2.19, and 2.20).

2.0 Geographic Data Views

Over the last decade or so there have been tremendous advances in the area of power system visualization. For example, prior to the year 2000 in practically all power system control centers operational quantities, such as power flows and voltages were represented either as analog fields on substation one-line displays or as numeric fields on tabular displays. Dynamic display of system information was quite limited, such as the use of dashed lines to represent device status and font color for limit violations. An overview of the system had only been available on a static map board with the only dynamic data shown using different colored lights.

However since 2000 many power system control centers have adopted more advanced visualization techniques, particularly for wide-area displays. For example, now the use of color contours to show voltage magnitude variation across large regions is common. Animated arrows may be used to show line flow direction, while dynamically sized pie charts are used to indicate which transmission lines and transformers are close to or are exceeding their limits, or are out-of-service. A more detailed discussion of these techniques are provided in [1] and [2]. Figure 2.1 shows a wide-area display used at the TVA Regional Operations center.



Figure 2.1: TVA Regional Operations Center Display

2.1 The Need for Geographic Data Views

Typically such wide-area displays are based upon a predefined graphical one-line format. The use of these techniques on predefined displays can be particularly effective for power system monitoring. Being geographically-based they can rapidly provide system operators and engineers with an overview of current system conditions, letting them quickly focus on problem areas.

Since the displays are predefined, they also have the advantage of providing a consistent and known view of the system. Panning and zooming can be used to provide more detail as needed.

However, when the task switches from monitoring to corrective control or analysis one potential short-coming of this approach is it can be quite difficult to design a priori a single display, or even a set of displays, that contains all the information needed to make effective, corrective control decisions. For example, consider the common application of generation re-dispatch to remove a line overload, either for an actual violation or for a contingent violation. The two most important pieces of information for deciding which generators to change are 1) their control sensitivity with respect to the overloaded line, and 2) their effective real power (MW) control range. While one could design a display to show this information (indeed Figure 10 of [2] shows the use of control sensitivity contours), it would be difficult to construct beforehand since it requires the simultaneous display of sensitivity information that is device dependent, along with generator MW control ranges. Also, showing this information on an existing display designed for system monitoring could result in slow display performance and a more cluttered appearance.

The need to extend the power system visualization methodology for engineering analysis also became apparent as a result of this project. This occurred during the development of the human factors test cases discussed in Chapter 6. The starting point for the development of these cases was a 43,000 bus MMWG power flow case of the entire Eastern Interconnect along with a one-line diagram showing the 161 kV and higher voltage transmission system (shown in Figure 2.2). Overall the one-line contained more than 7100 buses and about 9500 transmission lines and transformers. Such a one-line could have been quite useful if one were simply interested in seeing which lines were overloaded, or with producing voltage contours.

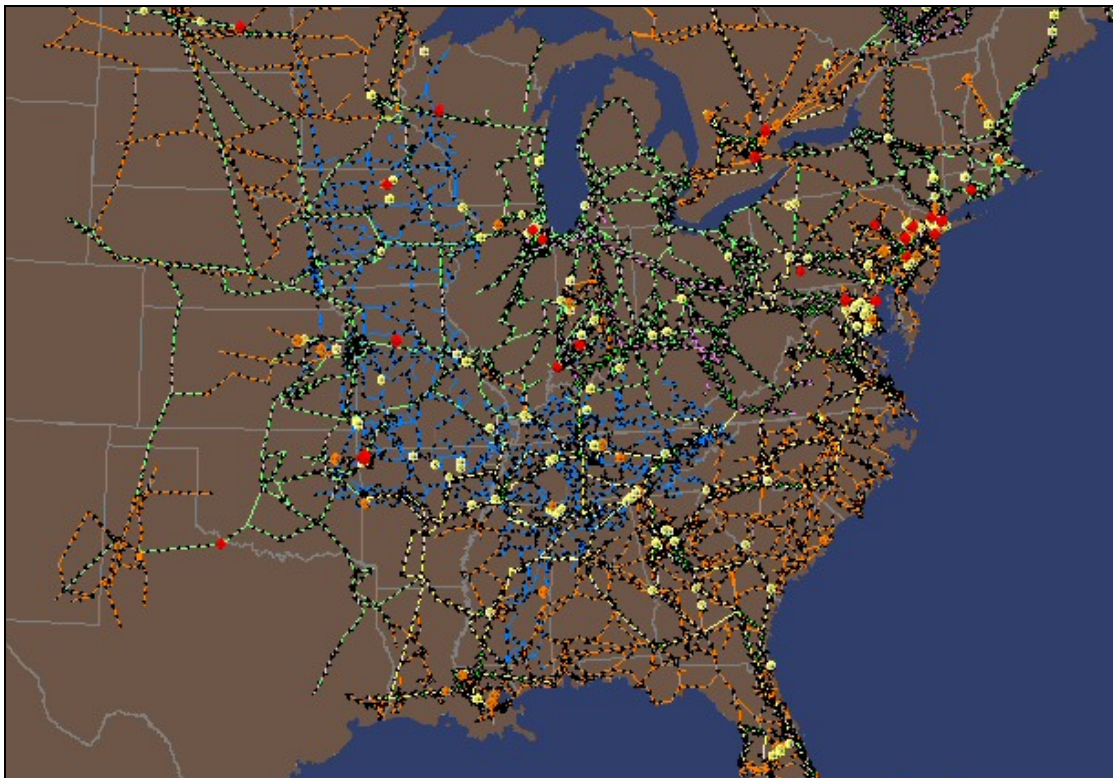


Figure 2.2: Eastern Interconnect One-Line Diagram

However, the design goal for the development of the test cases was to create a much smaller equivalent case, centered on TVA, with a strong north to south power flow pattern. Therefore it was necessary to both determine which nearby areas should be retained and which more distant ones should be deleted, and to visualize the importing and exporting areas in order to create the desired power flow pattern. For this task the one-line was much less useful.

The epiphany moment in the development of the concept that became known as geographic data views was the recognition that while the Figure 2.2 one-line did not show the desired information, the one-line, along with the underlying power system model, did contain the necessary information. The trick was to provide a way of dynamically extracting it, a technique known as geographic data views (GDVs).

2.2 Overview of Geographic Data Views

The idea behind GDV displays is to dynamically create power system visualizations by combining information derived from a power system model with geographic information that is embedded within the power system model. The resultant visualizations usually contain graphical symbols to represent power system quantities, with the location of the graphical symbols determined from the embedded geographic information. Typically one or more symbol attributes are dependent upon the values for the underlying power system data. Example attributes include size, color, rotation, and shape.

The key to an effective GDV implementation is to allow the dynamic displays to be easily customized to display the desired power system quantities. For wide-area visualizations the most important geographic information will be the bus locations, or at least the locations of the substations containing the buses. Once the location of the buses (or their substations) are known, the location of some other objects, such as operating areas can be estimated. Transmission lines could be dynamically drawn either by embedding the actual coordinates for the lines with the model, or by approximately their paths just from the location of their terminal buses. Depending upon the application, geographic display information about the location of devices modeled within a substation, such as generators, switched shunts, and loads, could either be stored explicitly, or just default to their bus's location. Simple overlap avoidance algorithms could be used to avoid overlapping display symbols.

To illustrate the GDV approach, again consider the Figure 2.2 case, in which the initial design goal was the creation of a smaller equivalent system, centered on TVA. This was to be accomplished by retaining all the buses in some electrical areas, and equivalencing all the buses in others. Overall the model had 144 areas, some with well known names like NYISO that easily denoted their geographic location, but also with many that were quite cryptic such as SETH, a name that was not geographically helpful. Some contained large amounts of generation and load, while for others the amounts were quite small. The power system model contained information about the operating areas themselves, such as their names and what buses they contained. From the list of buses an area's electric characteristics, such as total generation, load and interchange could be easily determined.

In order to create the GDVs the power system model was augmented to assign every bus to a substation, and then to provide each substation with a geographic location. While this step obviously takes a significant amount of work, it is a step that only needs to be done once in its entirety since substations do not move. Furthermore, if a detailed one-line diagram is available, substation geographic coordinates can be automatically determined from the one-line. With all the data in place, a GDV can be created "on-the-fly." Figure 2.3 shows a GDV in which cyan

colored rectangles are used to show the location of the various operating areas from the Figure 2.2 case, with the size of each rectangle proportional to the area's total generation. Black text is centered on each symbol is used to show the area's name. For this example the geographic location of each rectangle was determined by a simple averaging of the locations for the area's buses. To provide a geographic context, the rectangles are shown superimposed upon a map of the US state boundaries. However, the point of emphasis about GDVs is that they can literally be created from scratch within seconds. This allows for quick visual display of almost any power system data. Also, by combining different graphical element attributes multi-attribute visualizations are possible. For example, Figure 2.4 extends the Figure 2.3 GDV by making the rectangle color dependent upon the area's interchange, with blue shades corresponding to exporting areas, and red importing areas.

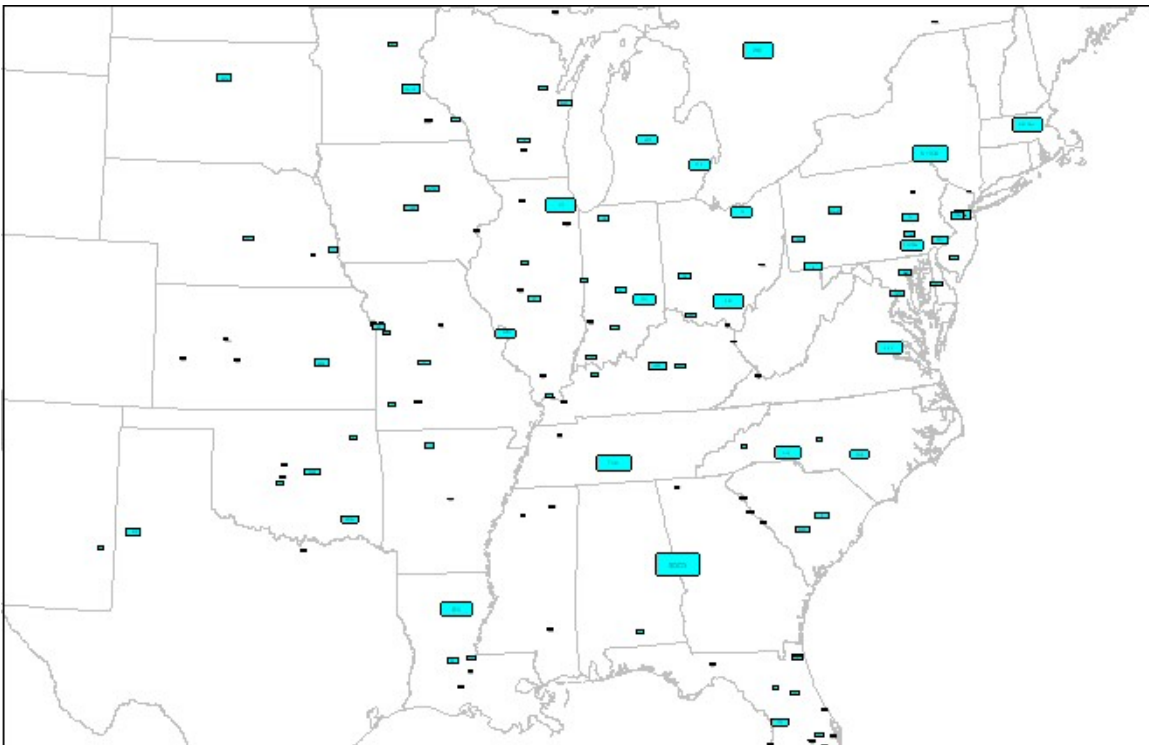


**Figure 2.3: GDV of Eastern Interconnect Operating Areas
with Size Proportional to Area Generation**

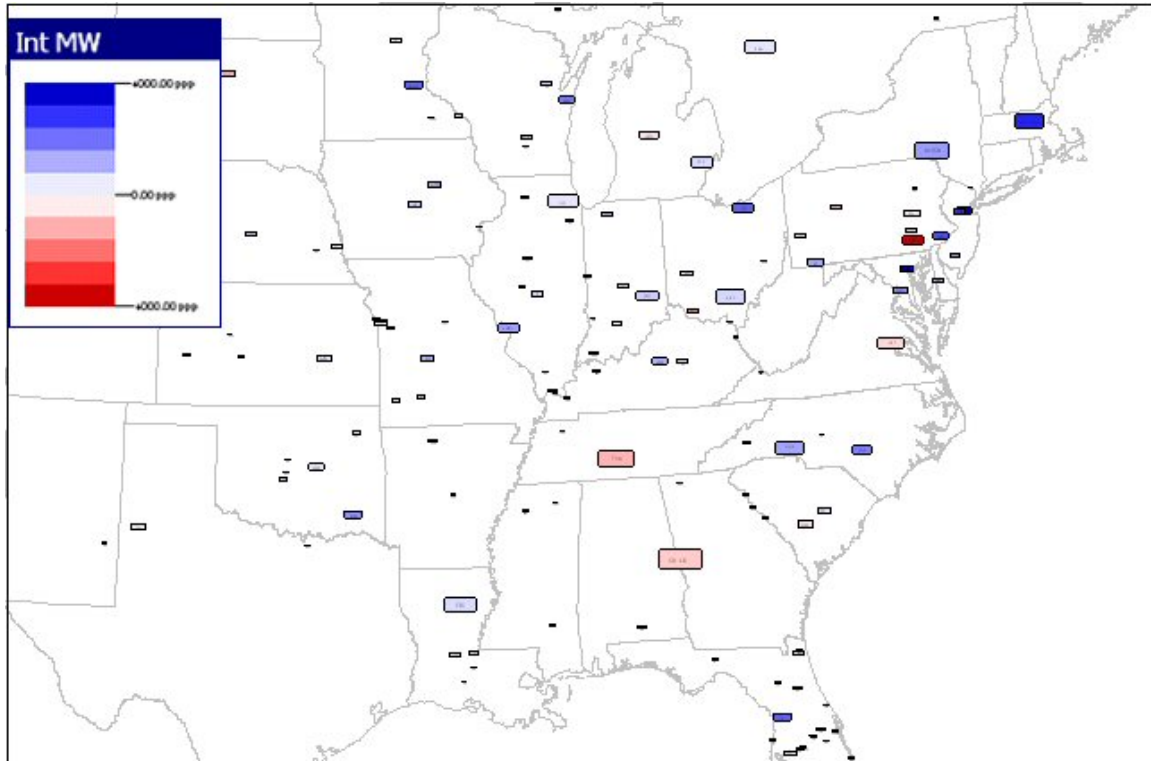


Figure 2.4: Display with Rectangle Color Based on Area Interchange

(Exports are Blue, Imports are Red)

Before moving on to the details on a GDV implementation, the issue of which geographic coordinates showed be implemented within the power system model needs to be considered. Traditional utility control center map boards and other wide-area displays have usually been constructed using pseudo-geographical coordinates at best. That is, while the displays have some relationship to the actual geographic location of the modeled devices, the need to show the one-line in a readable format tends to be the dominate design factor. A pure geographic representation, as might be done in a geographic information system (GIS), is seldom practical since locations of great interest electrically (e.g., substations) usually have a very small geographic footprint. Also, transmission lines sharing a common tower would be indistinguishable in a true GIS representation. Finally, some one-line elements, such as aggregate loads, are often spread over a large geographic area. Therefore it is expected that most GDV models would use such a pseudo-geographic approach.

However, there may be times when having a visualization that contains the exact geographic location of the power system elements could be useful. For example, one might wish to superimpose power system information with weather radar images, lightning strike data, or show the exact location of a transmission line fault. Or perhaps a substation level GDV could be used to show the exact equipment locations. Therefore it might prove useful to design GDV models so buses, lines and other elements (e.g., breakers), are modeled using two coordinates systems. One coordinate system would contain the pseudo-geographic location for the device, with the design goal being display clarity, while the second coordinate system would contain its exact latitude

and longitude. Which system to use would then just become another option when the display is created. All of the GDVs shown in this report were created using a pseudo-geographic approach.

2.3 GDV Implementation

To better illustrate the GDV approach this section describes an initial implementation of the concept. Of course, a wide variety of different implementations are possible, and the implementation shown here is certainly still a work in progress. But key design goals would be to make it easy to select the information to visualize, and to make it easy to customize the GDVs. For the GDVs shown here the approach was to have the objects and initial field to be displayed selected from tabular “case information displays.” An example of such a display is shown in Figure 2.5, in this case with the display showing all of the substations within Energy, Southern, and TVA, with the list sorted by generator real power output. Key functionality of these case information displays is their ability to allow filters to limit the objects displayed, and allow easy sorting. To create a GDV of a particular set of objects one would select the desired objects within the column corresponding to the initial field to show. As an example, the 163 substations with on-line generation were selected, with the initial field to display set to generator MW. Right-clicking on the selection, and selecting the appropriate option from a local menu results in the display of the GDV Customization Dialog, shown in Figure 2.6.

Sub Name	Sub ID	Area Name	Zone Name	# of Buses	Gen MW	Gen MW	Gen MW	Load MW	Load MW
1471001 Miller	Miller	SOCCO	APC	12	999.0	2792.00	261.83		
1471007 Barry	Barry	SOCCO	APC	26	238.0	2726.10	903.69	288.98	90.40
1471002 Cumberland (T)	Cumberland (T)	TVA	TVA_2000	6	999.0	2649.00	270.40	170.10	136.71
1471010 Browns Ferry	Browns Ferry	TVA	TVA_2000	5	999.0	2539.00	189.92	147.00	91.00
1471000 Deepwater (T)	Deepwater (T)	TVA	TVA_2000	4	999.0	2412.00	40.70	126.44	90.00
1471007 Paradise (T)	Paradise (T)	TVA	TVA_2000	7	999.0	2382.00	494.92	171.30	120.00
1471000 Johnsonville (T)	Johnsonville (T)	TVA	TVA_2000	30	999.0	2296.00	413.61	170.90	110.00
1471000 John H. Hughes (T)	John H. Hughes (T)	SOCCO	GA-070	6	999.0	2287.00	336.69		
1471000 John S. Dwyer (T)	John S. Dwyer (T)	SOCCO	APC	10	999.0	2126.00	438.32		
1471000 Rumble Road	Rumble Road	SOCCO	GA-070	12	999.0	2109.00	200.43	64.15	37.40
1471000 Willow Glen	Willow Glen	SOCCO	SOCCO	6	999.0	1989.00	479.17		
1471000 Waterford (T)	Waterford (T)	SOCCO	SOCCO	5	999.0	1972.00	103.63	76.23	10.11
1471000 Gadsden (T)	Gadsden (T)	SOCCO	APC	6	238.0	1889.04	477.92		
1471000 Gadsden	Gadsden	SOCCO	SOCCO	7	238.0	1889.00	762.46	12.40	4.90
1471007 Arkansas North	Arkansas North	SOCCO	SOCCO	6	999.0	1779.00	360.02	9.23	5.62
1471000 Edwin S. Hatch	Edwin S. Hatch	SOCCO	GA-070	6	999.0	1773.00	432.76		
1471000 Nevada Point	Nevada Point	SOCCO	SOCCO	6	238.0	1763.00	430.11	176.56	66.90
1471000 Raccoon Point	Raccoon Point	TVA	TVA_2000	6	999.0	1756.00	283.00		
1471000 Independence	Independence	SOCCO	SOCCO	6	999.0	1679.00	40.00		
1471000 Joseph M. Park	Joseph M. Park	SOCCO	APC	6	999.0	1675.00	139.26		
1471000 White Bluff	White Bluff	SOCCO	SOCCO	6	999.0	1671.00	174.34	78.10	10.44
1471000 Wilkes Creek	Wilkes Creek	TVA	TVA_2000	14	999.0	1652.00	486.27	112.00	84.00
1471000 Gadsden (T)	Gadsden (T)	TVA	TVA_2000	10	141.0	1638.00	391.03	196.91	110.47
1471000 Culbert	Culbert	TVA	TVA_2000	10	141.0	1617.00	394.30	69.00	51.74
1471000 Kingston	Kingston	TVA	TVA_2000	10	141.0	1480.00	107.04	117.76	70.30
1471000 Nelson	Nelson	SOCCO	SOCCO	6	999.0	1418.00	306.01		
1471000 Shawnee (T)	Shawnee (T)	TVA	TVA_2000	26	999.0	1400.00	457.32	940.00	500.51
1471000 Mcintosh	Mcintosh	SOCCO	SOCCO	11	238.0	1375.00	207.04	92.32	40.00
1471000 Baxter Wilson	Baxter Wilson	SOCCO	SOCCO	11	999.0	1362.40	456.12	60.39	37.00
1471000 Grand Gulf	Grand Gulf	SOCCO	SOCCO	2	999.0	1360.00	250.60	74.90	36.41
1471000 Yates	Yates	SOCCO	GA-070	9	238.0	1296.00	340.40	103.23	124.94
1471000 Geneva	Geneva	SOCCO	APC	11	238.0	1296.00	330.11	198.70	96.78

Figure 2.5: Substation Case Information Display Showing Entergy, Southern and TVA Generation Substations (intentionally blurred for data confidentiality)

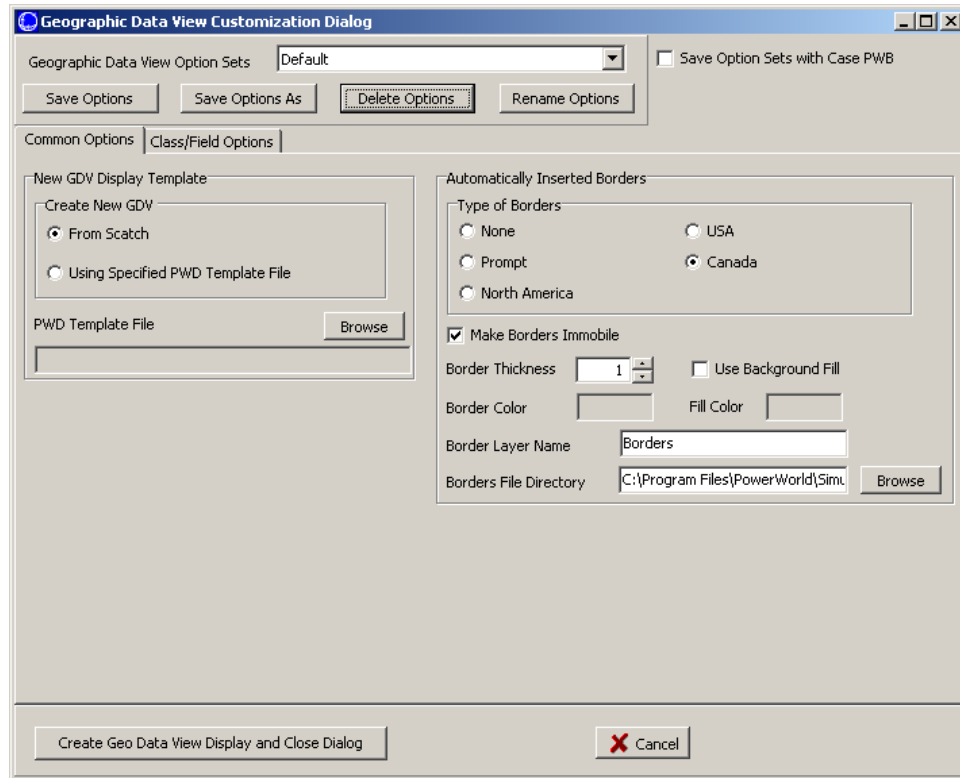


Figure 2.6: Geographic Data View Customization Dialog, Common Options Page

The GDV Customization Dialog has two main pages, corresponding to its two main tasks. The first task is to specify the background for the new GDV. Currently several options for US state borders and Canadian provincial borders are implemented, along with the more common option of using a specified template file which could include any desired predefined background.

The second page, the Class/Field Options, is used to specify how the object field data is displayed on the GDV. The page itself contains a number of subpages, with the General Display Options page shown in Figure 2.7. This page has a number of general options such as what symbol to use (rectangle, triangle, oval, etc), its default border color, border thickness, fill color, and whether identifier information should be shown on the symbol (e.g., its name and/or number). This page also provides an option to automatically determine a default size for the objects on the new GDV display. This can be quite useful since it can be quite difficult to determine a priori what size to make the objects to create a useful display. A display created using the default values, except that the border and fill colors have been changed, for the 163 substation example is shown in Figure 2.8.

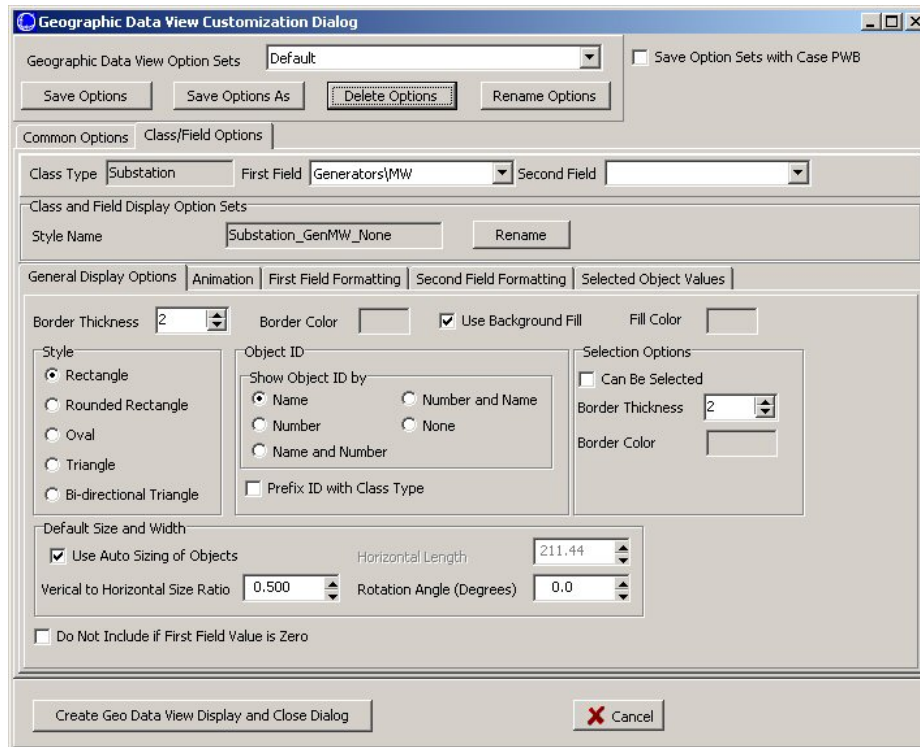


Figure 2.7: Geographic Data View Customization Dialog, Class/Field Options Page

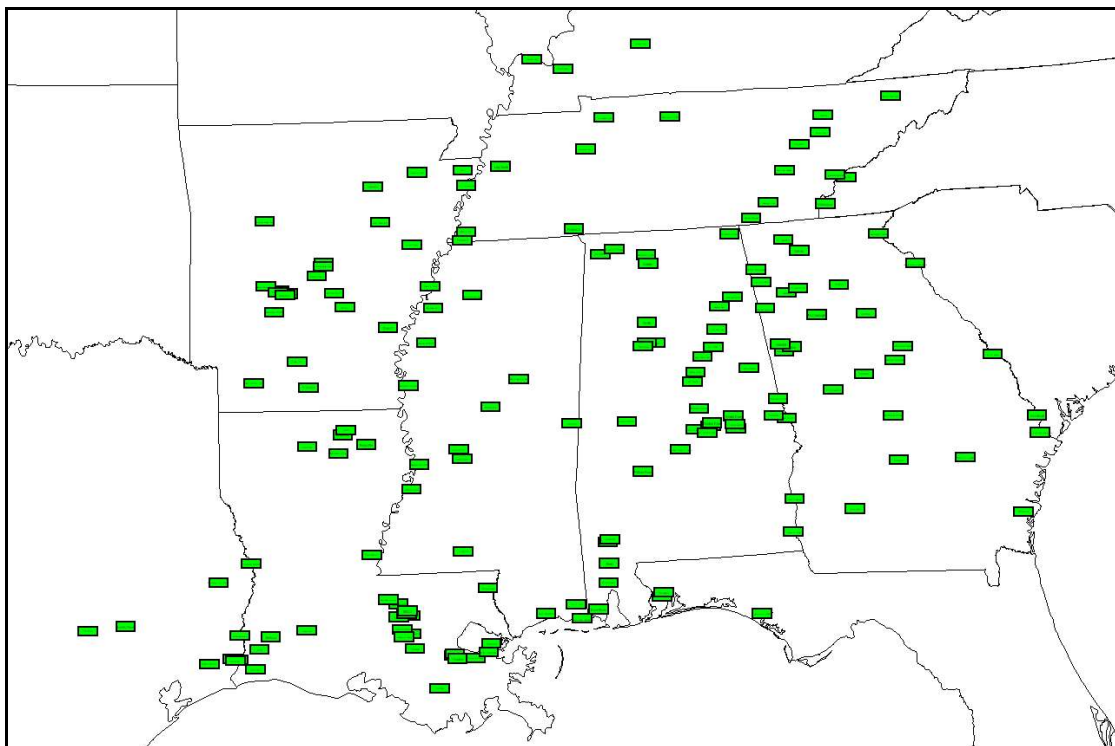


Figure 2.8: A Default Geographic Data View Showing the 163 Generation Substations

By itself the Figure 2.8 display does little more than show the geographic locations of the generation substations. While useful, especially since each display object is automatically linked to the underlying substation object allowing easy display of additional substation information, the real power of the GDV approach is in its ability to customize the visualization based upon the field values. This can be done either when the GDV is being created using subpages from the Figure 2.7 dialog, or after the GDV has been created by right-clicking on any of the display objects. For both approaches the object appearance can be dynamically updated by using the First Field Formatting and Second Field Formatting pages from Figure 2.7. Examples of these pages are shown in Figure 2.9 and Figure 2.11.

Field Value	Characteristic Value
6.000000	81
1730.999878	20080
3455.999756	40080

Figure 2.9: Geographic Data View Customization Dialog, First Field Formatting Page

The main idea for both of these formatting pages is to change the appearance of the screen object based upon the value of an object field. The field itself is selected at the top of the dialog, with the generator real power output set as the first parameter in the Figure 2.9 example. Once the field has been selected, various attributes can be customized based upon the field value. While a variety of different attributes are possible, only four are currently available: Fill Color, Total Area, Border Color, and Rate of Rotation. Once the attribute has been selected, the right side of the page is used to map the field's values to a characteristic value for the attribute. For Total Area and Rate of Rotation this is accomplished using a piece-wise linear mapping from the field value to a real number. In the Figure 2.9 example the total area (size) of the display symbol is set to be proportional to the total substation generation, with the mapping going from 81 square display units if the generation is at or below 6 MW to 40080 square display units if the generation is at or above 3456 MW. Again intelligent default values are used to simplify this

process. The results of this modification are shown in Figure 2.10. Now the locations and relative amounts of generation are available at a glance.

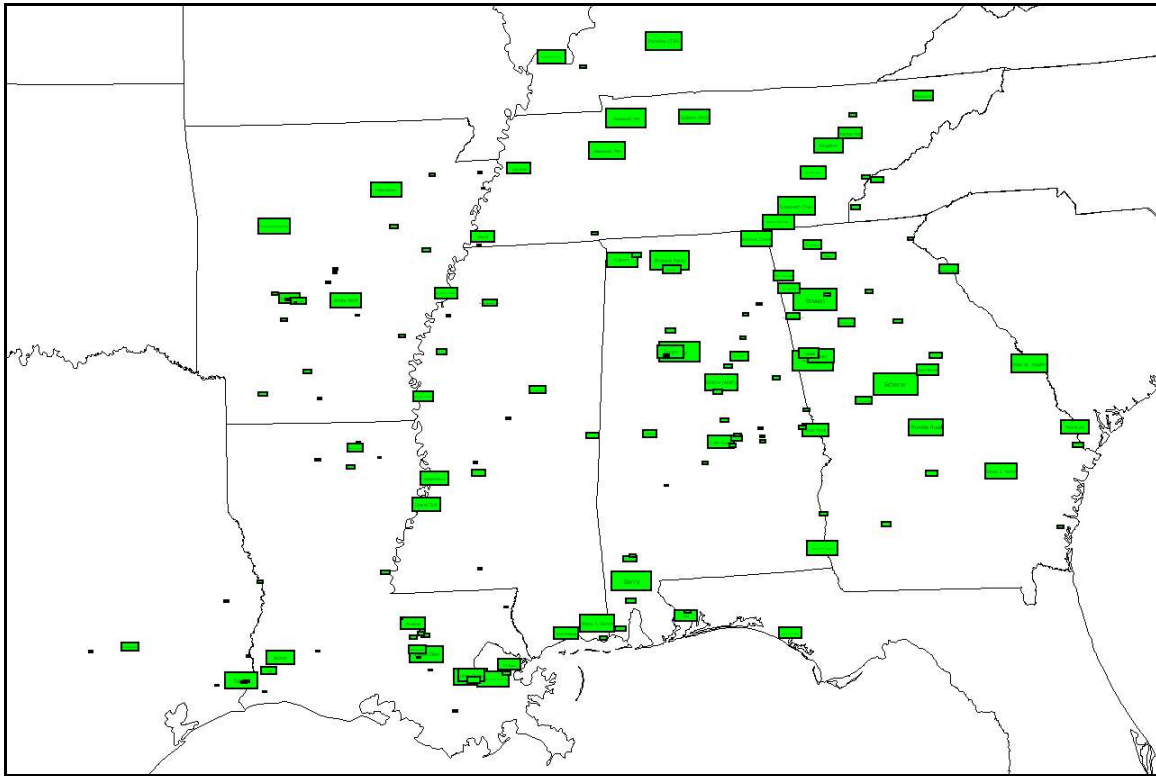


Figure 2.10: Visualization with Size Proportional to Substation Generation

Additional insight is possible by simultaneously associating other attributes with other field values. The current implementation only allows the dynamic display of two independent attributes. Certainly higher numbers of independent attributes could be possible, however one would need to avoid using too many to maintain display clarity.

Figure 2.11 shows an example in which fill color is being mapping to the ratio of the generators' reactive power output to real power output (i.e., the Q/P ratio). For the color-based attributes (fill color or border color) the right side of the page is used to select a color mapping between the field values (with a Q/P ratio range of between -0.4 and 0.4 for this example) and a color. The color mapping was chosen so generators producing reactive power are shown with a blue shade, while those absorbing reactive power are shown with a red shade. The result of the simultaneous visualization of total substation generation and generator Q/P ratio is shown in Figure 2.12. Of course many other substation fields could be visualized as well, with the current implementation allowing about one hundred. Figure 2.13 shows just one additional possibility, in which the color mapping is changed from showing the Q/P ratio to showing the generator reactive power reserves.

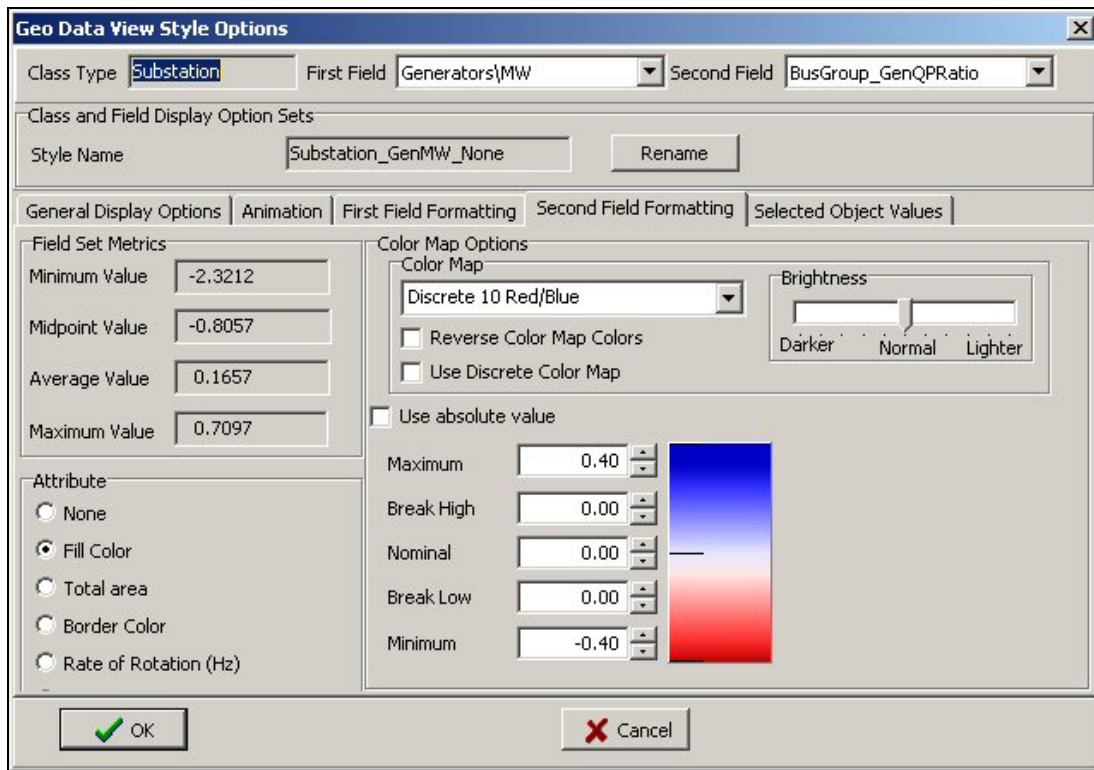


Figure 2.11: Geographic Data View Customization Dialog, Second Field Formatting Page

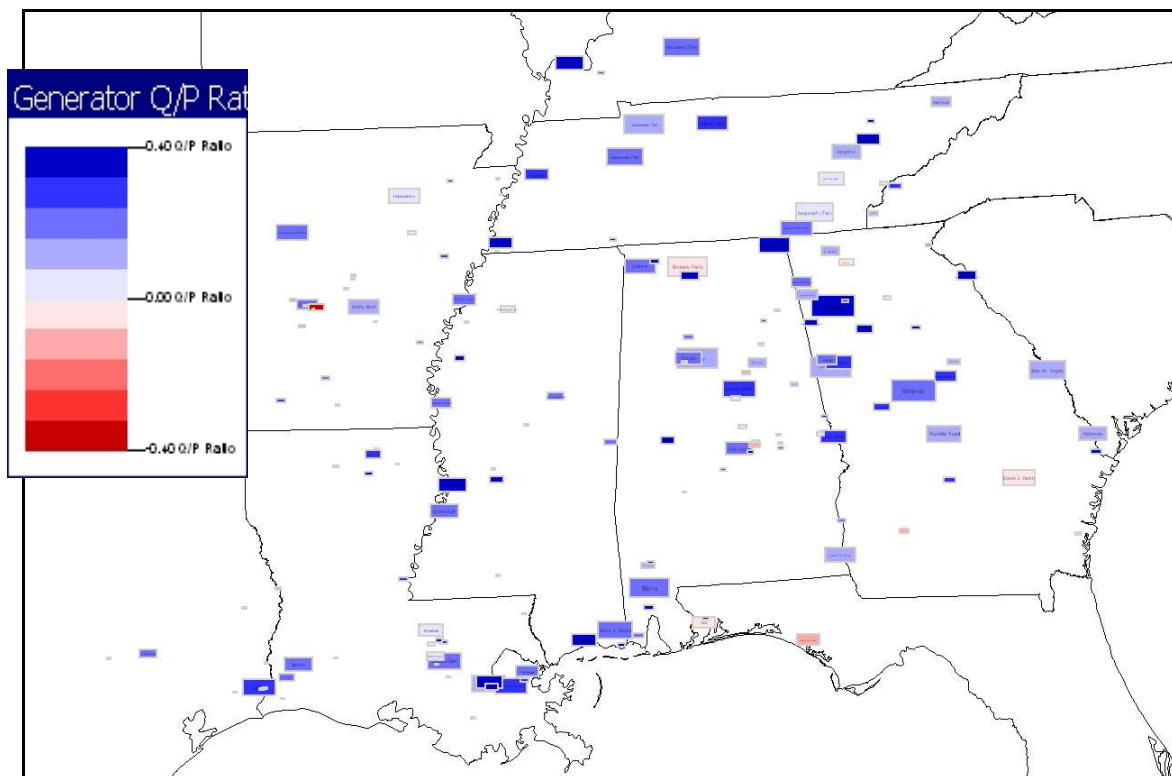


Figure 2.12: Visualization with Fill Color Proportional to Generator Q/P Ratio

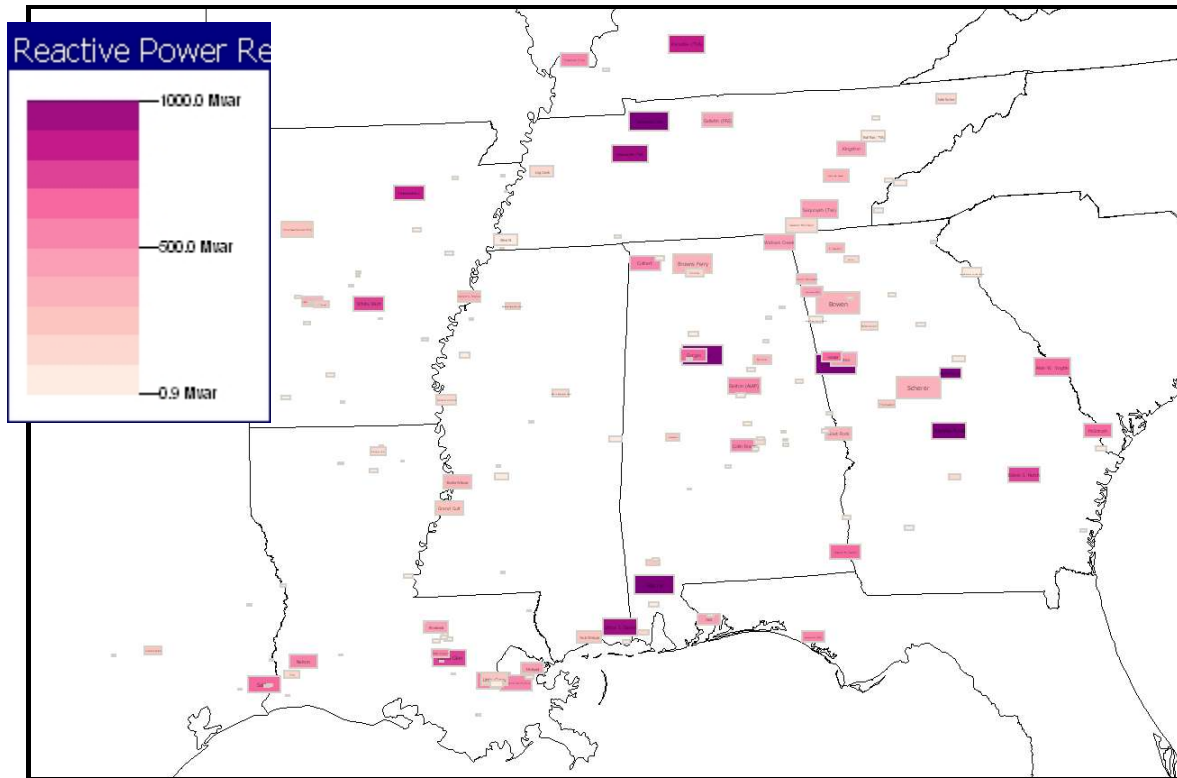


Figure 2.13: Visualization with Fill Color Proportional to Reactive Reserves

While the GDV have been designed to be quickly created and customized, it is certainly not outside the realm of reason to expect that certain GDVs would be reused. Therefore two options for quickly recreating these displays are available. First, the GDV itself can be saved just like the predefined visualizations mentioned in the beginning of the chapter. This allows the GDV to be easily used to monitor the system state albeit showing the same objects as when it was first created. Second, the customizations used to create the GDV can be saved. This allows very quick creation of new GDV but possibly with different fields. For example, the Figure 2.13 display could be recreated showing the generation for a different subset of substations.

2.4 Application of GDVs to the Line Overload Problem

This last section of the chapter provides a specific example of how GDVs can be applied to help with corrective control. As was mentioned earlier, a common operator task is the redispatch of generation to remove a line overload. This task requires a knowledge both of what generators are available to participate in the redispatch, and the impact each generation change would have on the flow of the overload line (i.e., the line flow sensitivities). The design criteria for this application was to provide the operator with options on how a particular line overload could be corrected, while minimizing the amount of numerical calculations they needed to manually perform. Hence the goal was to have the computer do much of the underlying math, assisting but not replacing, the operator in the decision-making process. This section describes how this can be accomplished using the Line Overload Correction Form (LOCF). A human factor analysis of the LOCF is presented in Chapter 6.

To begin the development of the LOCF it is helpful to first focus on the two types of information needed, the available generators, and their line flow sensitivities. Information about the generators available to participate in the redispatch, or specifically the available correction range for each generator, is independent of which line(s) is violated. From a visualization perspective this is a relatively straightforward problem since there is only one set of information that needs to be shown, and that information is usually readily available. This information could be shown either in a tabular list format or more graphically. Figure 2.14 shows an example of the latter in which the information is visualized using a GDV with objects to represent the generation available for re-dispatch, either up or down, within the TVA footprint (aggregated at the substation level). This is done using vertically symmetric quadrilaterals, denoted here as “kites,” that merge two isosceles triangles, an upward pointing one whose area is proportional to the amount by which the generation can be increased, and a downward pointing triangle whose area is proportional to the amount by which the generation can be decreased.



Figure 2.14: Visualization of Available Generation in TVA Footprint Using Kites (intentionally blurred for data confidentiality)

However, in contrast to available generation range, the line flow sensitivities depend upon which line is violated. Therefore they need to be calculated with a knowledge of the specific line whose flow should be corrected. In the current LOCF implementation this information is obtained when the LOCF is initialized by requiring the operator to right-click on either a transmission line or transformer on a one-line diagram, or on its associated pie chart. For example, for the Figure 2.15 case right-clicking on the “105%” pie chart symbol would cause the display of the LOCF.

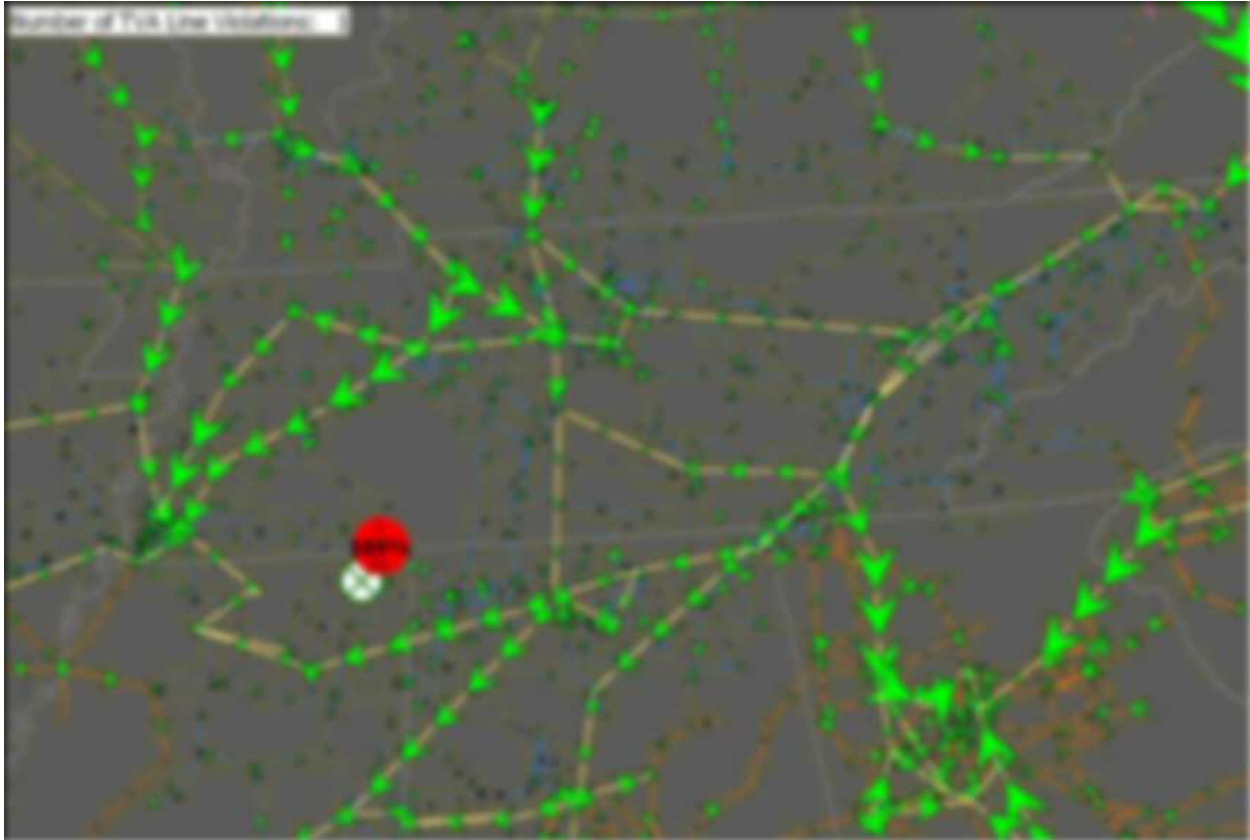


Figure 2.15: One-line Diagram Showing Overloaded Transmission Line (intentionally blurred for data confidentiality)

The LOCF was designed to allow the option to show the information needed to assist with the correction of line overloads in either a textual format or graphically using a GDV. An example of the textual format option is shown in Figure 2.16, while the GDV option is shown in Figure 2.20. The LOCF itself has three main sections. The first section, which is in the upper left, contains identifier information for the overloaded device.

The second section, which comprises the bottom 75% of the form, contains the generator sensitivity information that has been designed to help the operators make the decision about which generators to change to correct the line overload. This section of the form contains three tabbed pages that present the generator to line flow sensitivity in three different ways. The first two pages present the sensitivity information in the text-based format, with data provided for individual generators on the first page, and for generators aggregated by substation on the second page. The third page presents the generator information using a GDV aggregated by substation.

The screenshot shows the 'Line Overload Correction Form (LOCF)' with the 'Text-Based Option' selected. The form is divided into several sections:

- Top Section:** Contains input fields for 'Line ID', 'Line Name', 'Line Type', 'Line Length', 'Line Voltage', 'Line Capacity', 'Line Loss', 'Line Factor', 'Line Sensitivity', 'Line Range', 'Line Limit', 'Line Status', 'Line Type', 'Line Length', 'Line Voltage', 'Line Capacity', 'Line Loss', 'Line Factor', 'Line Sensitivity', 'Line Range', 'Line Limit', 'Line Status'.
- Second Section:** Contains a 'Select Page of Substations' dropdown and a 'Select Page of Substations' button.
- Third Section:** Contains two large tables for generator selection. The left table is titled 'Select Page of Substations' and the right table is titled 'Select Page of Substations'.

The tables contain columns for 'Substation', 'Generator', 'MW', 'MVA', 'Sensitivity', 'Range', 'Limit', 'Status', 'Type', 'Length', 'Voltage', 'Capacity', 'Loss', 'Factor', 'Sensitivity', 'Range', 'Limit', 'Status'.

Figure 2.16: Line Overload Correction Form (LOCF) Showing Text-Based Option (intentionally blurred for data confidentiality)

The individual generator page contains two lists of generators, with the left list showing the generators that would be most effective in correcting the line violation if their outputs were increased, while the generators on the right list would be most effective if their outputs were decreased. The first two columns in this list are just the name of the generator's bus and its ID. The third column gives the current status for the generator. Only generators that are either on-line or are fast start (such as combustion turbines) are listed. The fourth column lists the current output of the generator, plus any proposed changes (described later), while the fifth column lists the generator's maximum output. The sixth column then tells the sensitivity of how the line's MVA flow would decrease if the generator's MW output were increased. This sensitivity information, which is line dependent, is calculated automatically using the underlying power flow Jacobian matrix. Note, while the current implementation uses the ac power flow Jacobian, very good sensitivity information could also be calculated using a dc power flow Jacobian, which would not require the availability of an ac power flow solution. The sign convention for the sensitivities is such that positive numbers always indicate the most effective generators. The last column lists the product of the line flow sensitivity with the generator's available range. By default the list is initially sorted by this value, so the most sensitive generators that actually have available regulation range are listed first. The right list contains essentially the same column fields, except the signs on the sensitivities have been changed to represent the different movement direction, and the limit field corresponds to the generators' minimum limit.

The initial design philosophy for the LOCF was that in order to actually correct the line violation one would initially select a generator from the left list by clicking on it, and then

another from generator from the right list. That is, generation is changed in pairs with one going up and one going down. However, based upon results from the TVA operator testing this restriction should probably be removed. In the current implementation once a pair is selected, the next step is to click on the “Select MW Amount” button shown in the title area above the right list to select the MW amount by which the generator pair should be varied. Clicking on this button displays the “Line Flow Correction Dialog” shown in Figure 2.17.

The image shows a software dialog box titled "Line Flow Correction Dialog". It contains several input fields and buttons. The fields are arranged in a list-like format on the left, with their corresponding values or controls on the right. The values are intentionally blurred for confidentiality. At the bottom, there are two buttons: "OK" with a green checkmark icon and "Cancel" with a red X icon.

Field Label	Value / Control
Generation to Increase	[Blurred]
Generation to Decrease	[Blurred]
Combined Line Flow Decrease Sensitivity	[Blurred]
Line Flow Correction Needed (MW)	[Blurred]
Generation Change to Fully Correct (MW)	[Blurred]
Max. Generation Change (MW)	[Blurred]
Enter Desired Generation Change (MW)	[Blurred]

Figure 2.17: Line Flow Correction Dialog (intentionally blurred for data confidentiality)

The design goal for this dialog was to eliminate, as much as possible, the manual math that the user needs to do in order to actually select the amount by which the generation should be changed. The first two lines in the dialog list the selected generators. The third line then lists their combined line flow sensitivity. Hence it shows how the line’s MVA flow would decrease if the first generator’s output were increased and the second generator’s output were decreased by the same amount. The fourth line tells the required line flow change needed to correct the overload, while the fifth line is just the product of the third line and fourth line. Hence it tells how much the two generators should be varied if they were to single-handedly correct the violation. The sixth line tells how far the generation pair could actually change, taking into account the maximum limit on the first generator and the minimum limit on the second generator. The last line, which is the only enterable field on the dialog, is where the user specifies the desired MW change for the pair. By default this field is the minimum of the fifth and sixth fields. This change is actually scheduled by selecting the “OK” button.

Changes for other pairs of generators can be made by repeating the above process, again selecting a generator from the left list, and generator from the right list, and clicking the “Select MW Amount” button. Now, however, when the Line Flow Correction Dialog is shown the results on lines four, five and seven will take into account any previously selected changes.

Before describing the remaining pages in the second section of the form, it would be useful to finish the form's overview with a description of the last section, which is shown in the upper right. Figure 2.18 gives a zoomed view of this section. The first three fields in the section list the original maximum MVA flow on the line, the line's limit and the desired correction percentage. The desired correction percent tells the desired new MVA flow on the line as a percentage of its limit. For the human factor testing this value was set to 98%, with the rationale being we wanted to slightly overcorrect to take into account for any nonlinearities in the sensitivity calculations. The fourth field tells the required MVA change needed to achieve this correction percentage. The fifth field displays the estimated new MVA line flow taking into account any proposed generation changes shown in the "List of Selected Generation Changes".

**Figure 2.18: Proposed Line Corrections Portion of LOCF
(intentionally blurred for data confidentiality)**

The "List of Selected Generation Changes" contains the proposed generation changes made using the lower portion of the dialog. However, these changes are not actually made in the power flow until the "Make Requested Generation Changes and Solve Power Flow" button is clicked. Prior to this happening the entries in the list can be edited or deleted by left clicking on them. Clicking the button automatically changes the generation, resolves the power flow and updates the form. Figure 2.19 lists the form showing the results of the proposed changes listed in Figure 2.18.

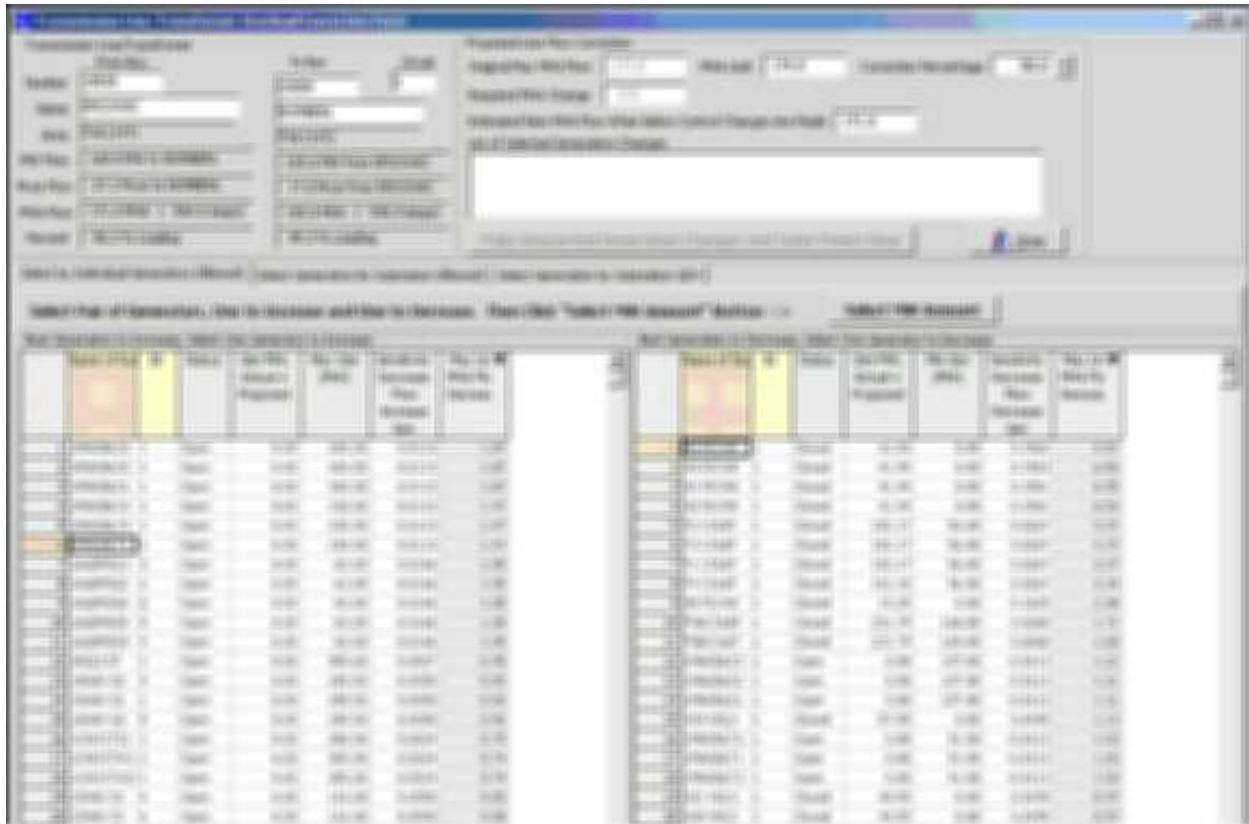


Figure 2.19: LOCF After Changes (intentionally blurred for data confidentiality)

Returning to the other tabbed pages on the lower portion of the form, the second page tab is similar to the first in that it provides a tabular list of the generators to increase and the generators to decrease. However, rather than listing individual generators, on the Select Generation by Substation page the generators are listed aggregated by substation. The process to select the generators to change is exactly the same as before, except rather than selecting individual generators the generation is selected by substation. The remainder of the procedure is the same. When the “Make Requested Generation Changes and Solve Power Flow” button is clicked the program automatically adjusts the individual generators within the selected substations, using an algorithm that the most sensitive generators are adjusted first.

The last tabbed page also displays the generators aggregated by substation, but rather than using a tabular format the information is presented graphically using a modified version of the GDV shown in Figure 2.14. The GDV version of the LOCF is shown in Figure 2.20. The GDV itself augments the one from Figure 2.14 by applying color mapping to the fill of each kite so its color is proportional to the sensitivity of the line’s MVA flow with respect to decreasing the substation’s generation. The color mapping is such that red represents locations where the generation should be increased and blue where it should be decreased. Therefore to correct the line overload the user would be looking for red upward pointing kites and blue downward pointing triangles.



Figure 2.20: Line Overload Correction Form (LOCF) Showing GDV Option (intentionally blurred)

Similar to the other two pages, one selects the generation at one substation to increase, and one to decrease. This is done by simply left-clicking on the symbols, which causes a thick green border to be drawn on the symbol. Then the user clicks on the “Select MW Amount” button to display the Line Correction Dialog, with the remainder of the procedure the same as what was described earlier. The second display condition for the human factor testing results from Chapter 6 used this display.

To summarize, this chapter has introduced the concept of GDVs, in which new visualizations are created on-the-fly based upon power system information coupled with embedded geographic information. A key advantage of GDVs is they can be used to visualize a wide variety of different power system field values with the ability to use different display attributes to simultaneously show different fields. However, it should be emphasized that GDVs are not intended to replace existing text-based and predefined object visualizations. Rather they are

intended to supplement existing techniques, with the major uses expected in the areas of power system analysis and corrective control particularly for wide-area visualizations.

3.0 Improved Power System Contouring¹

A second aspect of this project considered how to speed up existing visualization techniques. Certainly an important visualization requirement is the need for responsive displays, a requirement that was mentioned in a number of the initial control center visits for this project. Currently one of the most numerically intensive aspects of modern power system control center visualizations is the display of contours, usually for bus-based values. This chapter presents two techniques for improving the computational efficiency of existing contouring routines. The chapter first presents the basics of contouring along with the method of using an influence region to determine how much of the contour each bus will affect. Then, a new contouring algorithm, called the Adaptive Influence Region Algorithm, is introduced, whose objective is to produce quality contouring images at faster speeds compared to previous algorithms. After presenting a theoretical analysis of contour timing, empirical results for the Adaptive Algorithm are discussed. Next, the use of the new algorithm is validated through an examination of the created visualizations. Finally, a potentially much faster numerical algorithm that takes advantage of the graphics card processor is introduced.

3.1 Contouring Basics

Before discussing contour plots in detail, it is useful to consider what constitutes a good graphical representation. Since the quality of the images is important, some simple guidelines must be established to define effective visualizations. The three keys set out by [3] are:

- Natural encoding of information
- Task specific graphics
- No gratuitous graphics

A natural encoding of the information implies that the display's meaning is intuitively obvious to the user, and that no training is necessary to explain the objective of such displays. For a task-specific representation, the task is the underlying control of what is being displayed. Features not pertinent to the task are disregarded. Recall that the goal of these visualizations is to transmit information, not to create an aesthetically pleasing picture. Gratuitous graphics, which do not hold operationally useful information, must also be suppressed so as not to confuse the user. In [4], the argument is made that contour plots do in fact meet these criteria. Contour plots are fairly common tools that most people can associate with. The prevalence of weather maps on evening news shows provide widespread exposure of such representations and give many people an inherent understanding of the data. The guidelines for providing task-specific and essential graphics can be satisfied by creating customized one-line diagrams that enable a clear interpretation of the data.

Now that contouring has been justified as a viable visualization option, it is important to consider implementation strategies. A significant amount of power system data, including voltage magnitude and angle, load, and generation, is referenced to the system buses. Unfortunately, since buses exist at discrete points in the system, employing contouring requires that these points be mapped onto a continuous surface. For computer implementation, this continuous surface can be represented as a grid of data points, where each point corresponds to a

¹ Much of the material presented in the beginning of this section is reproduced from project publication A, "Adaptive Influence Distance Algorithm for Contouring Bus-Based Power System Data", presented at the 40th Hawaii International Conference on System Sciences (HICSS), Kona, HI, January 2007

pixel on the monitor. The color of each pixel is determined by mapping the value of the data point according to some color scheme. For pixels representing actual buses, the data value is known. However, for other pixels (those representing points in between the buses) a virtual value must be calculated. There are many possible algorithms for creating these virtual values, some of which are addressed in the next section.

3.1.1 Shepard's Method

Shepard's method is a brute force approach where each virtual value is calculated as a weighted-sum of the values of all the system buses [5]. The weighting is based upon the distance separating the bus and the virtual point. Buses that are closer to the virtual point should have higher weightings than those further away. With reference to Figure 3.1, since $d_1 > d_3 > d_2$ for the calculation of the virtual value at point (x_0, y_0) , the value at (x_2, y_2) is weighted more than (x_3, y_3) which is weighted more than (x_1, y_1) .

This algorithm assumes that buses near one another geographically are also near one another electrically. This assumption is validated through judicious construction of the one-line diagram. Care should be taken to ensure that the one-line correctly represents the geography of the real system. The virtual values are calculated using (3.1).

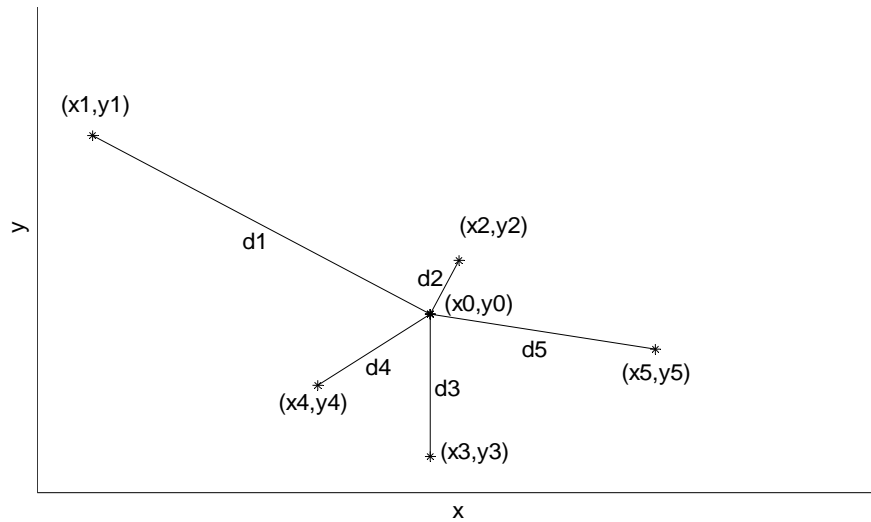


Figure 3.1: Virtual Value Calculation

$$v_p = \begin{cases} \frac{\sum_{i = \text{all buses}} \left(v_i \frac{1}{d_{pi}^\alpha} \right)}{\sum_{k = \text{all buses}} \left(\frac{1}{d_{pk}^\alpha} \right)} & \text{if } d_{pi} \neq 0 \\ v_i & \text{if } d_{pi} = 0 \end{cases} \quad (3.1)$$

where

v_p = value for virtual position p

v_i = value for bus i

d_{pi} = distance from position p to the center of bus i

α = parameter controlling weight

The α parameter can be changed to control the relative weightings of close versus far buses. A higher α value results in more weight given to the nearest buses. For general purposes, using $\alpha = 2$ is preferred because it gives satisfactory surface mapping results and it provides for the fastest computation time.

3.1.2 Mapping Virtual Values Into A Color Scheme

Once the virtual values for all the pixels on the screen are created, they must be mapped into a color scheme. Most computers use a three primary color additive model, where shades of the three primary colors (red, green, and blue) add together to produce the perceived color. Assuming a typical system, where each pixel consists of 24 bits, each pixel can be colored one of 2^{24} (16.7 M) distinct colors. This means the primary colors can take on one of 2^8 values (0 – 255), which decide its shade. Zero denotes none of the primary color, and 255 denotes a maximum or saturated value. An example of a common mapping method is shown in Figure 3.2 where high values are mapped to red and low values are mapped to blue.

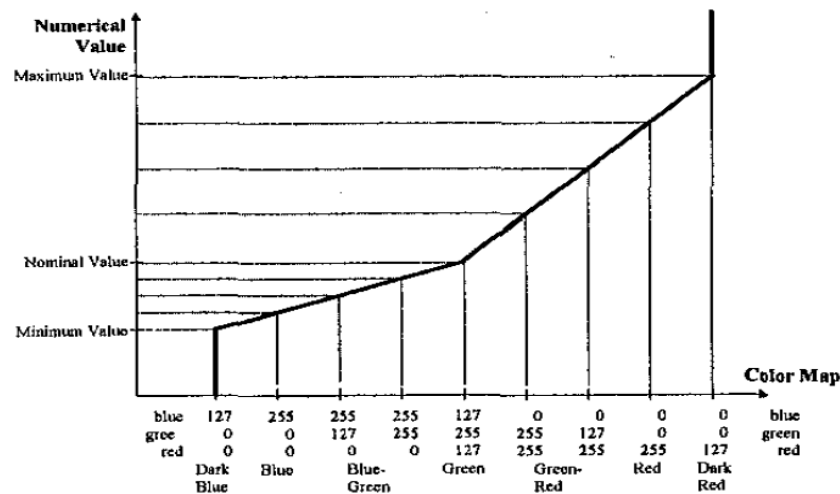


Figure 3.2: Color Mapping for Red = High, Blue = Low

Another available option is the use of continuous versus discrete color mappings. For a continuous mapping an upper, lower and nominal value is defined while the rest of the scale is defined by an interpolative blending of these values. For continuous color scales, no definite sections exist, making it difficult, with a large degree of accuracy, to determine a pixel's value. When using a discrete mapping, however, the color scale is divided into discrete sections. The value of any pixel is guaranteed to be within the scale limits specified by its corresponding color. Figure 3.3 shows a 10-color discrete scale. The main advantage of discrete scales is that the user can always determine, within some definite range, the value of any pixel. This is the color scale utilized for the experimental analysis in Section 3.4.

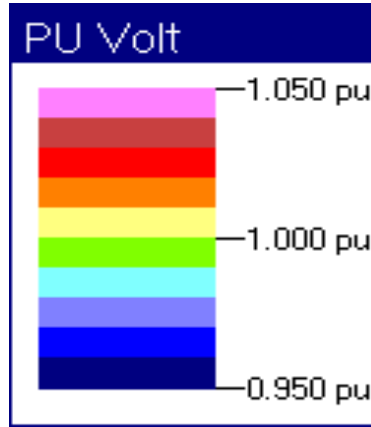


Figure 3.3: Ten-Color Discrete Scale

3.2 Influence Distance

The weighted-sum calculation method for the virtual values is the basis for all of the algorithms explored in this paper. Unfortunately, the original Shepard's method has several shortcomings, the most prominent being its computational inefficiency. Every bus is considered in the summation calculations of every virtual value, which is not only slow but also nonsensical, since buses that are separated by hundreds of miles normally have negligible effects on one another. Since only “near” buses significantly influence virtual values, one solution for improving efficiency is to eliminate calculations from distant buses. One approach, the fast contouring algorithm, introduced by [4], suggests the use of an arbitrary distance criterion, where only virtual points located within some specified distance from a bus contribute to the weighted-sum.

Within this algorithm, each virtual point is no longer influenced by every bus in the system, but instead by only a collection of geographically close buses. An influence region, as seen in Figure 3.4, is established for each bus in the system as a conceptual circle radiating out from the midpoint of the bus. This work defines the radius of said circle to be β . Only virtual points within this circle are affected by the bus. As β grows the total number of pixels being colored grows, and the influence regions begin to coincide and merge. As β approaches infinity, the results approach those found using the original Shepard's method.

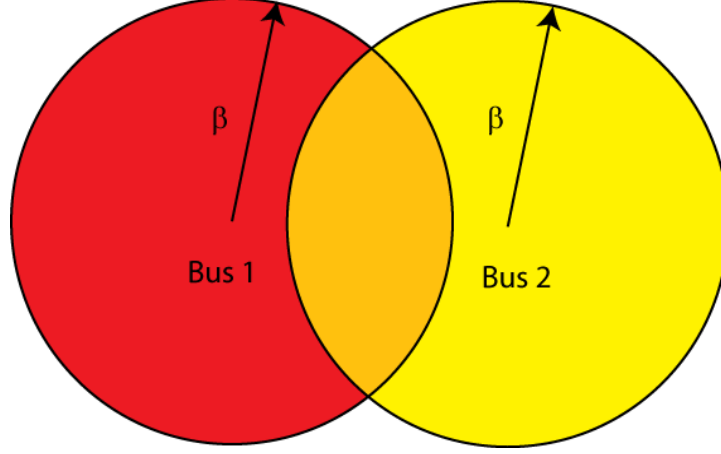


Figure 3.4: Bus Influence Distance

The virtual value calculations are similar to the basic Shepard algorithm, with the exception that the summations are now over only “influencing buses” instead of “all buses.” The new virtual value calculation equation is defined in (2):

$$v_p = \frac{\sum_{i = \text{all "influencing" buses}} \left(v_i \frac{1}{d_{pk}^\alpha} \right)}{\sum_{k = \text{all "influencing" buses}} \left(\frac{1}{d_{pk}^\alpha} \right)} \quad (3.2)$$

A two-dimensional array, with entries for each point of the contour region, is used to store the two summations in (2). Each bus in the system is processed in turn. For those points within its influence region, the corresponding entry in the array is updated by adding an additional term to both summations. After all the buses are processed, the two summations are divided to calculate the virtual value. The virtual value calculation for bus i located at (x_i, y_i) looks like a double integral over a circular region as follows.

```

For  $x = (-\beta + x_i)$  to  $(\beta + x_i)$ 
  For  $y = (-(\beta^2 - x_i^2)^{0.5} + y_i)$  to  $((\beta^2 - x_i^2)^{0.5} + y_i)$ 
     $d = ((x - x_i)^2 + (y - y_i)^2)^{0.5}$ 
    Update numerator sum at  $(x, y)$  with  $(v_i/d)$ 
    Update denominator sum at  $(x, y)$  with  $(1/d)$ 
  Next  $y$ 
Next  $x$ 

```

For the weighted-sum-based algorithms, the virtual value calculation times are proportional to the number of computations, which is basically the number of times the summations are updated. For Shepard’s method, where every bus affects every pixel, the number of updates is equal to the product of the number of system buses and the number of pixels on the screen. Consider an

example with an $N \times M$ screen resolution and K system buses. The total number of computations would be $N \times M \times K$. However, the number of computations needed for the fast contouring algorithm is much lower, since only a subset of the total system buses are used, and each bus does not necessarily affect every pixel on the screen.

The most significant shortcoming of the fast contouring algorithm is that contouring dense areas is substantially slower than contouring sparse areas. Dense areas have a larger subset of buses to consider than sparse areas. The reduction in speed is especially apparent for zoomed in views of dense areas. Since the influence distance is independent of the zoom level and the number of pixels on the screen, upon zooming in a bus's influence region will encompass more pixels. As the zoom level increases, the number of affected pixels approaches the number of pixels on the screen. When this occurs, the difference in speed between Shepard's method and the fast contouring algorithm is entirely based on the number of buses that affect the contour. The bus count for dense areas, while not as high as in Shepard's method, is much higher than for sparse areas. This accounts for the disparity in speeds. The algorithm presented in the next section is an attempt to speed up contouring times by allowing each bus to possess a unique influence distance that may be reduced from the original.

3.3 Adaptive Influence Region Algorithm

The fast contouring algorithm is an improvement in terms of computational efficiency over the basic Shepard's method. However, for the purposes of continuously updating contours based on real-time data, the need for an even faster contouring algorithm exists. In the fast contouring algorithm, all of the buses have the same size influence region. This causes problems in areas with a high bus density. Particularly if the influence distance is large, virtual points are influenced by too many buses, making the contour slow and less physically meaningful. To counter these issues, an algorithm must be developed where each bus can have a unique influence distance. Each bus's influence distance is calculated as the minimum of the original influence distance and the distance to the g^{th} closest bus, where g is a parameter set by the user. The higher g is set, the larger the influence distance.

The individual influence distance calculations introduce computations not present in the fast contouring algorithm. However, a reduction in a bus's influence distance results in fewer affected pixels, and thus a decrease in the computation count. The aspiration of the Adaptive Algorithm is that even with added computation time caused by the calculation of the reduced influence distances, the decrease in each bus's pixel coverage will ultimately result in a faster algorithm. This algorithm can be stated as follows.

Given:

- $N \times M$ screen resolution
- Rectangular contour region defined by the coordinates of $[(MinX, MinY) (MinX, MaxY) (MaxX, MaxY) (MaxX, MinY)]$
- Original influence region radius of β_0
- $i = 1, \dots, K$ system buses, where bus i is located at coordinate (x_i, y_i)
- g = the number of buses used to resize a bus's influence distance

Step 1: Create an $N \times M$ array (*ContArray*) to hold the two summations used to calculate the virtual values for each pixel in the contour region.

Step 2: Create a list of buses (*ContourBuses*) to be considered during the contouring. These buses are the subset of the K system buses located within the contour region or a distance less than β_0 outside the region.

Step 3: Cycle through *ContourBuses*, searching for and storing the minimum and maximum X and Y coordinates ($BusMaxX$, $BusMinX$, $BusMaxY$, $BusMinY$). These coordinates define the smallest rectangular region which encompasses all of the buses in *ContourBuses*.

Step 4: Set up a grid to facilitate the adaptive sizing of each bus's influence region. This step breaks up the rectangular region found in step 3 into a grid with the distance between the grid points at least equal to the original influence region radius, β_0 . Each cell in the grid holds a list of the buses associated with that particular section of the region.

i) Find the size of the grid in terms of blocks.

$$GridSizeX = truncation\left(\frac{BusMaxX - BusMinX}{\beta_0}\right) + 1 \quad (3.3)$$

$$GridSizeY = truncation\left(\frac{BusMaxY - BusMinY}{\beta_0}\right) + 1 \quad (3.4)$$

ii) Create and initialize a $GridSizeX \times GridSizeY$ array (*BusGrid*) to hold the bus lists.

iii) Cycle through each bus in *ContourBuses*, placing them onto the list in the appropriate cell defined by [NewX, NewY] of *BusGrid*.

$$NewX = truncation\left(\frac{x_i - BusMinX}{\beta_0}\right) + 1 \quad (3.5)$$

$$NewY = truncation\left(\frac{y_i - BusMinY}{\beta_0}\right) + 1 \quad (3.6)$$

Step 5: For each bus in *ContourBuses*, calculate a new influence distance that is possibly smaller than the original influence distance. The new influence radius, β_i , will be the minimum of the original influence distance and the distance to the g^{th} closest bus.

For bus i :

i) Retrieve the cell location in *BusGrid* for bus i .

ii) Get a count of all the buses contained within not only this cell but all of the eight (less if the cell is on the region border) adjacent cells as well. This number is defined as *NearbyCount*. Before proceeding, one must decrement *NearbyCount* by 1, so as not to count bus i itself.

iii) If $NearbyCount \leq g$, then stop and $\beta_i = \beta_0$. Else go to step iv).

iv) Cycle through the bus lists for all nine (or less) cells and store in another list ($Distance$) the distance between bus i and each of the other buses.

v) Sort $Distance$ in ascending order. The new influence distance for bus i is the $(g+1)^{th}$ entry in the list ($g+1$ is used because the first entry will always be 0, the distance between bus i and itself).

$$\beta_i = Distance[g + 1] \quad (3.7)$$

Step 6: Process each bus in *ContourBuses* in turn, updating the summations in *ContArray*. Then calculate each virtual value by dividing the numerator summation by the denominator summation, as in (3.2).

Step 7: Map the virtual value into a color scheme

3.4 Adaptive Algorithm Testing

Testing the effectiveness of the Adaptive Influence Region Algorithm requires two steps. First, timing data must be recorded under various conditions to compare the Adaptive Algorithm's speed to the speed of the fast contouring algorithm. Second, an examination of the visualizations that the Adaptive Algorithm produces is conducted to ensure that no information has been lost in a tradeoff for faster computation time.

3.4.1 Experimental Setup

Contours were created per unit voltage data on a one-line diagram showing the transmission grid of Illinois. In order to show that the Adaptive Algorithm is effective under various conditions, combinations of several variables are changed to obtain the timing data:

- The original influence distance, β_0 . Five different values of β_0 are used: 1%, 25%, 50%, 75%, and 100% of the allowable range in PowerWorld Simulator.
- The number of “near” buses used to calculate the adaptive influence distance for each bus, g . Tests are run without adaptive sizing ($g = \infty$) and for g equal to 5, 10, 30, and 60.
- The magnification level of the one-line diagram. Times are taken at five zoom levels: 1.5%, 10%, 30%, 60%, and 100%. Zooming is centered on the Chicago area due to the region's high density of buses. Zoomed-in views of dense areas usually create the slowest contouring times and thus are where the Adaptive Algorithm is most needed.

3.4.2 Contouring Time – Theoretical Results

Two main components affect contouring times: the time it takes to evaluate each virtual value and the time it takes to map these values into a color scheme and display the image on screen. The goal of the Adaptive Algorithm is to increase the speed of the virtual value evaluations. The main timing issue is the number of computations needed to create these values. The number of computations is proportional to the summation, over the set of buses affecting the contour, of the number of on-screen pixels affected by each bus.

$$VC \propto \text{the number of computations} \propto \sum_{i \in \Omega} p_i \quad (3.8)$$

$$p_i \propto \beta_i \quad (3.9)$$

In (3.8) and (3.9),

- p_i = the number of on-screen pixels contained in the influence region of bus i
- Ω = the subset of the K system buses considered in the contour
- VC = virtual values calculation time
- β_i = the influence distance for bus i

Three cases are considered, in which two of the variables are held constant and the last is varied. The three experimental timing variables are defined in Section A. Theoretical results are presented below and then compared to the experimental results in Section C.

Case 1: g is allowed to vary while β_0 and the zoom level are held constant

Since β_0 and the zoom level are held constant, the number of buses in Ω are constant, making the number of pixels covered dependent on the influence distance for each bus. As g increases, a bus is less likely to reduce its influence distance from the original. When these reductions take place, the margin of reduction is generally smaller for larger g values. Since the fast algorithm is equivalent to setting g to infinity, the use of the Adaptive Algorithm should generally result in faster contouring times.

Case 2: β_0 is allowed to vary while g and the zoom level are held constant

Since g and the zoom level are held constant, an increase in β_0 causes an increase in the number of pixels influenced by each bus, thereby increasing computations and contouring times. When using the Adaptive Algorithm, an increase in β_0 will never result in the decrease of β_i for any bus. The term β_i will either stay at the distance calculated based on the g variable, or, as in sparse areas, will equal β_0 . Also, since the number of buses in Ω is defined as both those buses within the contour region and those buses a distance less than β_0 outside the contour region, an increase in β_0 can potentially lead to an increase in the number of buses contained in Ω . This also causes an increase in computations.

Case 3: The zoom level is allowed to vary while g and β_0 are held constant

It is difficult to predict the results for this case. Zooming in on the one-line diagram causes the number of buses contained in Ω to decrease because the area being contoured is shrinking. This suggests a decrease in contouring times when zooming in. However, zooming in also causes the number of pixels encompassed by a bus's influence region to increase because the influence distance is based on true distance, not on the number of pixels. In essence, zooming makes the influence area seem to grow larger and cover more pixels. For example, if the influence region covers from $x = 3$ to 6, after zooming in, the influence region still covers $x = 3$ to 6. However, since the screen resolution does not change, there are now more pixels located between $x = 3$ to $x = 6$ than originally. The increased number of pixels would indicate an increase in contouring times.

3.4.3. Contouring Times – Experimental Results

Contouring times are recorded for every possible combination of the three variables, resulting in a total of 125 measurements. For the sake of space and ease, only a subset of these measurements is shown in this section. Examination of the measurements reveals several data trends. Note that for the tables in this section, $g = \infty$ refers to using the Fast Contouring Algorithm.

Case 1: g is allowed to vary while β_0 and the zoom level are held constant

Table 3. shows the measurements for all combinations of zoom level and g , with β_0 held constant at 50% of the allowable range.

Table 3.1: Timing Data for $\beta_0 = 50\%$ of Allowable Range

Zoom Level = 1.5%		Zoom Level = 10%		Zoom Level = 30%		Zoom Level = 60%		Zoom Level = 100%	
g	Time (s)	g	Time (s)	g	Time (s)	g	Time (s)	g	Time (s)
∞	0.88	∞	2.69	∞	4.13	∞	3.72	∞	1.43
60	1.47	60	1.17	60	1.12	60	1.05	60	0.89
30	1.41	30	1.14	30	0.99	30	0.82	30	0.73
10	1.36	10	1.09	10	0.94	10	0.76	10	0.67
5	1.36	5	1.04	5	0.90	5	0.72	5	0.63

Several data trends can be discerned from the data in Table 3.. When utilizing the Adaptive Algorithm, the larger g is, the slower the contouring time. This is reasonable because the larger the g value is, the less likely a bus is to reduce its influence distance from the original. These results are consistent with theoretical expectations.

Another theoretical expectation contends that the Adaptive Algorithm is faster than the fast contouring algorithm. This was true for zoom levels of 10% and higher. However, for the 1.5% zoom level, the Adaptive Algorithm is actually slower. At the 1.5% zoom level, most of Illinois and its surrounding connections in the Midwest are visible. Most of these areas are sparse, and running the Adaptive Algorithm does not reduce many of the buses' influence distances. If a large number of buses on the screen do not reduce their influence, then the overhead of running the more complicated algorithm results in slower contouring times. As one zooms in, particularly on the dense Chicago area, more and more buses reduce their influence causing a reduction in the number of pixels covered and a reduction in computations that outweighs the increased overhead. It is important to note that while in most cases the Adaptive Algorithm is faster, this is not always the case. These same trends exist for all choices of β_0 .

Case 2: β_0 is allowed to vary while g and the zoom level are held constant

Table 3. shows the measurements for all combinations of β_0 and g , with the zoom level held constant at 10%. The data in Table 3. indicates that contouring times increase with β_0 , regardless of the use of adaptive sizing or the choice of g when adaptive sizing is in effect. These results agree with the theoretical expectations presented earlier. The larger the influence distance for a bus, the more pixels it will cover, creating more computations and raising contouring times. The same trend is observed for all zoom levels.

Case 3: The zoom level is allowed to vary while g and β_0 are held constant

Table 3. shows the measurements for all combinations of zoom level and g , with β_0 held constant at 75% of the allowable range. For the fast contouring algorithm, the trade-off suggested in the theoretical expectations is observed. As one zooms in, the number of pixels covered by the influence regions of the buses increases and the contouring times begin to slow down. However, after zooming in past 30%, the number of buses contained in Ω decreases enough so that the contouring times begin to speed up. To better illustrate this effect, timing data is taken at more zoom levels for the $g = \infty$, $\beta_0 = 75\%$ case. A plot of the contouring time versus zoom level is shown in Figure 3.5. It shows that the contouring time peaks between 25% and 35%.

Table 3.2: Timing Data at Zoom Level = 10%

$g = \infty$		$g = 60$		$g = 30$		$g = 10$		$g = 5$	
β_0 (%)	Time (s)	β_0 (%)	Time (s)	β_0 (%)	Time (s)	β_0 (%)	Time (s)	β_0 (%)	Time (s)
1	0.93	1	0.93	1	0.91	1	0.84	1	0.79
25	1.72	25	1.12	25	1.09	25	1.07	25	1.01
50	2.69	50	1.17	50	1.14	50	1.09	50	1.03
75	3.29	75	1.25	75	1.15	75	1.10	75	1.04
100	8.57	100	1.26	100	1.21	100	1.18	100	1.15

Table 3.3: Timing Data for $\beta_0 = 75\%$ of Allowable Range

$g = \infty$		$g = 60$		$g = 30$		$g = 10$		$g = 5$	
Zoom Level (%)	Time (s)	Zoom Level (%)	Time (s)	Zoom Level (%)	Time (s)	Zoom Level (%)	Time (s)	Zoom Level (%)	Time (s)
1.5	1.10	1.5	1.76	1.5	1.68	1.5	1.62	1.5	1.57
10	3.29	10	1.25	10	1.15	10	1.09	10	1.04
30	4.90	30	1.15	30	1.00	30	0.99	30	0.95
60	4.51	60	1.06	60	0.83	60	0.78	60	0.72
100	1.59	100	0.90	100	0.74	100	0.67	100	0.63

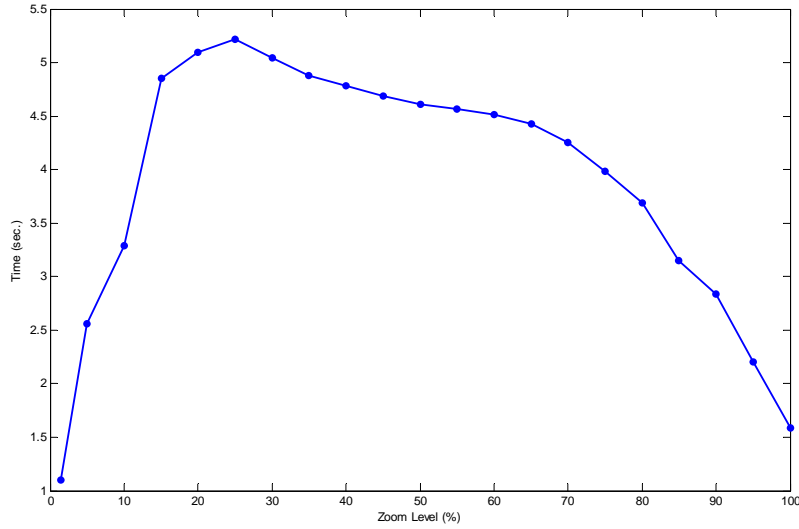


Figure 3.5: Zoom Level vs. Time for $g = \infty$, $\beta_0 = 75\%$

This peaking behavior does not appear to occur when using the Adaptive Algorithm. This means that the Adaptive Algorithm is reducing the influence distances enough that the speed increase caused by the decrease in the number of buses in Ω is more dominant than the speed decrease caused by the increased pixel coverage. This illustrates one of the key advantages of the Adaptive Algorithm since the slowest contour times usually result from zooming in on dense areas. These same trends exist for all choices of β_0 .

Results indicate that in general the Adaptive Algorithm is much faster than the fast contouring algorithm, but how much faster? This is difficult to quantify. Consider the zoom level of 30%. It is possible to compare the average time it takes for each choice of g , where the average is that of the data taken over all five choices of β_0 . Table 3. tabulates this data.

Table 3.4: Average Time Comparison for Zoom Level = 30%

g	Average Time (s)	# Times Faster Than $g = \infty$
$g = \infty$	5.52	---
$g = 60$	1.11	4.97
$g = 30$	1.00	5.52
$g = 10$	0.95	5.81
$g = 5$	0.90	6.13

The data shows that, on average, the Adaptive Algorithm is over five times faster than the fast contouring algorithm. Often times this average can mask the time variation that occurs as β_0 changes. Table 3. shows the worst-case times over the five choices of β_0 .

Table 3.5: Worst Case Time Comparison for Zoom Level = 30%

g	Worst-Case Time (s)	# Times Faster Than $g = \infty$
$g = \infty$	14.73	---
$g = 60$	1.16	12.70
$g = 30$	1.10	13.39
$g = 10$	1.03	14.30
$g = 5$	0.99	14.88

Table 3. shows that for the worst-case scenario, the Adaptive Algorithm is, on average, 14 times faster. Another thing to note is that all of the times taken are total contouring times, constituting both virtual value calculation time and color mapping time. If one assumes that the mapping time is roughly constant, then the speed of calculating the virtual values alone is several times faster than what previously calculated.

3.4.4 Contouring Images

This research shows that the Adaptive Algorithm generally has an increase in speed. However, another important part of contouring is creating a quality image. If the picture produced has little physical meaning or is hard to understand, then the fact that the algorithm that produces it is faster is inconsequential. In this section the images are compared to those made using the fast contouring algorithm and, the merits of the Adaptive Algorithm images are discussed.

Figure 3.6-10 are contours taken for different choices of g , while the zoom level and β_0 are held constant at 60% and 25%, respectively. At first glance, the contour created using the fast contouring algorithm (Figure 3.6) may cause one to believe that almost all the buses in the contour region have a voltage between 1.00 p.u. and 1.01 p.u., since almost the entire diagram is the same color. Upon close inspection, small colored circles (representing 0.99 p.u. to 1.00 p.u.) can be discerned around some of the buses, especially those in the upper middle portion of the image. Also, small colored circles (representing voltage magnitudes between 1.01 p.u. to 1.02 p.u.) are also observed around the buses in the upper left and bottom right portions on the region.

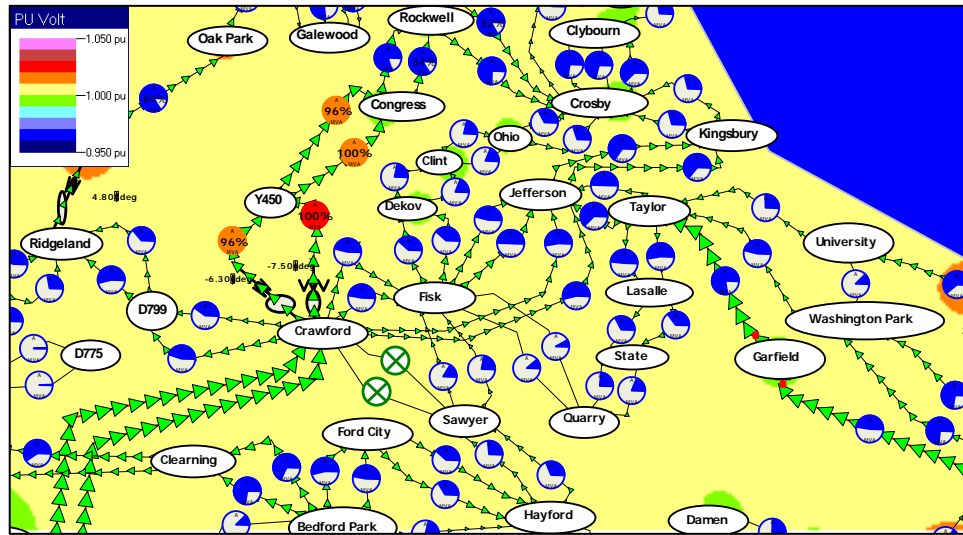


Figure 3.6: Contour with $g = \infty$

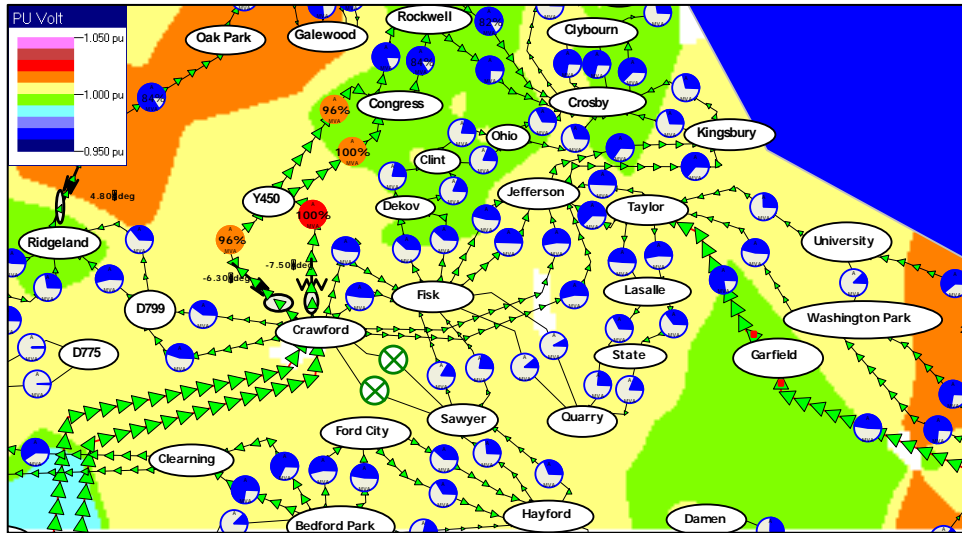


Figure 3.7: Contour with $g = 5$

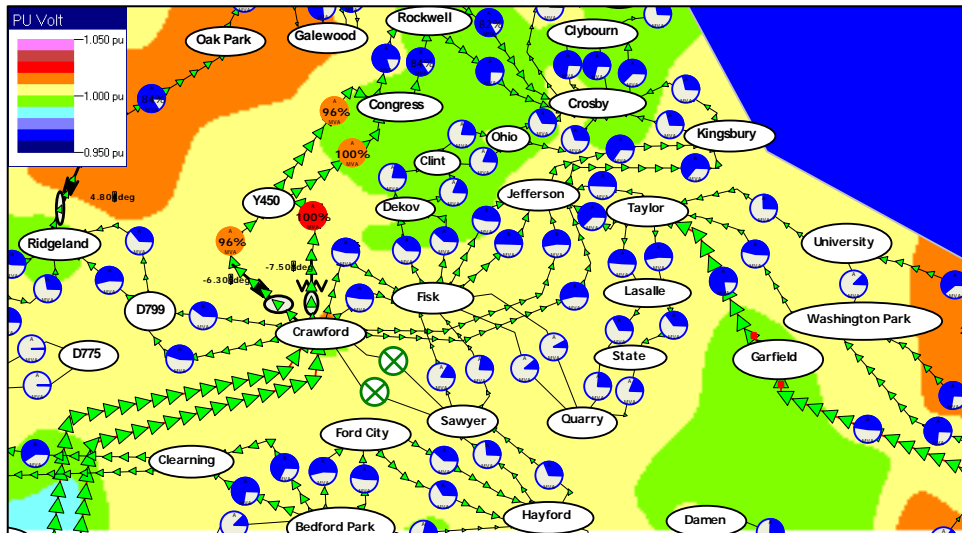


Figure 3.8: Contour with $= 10$

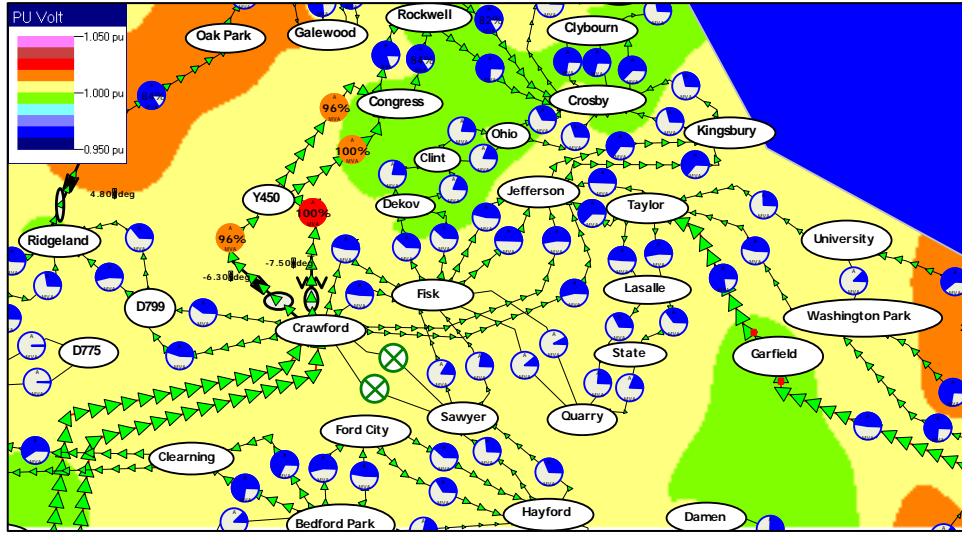


Figure 3.9: Contour with $g = 30$

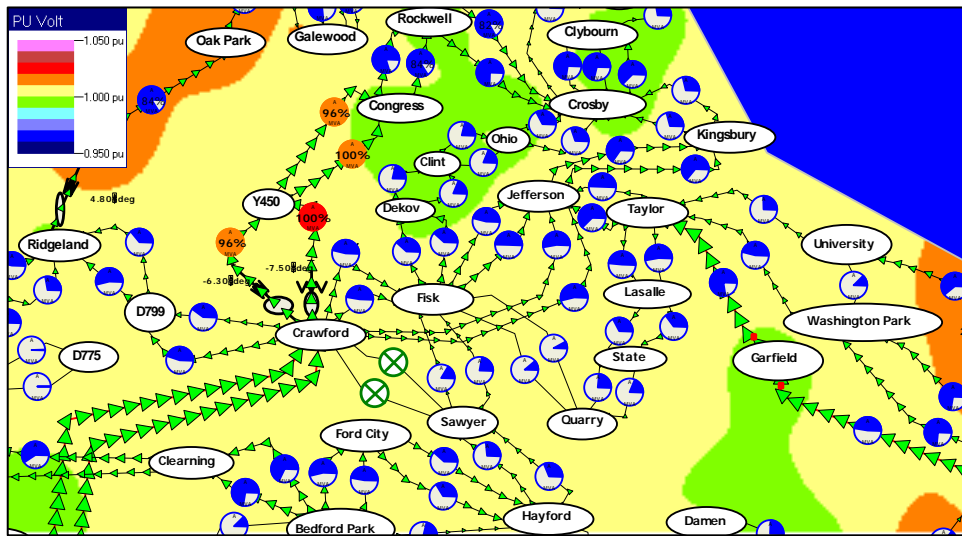


Figure 3.10: Contour with $g = 60$

Though this contour correctly shows the bus voltage values, it is difficult to draw conclusions about areas in the region. For the contours created using the Adaptive Algorithm (Figure 3.7-10), there are several large dark colored areas. Upon looking at the image, one immediately notices that the majority of the buses in these areas have voltage values that are between 0.99 p.u. and 1.00 p.u. or between 1.01 p.u. and 1.02 p.u. corresponding to the correct color mapped by the legend.

The above results indicate that the visualizations produced by the Adaptive Algorithm are easier to understand, making them, to some degree, better than those produced using the fast contouring algorithm. However, how do the Adaptive Algorithm images compare to each other? As g grows, the dark colored areas begin to shrink. This seems logical because, as g grows to infinity, the images grow toward the one in Figure 3.6, where the large dark colored areas do not exist. It is hard to say if any one of the Adaptive Algorithm images is better than all the others;

this is more of a human factors question. One result worth noting is in Figure 3.7 there are several areas where the pixels are uncolored (white). This makes the images less appealing. Perhaps it is better to use a larger value of g . The differences between the last three images appear to be marginal. Since Figure 3.8 is faster to create than Figure 3.9 and Figure 3.10, it may arguably be the best.

3.5 GPU-based Contouring

There are two key motivations for speeding up the rendering of contours in power system visualizations. First, increasing rendering speed leads to an enhanced feeling of interactivity when working with the visualization. To achieve a true feeling of interactivity, a rendering speed of 16 frames per second (fps) is considered a minimum. With traditional CPU-based rendering, the frame rates obtained are closer to 1 fps due to the large computational burden placed on the CPU. Secondly, the visualization rendering rate should be able to keep up with the underlying data rate. With the advent of newer, faster measurement devices and state estimators, it is possible to get data at a much faster rate than CPU-based contouring can handle. As an example, some phasor measurement units are capable of providing samples at 30 Hz. In order to visualize this data in real time, the rendering speed must be equal to or exceed 30 fps, assuming that one frame is rendered per sample time.

While CPU-based contouring methods have had trouble reaching such high rendering speeds, the use of the computation power contained within the graphics processing unit (GPU) (i.e., the display card) shows much promise. Virtually every video game released in the past few years has employed the significant parallel power of the GPU in order to increase rendering speeds. By employing the GPU in contouring, we hope to get significantly shorter rendering times in order to promote greater interactivity and data/visualization cohesiveness.

3.5.1 Advantage and disadvantages of GPU contouring

There are significant advantages and disadvantages of moving the contour calculations from the CPU to the GPU. As with any application, the tradeoff between these factors must be taken into account in order to determine if a GPU-based approach is the best approach.

The greatest advantage of GPU-based contouring is the ability of the GPU to perform parallel computations. A typical GPU contains multiple fragment and vertex shaders, each of which can operate independently on incoming data. This architecture, known as Single Instruction, Multiple Data (SIMD), can lead to dramatic increases in rendering speed if the rendering operations are easily parallelizable. This is in stark contrast to most CPUs, which employ a Single Instruction, Single Data (SISD) architecture which processes instructions in a serial rather than parallel fashion. Because the contouring algorithm we use can be easily parallelized, the GPU is able to take advantage of this parallelization whereas the CPU is not. It is because of this difference in parallelization that the GPU can achieve much quicker contour rendering. Another nice side effect of doing the contouring calculations on the GPU is that the CPU is then free to perform other tasks while the GPU performs the necessary calculations.

Although using the GPU can achieve faster rendering speeds, particularly when parallel computations must be performed, there are still some disadvantages to using the GPU. First, in order to achieve high rendering rates, 16-bit floating point numbers must be used. While most GPUs support 32-bit floating point operations, using these larger data types can slow rendering to a crawl. As a result of using 16-bit floating point numbers, it is easy to get into problems with

round-off error, leading to undesirable visual artifacts. Furthermore, because GPUs use an SIMD architecture, it is not possible to read and write to the same memory address while executing a program. Introduction of new OpenGL extensions such as framebuffer objects have made this less of a hassle, but having to read from and write to separate memory locations requires high memory allocation and can be difficult to program effectively. Also, because GPUs tend to have much less memory available to them than CPUs, care must be taken to avoid running out of memory.

3.5.2 Preliminary results

We have implemented GPU fragment shaders to perform Shepard's algorithm on an nVidia GeForce 7600 GT graphics card. These fragment shaders were written in the Cg programming language using 16-bit floating point numbers as mentioned above. For a large case with over 1000 buses, the GPU-based contouring was able to achieve rendering speeds above 20 fps. Also, for the one-line diagram used in the investigation of dynamic influence distances, rendering times as low as 0.002 seconds have been achieved with a 1920x1200 resolution. The extremely fast rendering rates are encouraging; however, much more work needs to be done in order to optimize the performance of the GPU-based contouring algorithm. With the latest implementation, there are visual artifacts present which must be addressed before the GPU-based contouring can be brought out of the lab and into the control room. Hopefully, we will be able to make suitable modifications to the current implementation such that decreases in rendering times do not require a significant decrease in the quality of the resulting contours. An example contour using this technique for a 37 bus system is shown in Figure 3.11.

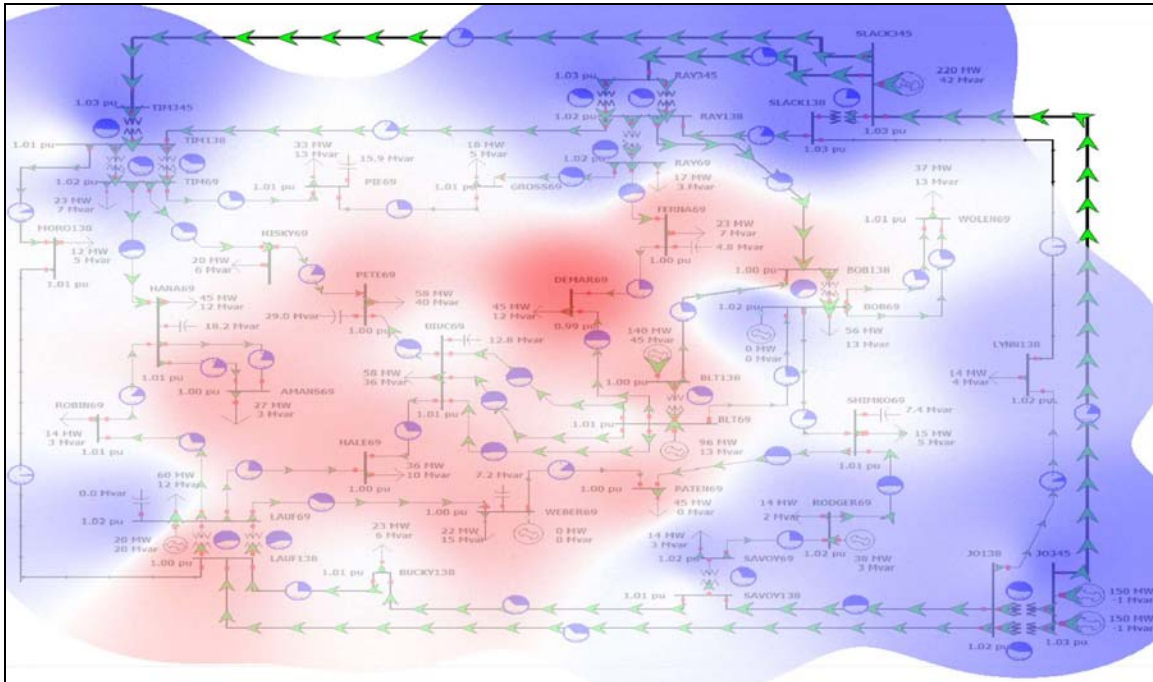


Figure 3.11: GPU-Based Contouring for 37 Bus System

4.0 Line Outage Detection Using PMU Data

The deployment of phasor measurement units (PMUs) throughout the power grid has increased substantially in recent years, and this growth is expected to continue. With these new measurement devices, new techniques must be developed to take advantage of the wealth of information that they provide. In particular, the voltage and current phasor angles obtained from these PMUs should be used to increase the situational awareness of grid operators. In this chapter we discuss how line outages can be identified due to changes in phasor angles observed at a limited number of buses. Using these techniques, it should be possible to get early indicators of line outages anywhere in the grid.

4.1 Problem Formulation and Theory

With this detection algorithm, we hope to provide indications of line outages on the system that would otherwise not be obtained as quickly (or at all, if the line is in an external system). In order to perform this task, we begin with the DC power flow equations for changes in power injection:

$$\mathbf{B}\Delta\theta = \Delta\mathbf{P} \quad (4.1)$$

Using the NERC System Data Exchange (SDX) along with existing study cases it should be possible for any control area to obtain the \mathbf{B} matrix used in equation (4.1). As discussed in the literature, the effect of an outage of a line in the system can be approximated by a power transfer between the terminal buses of the line that results in zero flow on the line. The necessary transfer from the “to” bus to the “from” bus on a line k , denoted as \tilde{P}_k , is related to the original line flow as follows:

$$\tilde{P}_k = \frac{P_k}{1 + PTDF_{k,k_{from}-k_{to}}} \quad (4.2)$$

where P_k is the pre-outage flow on the line defined as positive if flowing from the “from” bus to the “to” bus, and $PTDF_{k,k_{from}-k_{to}}$ is the Power Transfer Distribution Factor (PTDF) relating the change in flow on line k due to a transfer from line k ’s “from” bus (k_{from}) to its “to” bus (k_{to}). If this transfer across the terminal buses of line k is imposed on the system, then a change in angles at all buses will occur. This change in angles, denoted as $\Delta\tilde{\theta}^k$, is found by applying equation (4.1):

$$\begin{aligned} \Delta\tilde{\theta}^k &= \tilde{P}_k \mathbf{B}^{-1} \begin{bmatrix} 0 \\ 1 \\ -1 \\ 0 \end{bmatrix} \begin{matrix} \leftarrow k_{to} \\ \leftarrow k_{from} \end{matrix} \\ &= \tilde{P}_k \Delta\theta^k \end{aligned} \quad (4.3)$$

In this equation, $\Delta\theta^k$ is the angle change vector which would result from a transfer of 1 p.u. from the “to” to “from” bus of line k ; $\tilde{\Delta\theta}^k$ is obtained by simply multiplying $\Delta\theta^k$ by the actual value of P_k^o . We can then separate $\Delta\theta^k$ into two sets of angles—the changes in angles at buses where PMUs are located and the changes in angles at all other buses:

$$\Delta\theta^k = \begin{bmatrix} \Delta\theta_p^k \\ \Delta\theta_o^k \end{bmatrix} \quad (4.4)$$

In equation (4.4) and in the remainder of this chapter, the subscript p is used to refer to buses with PMUs, and the subscript o is used to refer to all buses without PMUs.

The next step is to consider the measured PMU phasor angle data. Once a discontinuity is detected in the phasor angles at one or more PMUs, the pre- and post-disturbance angles are subtracted from one another to give the observed angle change vector:

$$\Delta\theta_p^{obs} = \theta_p^{obs} \Big|_{\text{after disturbance}} - \theta_p^{obs} \Big|_{\text{before disturbance}} \quad (4.5)$$

With the observed angle change, $\Delta\theta_p^{obs}$, in hand, we can then try to determine which line outage caused this angle change. Even though neither the outaged line nor the pre-outage flow on the line is known, we can use the information we have to make a very good guess as to which line was outaged. In order to find the line l that was outaged, the following search is performed:

$$\text{line outaged } l = \arg \min_{k \in L} \left(\min_p \left\| \Delta\theta_p^{obs} - \Delta\theta_p^k \tilde{\mathbf{P}} \right\| \right) \quad (4.6)$$

where L is the set of all lines that we consider to be possibly outaged. The basic assumption underlying this search is that each line within the set L will give a unique change in angles $\Delta\theta_p^k$ regardless of the scaling performed on the angles. In other words:

$$m, n \in L, \text{ if } m \neq n, \frac{\Delta\theta_p^m}{\|\Delta\theta_p^m\|} \times \frac{\Delta\theta_p^n}{\|\Delta\theta_p^n\|} = 1 \quad (4.7)$$

If this assumption holds, then the inner minimization of equation (4.6) will result in unique values for all lines under consideration. If equation (4.7) does not hold, then there will be lines that will be very hard to distinguish when considering which one was outaged.

The search in equation (4.6) can be performed very quickly using dot products. To see why this is the case, consider two vectors, \mathbf{a} and \mathbf{b} . From linear algebra, we know that the projection of \mathbf{b} onto \mathbf{a} , $proj_{\mathbf{a}}\mathbf{b}$, is the vector that minimizes $\|\mathbf{b} - k\mathbf{a}\|$, where k is an arbitrary scalar value. The formula for calculating $proj_{\mathbf{a}}\mathbf{b}$ is:

$$proj_{\mathbf{a}}\mathbf{b} = k\mathbf{a} \quad (4.8)$$

$$k = \frac{\mathbf{a} \cdot \mathbf{b}}{\mathbf{a} \cdot \mathbf{a}} = \arg \min_{k \in \mathbb{R}} \|\mathbf{b} - k\mathbf{a}\|$$

Comparing equations (4.6) and (4.8), we can rewrite the inner minimization of (4.6) for a candidate line k as:

$$\begin{aligned}\tilde{P}_k &= \min_{\tilde{P}} \left\| \Delta\theta_p^{obs} - \Delta\theta_p^k \tilde{P} \right\| \\ &= \frac{\Delta\theta_p^{obs} \cdot \Delta\theta_p^k}{\Delta\theta_p^k \cdot \Delta\theta_p^k}\end{aligned}\quad (4.9)$$

We can then rewrite (4.6) using dot products, which leads directly to the algorithm used to determine the outaged line:

$$\text{line outaged } l = \arg \min_{k \in L} \left(\left\| \Delta\theta_p^{obs} - \Delta\theta_p^k \frac{\Delta\theta_p^{obs} \cdot \Delta\theta_p^k}{\Delta\theta_p^k \cdot \Delta\theta_p^k} \right\| \right) \quad (4.10)$$

Because $\Delta\theta_p^{obs}$ is a fixed vector and $\Delta\theta_p^k$ is scaled by the optimal value to minimize the difference between the two, the closeness of fit of the change in angles due to the outage of line k to the observed angle changes can be quantified by the distance between the normalized $\Delta\theta_p^{obs}$ and $\Delta\theta_p^k$ vectors. The error metric we use for ranking a possible line outage k is defined as the normalized angle difference (NAD_k):

$$NAD_k = \left\| \frac{\Delta\theta_p^{obs}}{\|\Delta\theta_p^{obs}\|} - \frac{\Delta\theta_p^k}{\|\Delta\theta_p^k\|} \right\| \quad (4.11)$$

Figure 4.1 shows the error metric and how it relates to the observed and expected angle changes. Clearly, the closer the fit between the observed and expected angle, the closer the NAD value should be to zero.

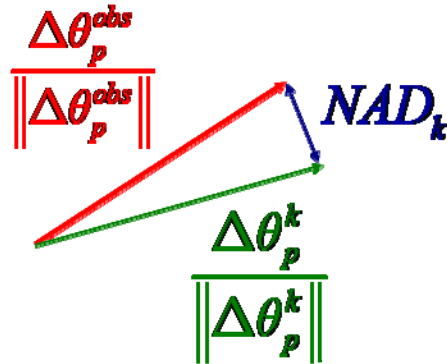


Figure 4.1: Normalized Angle Difference

4.2 Line Outage Detection Algorithm

In order to perform the search for which line is outaged, the following algorithm is used:

1. Calculate $\Delta\theta_p^{obs}$ using equation (4.5)
2. For each line k in the set of lines L :
 - a. Calculate $\Delta\theta_p^k$ using equations (4.3) and (4.4)
 - b. Calculate β_k^0 using equation (4.9)
 - c. Calculate the error between the measured and expected angle changes using the results from step 2a and 2b:

$$AngleError(k) = \|\Delta\theta_p^{obs} - \Delta\theta_p^k \beta_k^0\| \quad (4.12)$$

3. Determine the most likely line l that was outaged by sorting the vector $AngleError$:

$$l = \arg \min_k AngleError(k) \quad (4.13)$$

4. Determine the pre-outage flow on line l , P_l , using equation (4.2) and the results from step 2b:

$$P_l = \beta_l^0 (1 + PTDF_{l,l_{from}-l_{to}}) \quad (4.14)$$

The system **B** matrix must only be factored once and, once factored, can be quickly used to calculate $\Delta\theta_p^k$ in step 2a. Furthermore, this factorization (and the calculated values of $\Delta\theta_p^k$) must only be updated if a change in the **B** matrix occurs. Outside of step 2a, the algorithm requires only vector multiplications and one sort operation.

However, the algorithm is subject to several possible errors. First, the conditions under which the DC load flow equations hold (low impedance lines, small angle differences across lines, and voltages close to nominal) are necessary in order to treat the power system as a linear system. Because in a real system these conditions are never completely satisfied, error is introduced into the calculation of $\Delta\theta_p^k$ and β_k^0 . As a result, the calculated error values in equation (4.12) may not accurately reflect the relationship between line outage and angle changes, leading to inaccurate line rankings. Another possible source of error is in the determination of $\Delta\theta_p^{obs}$, the observed change in angles vector. Filtering and disturbance detection can both have an impact on the accuracy of $\Delta\theta_p^{obs}$, which would ideally represent the steady-state change in phasor angles due to the line outage.

Another possible concern with the algorithm is when multiple lines cause similar changes in phasor angles at the PMU buses. Because arbitrary scaling is performed on the vector $\Delta\theta_p^k$, any

lines a and b such that $\frac{\Delta\theta_p^a}{\|\Delta\theta_p^a\|} \cdot \frac{\Delta\theta_p^b}{\|\Delta\theta_p^b\|} \approx 1$ are indistinguishable in deciding which one was

outaged. However, as more PMUs are deployed on the grid, the chances of this happening should

decrease. Also, by comparing the differences in $\frac{\Delta\theta_p}{\|\Delta\theta_p\|}$ for all lines based on different PMU

placements, it should be possible to guide future placement of PMUs for line outage detection.

Because of these complicating factors, modifications were made to the algorithm during implementation. The first modification is based on the observation that lines which require pre-outage flows exceeding known line limits are most likely not the outaged lines. For example, if the pre-outage flow on a line would have to be 100 GW in order to get the observed change in angles, that line is probably not the outaged line. Therefore, lines with pre-outage flows above a cutoff value are removed from consideration after step 2. For the examples given below, the cutoff was set to twice the line limit or 10,000 MW if a line limit was not known.

In addition to this refinement, the pre-outage flows (calculated using equation (4.14)) are presented along with the line rankings. This allows the user to use engineering judgement in deciding if pre-outage flows are reasonable. This is accomplished by replacing step 3, which initially provided only the most likely line to be outaged, by a set of instructions which returns the X most likely lines to have been outaged:

3'. For $rank = 1$ to X

- a. $LineWithRanking(rank) = \arg \min_k AngleError(k)$
- b. Remove $AngleError(rank)$ from $AngleError$ vector

With this modification, line l from step 3 of the initial algorithm definition becomes $LineWithRanking(1)$. In the actual system example, X was set to ten to see the ten most likely lines to have been outaged (e.g., see Table 4. below).

4.3 Test Case

In order to gauge the usefulness of the algorithm on a large-scale system, we tested it with real data obtained from TVA. Calculation of the expected angle changes for each line considered were performed using the \mathbf{B} matrix from an up-to-date state estimator case. The observed angle changes, $\Delta\theta_p^{obs}$, were determined from actual PMU data.

Figure 4.2 shows the voltage phasor angles at the system's PMU buses before and after the opening of a 500 kV line. The data resolution in this figure is 30 samples per second. In order to determine the change in angles at each of the buses, the angles were filtered on both sides of the disturbance using a weighted averaging of 30 samples to eliminate oscillations and noise. The voltage phasor angles obtained after filtering are shown in Figure 4.3. After filtering, the angles one second after the disturbance were subtracted from the angles one second before the disturbance to obtain $\Delta\theta_p^{obs}$.

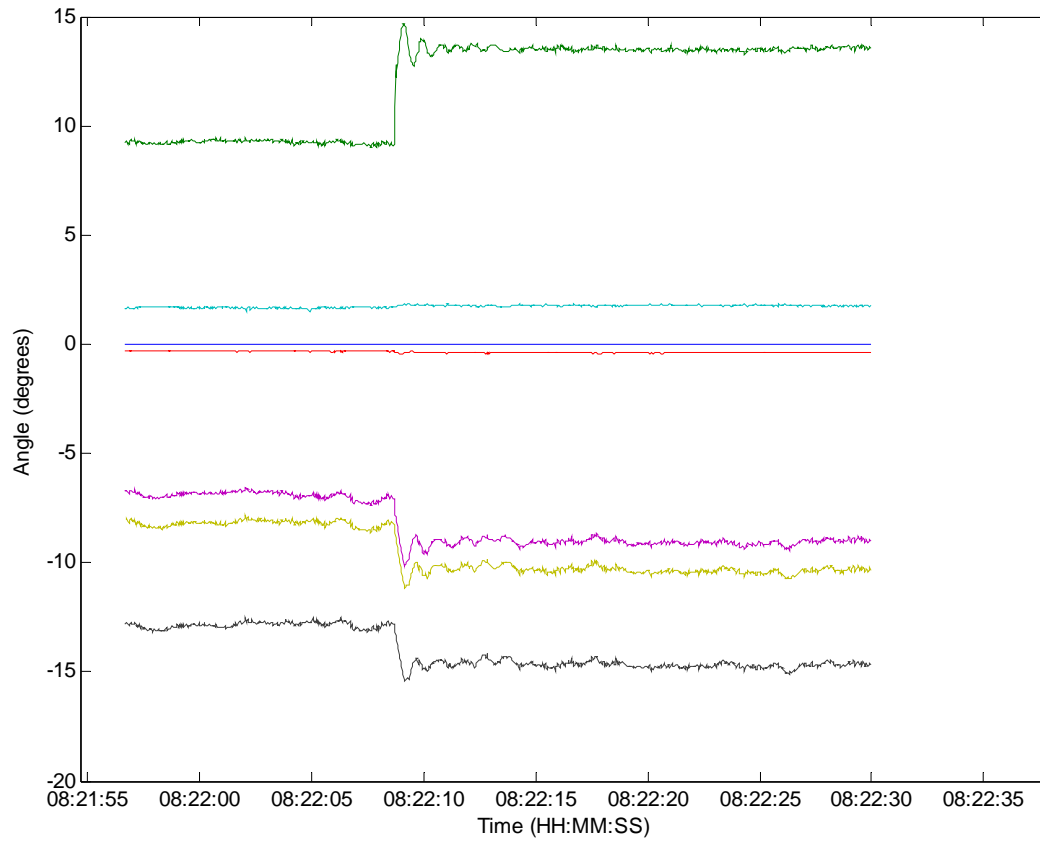


Figure 4.2: Voltage Phasor Angles at PMU Buses

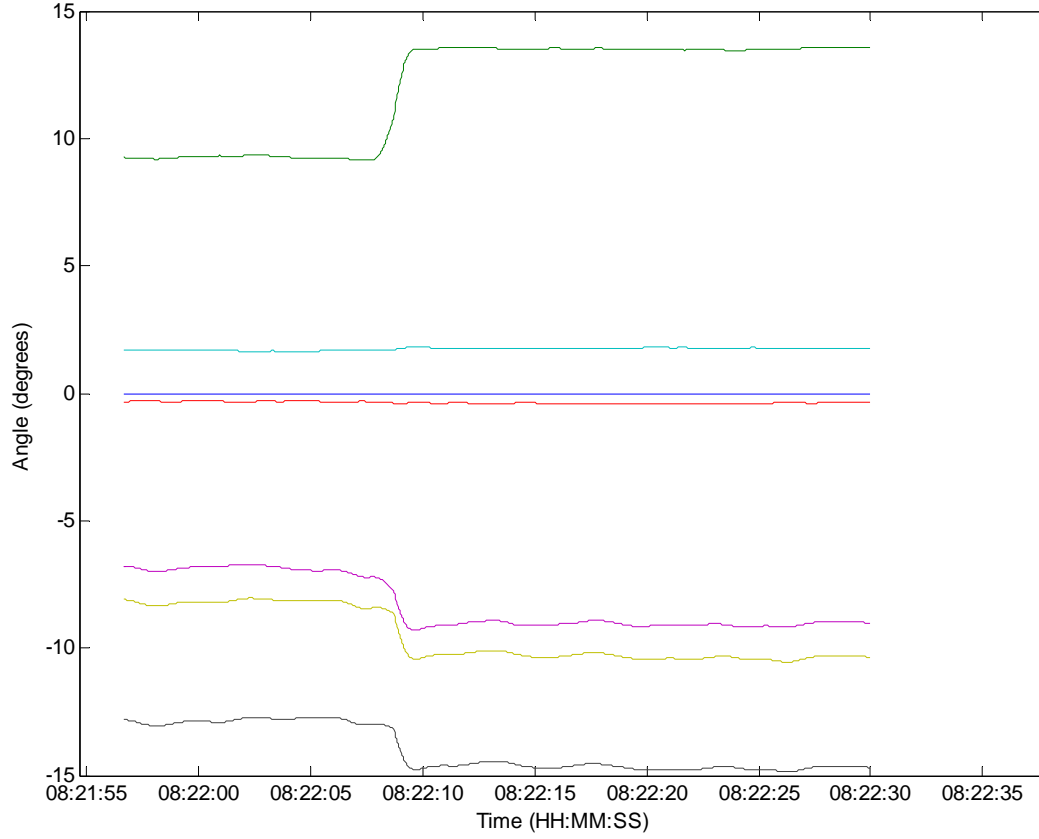


Figure 4.3: Voltage Phasor Angles at PMU Buses, Filtered

Using the full set of PMU voltage phasor angles, the outage was detected with little trouble. Table 4. shows the the top ten (sorted by NAD) lines, with the line that was outaged highlighted in bold. According to the state estimator case, the flow on the line before the outage was 1089 MW. The algorithm calculated the pre-outage flow to be 1005 MW, therefore the percent error is only 7.7%. Table 4.1 also shows that the normalized angle distance increases rapidly, indicating good differentiation between different line outages.

Table 4.1: Algorithm Results Using All Phasor Angles

Rank	Line number	NAD	Pre-outage flow on line (MW)
1	1466	0.028	1005.3509
2	4801	0.325	-2576.4177
3	1708	0.536	1025.9054
4	3118	0.584	-4586.4965
5	1625	0.616	-855.6809
6	3420	0.644	1847.8298
7	1448	0.658	603.0468
8	2275	0.665	-751.2777
9	1764	0.678	-2240.7109
10	3124	0.703	-3962.6182

The algorithm was also run using all phasor angles except for the one with the largest change (the top-most angle plot in Figure 4.3). The correct outaged line was detected as shown in Table 4.2, but the difference between successive normalized angle distances is much smaller when compared to the results from Table 4.1. Also noteworthy is that the calculated pre-outage flow is still very close to the actual value of 1089 MW.

Table 4.2: Algorithm results using reduced phasor angle set

Rank	Line number	NAD	Pre-outage flow on line (MW)
1	1466	0.012	972.0643
2	1685	0.027	673.4778
3	2614	0.035	4284.1793
4	2622	0.043	-4222.9484
5	1684	0.060	974.1054
6	1343	0.080	4724.7594
7	72	0.086	-4282.2886
8	710	0.107	894.8055
9	4080	0.109	-3597.6625
10	706	0.110	2654.7599

A final test was run to see the impact of the cut-off process described above. Using the full PMU data set, the algorithm was run without taking into account line limits or extremely high flows. The results are shown in Table 4.3. Comparing these results to those of Table 4.1, it is clear that checking to see if pre-outage flows are above a certain cut-off value, whether it is based on known line limits or a fixed number, can aid substantially in differentiating between which lines could have caused the observed angle change.

Table 4.3: Algorithm results using all phasor angles, without line cut-off checks

Rank	Line number	NAD	Pre-outage flow on line (MW)
1	1466	0.028	1005.3509
2	5264	0.067	3787.8794
3	5211	0.088	-343482.2388
4	3298	0.088	-343493.9092
5	1649	0.088	-343493.9092
6	2103	0.182	-188572.2537
7	364	0.185	27537.4776
8	4192	0.186	-37230.4475
9	2114	0.204	-5368.9884
10	959	0.204	5368.9876

4.4 Future Work

While we are pleased with the results obtained thus far, more work needs to be done before this algorithm can be used in a real-time system. Some of the issues we wish to explore in the future are:

- The practicality of checking for the simultaneous outage of more than one line
- How to best detect events and calculate $\Delta\theta_p^{obs}$ using real, noisy data

- The incremental benefit of adding a PMU at a particular location
- Sensitivity to errors in the **B** matrix

5.0 PMU Voltage Angle Visualization

PMUs are beginning to be deployed widely in the power system, which gives system controllers the ability to directly measure phase angles. PMUs also provide data at a much faster rate than traditional SCADA systems, which gives the ability to see higher frequency phenomena. However at present, PMUs are only deployed at a small percentage of buses. This presents a challenge: how to get useful information from the small number of data points.

This chapter discusses the work that has been done on visualizing the new data provided by PMUs. The first section of this chapter discusses the problems surrounding the visualization of PMU data. The second section discusses the application of equivalent circuit theory to arrive at equivalent injections. Next, difference contours are introduced as a way to alert operators to important changes without cluttering the control room. Then, these ideas are applied to several power flow cases from the August 14, 2003 blackout. Finally, conclusions and future work are discussed.

5.1 Problem Overview

As mentioned above, the problem is to get as much useful information from PMUs as possible. The most straightforward approach is to add the PMU angles measurements as inputs into the state estimator, and this work is being done as part of other projects. This chapter discusses an approach to visualizing PMU data. The set of PMU measurements is much smaller than the total number of buses, making state estimation impossible.

This chapter begins by exploring the meaning of a particular PMU measurement (i.e. what does a particular measured angle mean?). To do this, we will use the system B matrix and equivalent circuit theory to examine the mapping between the PMU measurements and bus injections.

5.2 Equivalent Circuit Theory

Equivalent circuit theory was developed as a way of removing external areas from a power system model in order to reduce the problem size. We will make use of it to reduce the system down to a set of PMU buses. Starting with the linear circuit model

$$\mathbf{B}\boldsymbol{\theta} = \mathbf{P} \quad (5.1)$$

the vector of bus angles and injections are partitioned into PMU buses and non PMU buses

$$\begin{bmatrix} \mathbf{B}_{pp} & \mathbf{B}_{po} \\ \mathbf{B}_{op} & \mathbf{B}_{oo} \end{bmatrix} \begin{bmatrix} \boldsymbol{\theta}_p \\ \boldsymbol{\theta}_o \end{bmatrix} = \begin{bmatrix} \mathbf{P}_p \\ \mathbf{P}_o \end{bmatrix} \quad (5.2)$$

where the subscript p denotes values associated with PMU buses and the subscript o is used to denote values at non PMU buses. Now, (5.2) can be rewritten as

$$\left[\mathbf{B}_{pp} - \mathbf{B}_{po} \mathbf{B}_{oo}^{-1} \mathbf{B}_{op} \right] \boldsymbol{\theta}_p = \left[\mathbf{P}_p - \mathbf{B}_{po} \mathbf{B}_{oo}^{-1} \mathbf{P}_o \right] \quad (5.3)$$

This expression has reduced the system so that the system states are the equivalent power injections at the PMU buses and the angles at the PMU buses. So, we have

$$\mathbf{B}_{equiv} \boldsymbol{\theta}_p = \mathbf{P}_{equiv} \quad (5.4)$$

where

$$\mathbf{P}_{equiv} = \mathbf{P}_p - \mathbf{B}_{po} \mathbf{B}_{oo}^{-1} \mathbf{P}_o \quad (5.5)$$

and

$$\mathbf{B}_{equiv} = \mathbf{B}_{pp} - \mathbf{B}_{po} \mathbf{B}_{oo}^{-1} \mathbf{B}_{op} \quad (5.6)$$

Equation (5.3) gives a way to map the angles measured by PMUs into injections. For a single line, the power flow across a single line is roughly proportional to the angle difference across the line. However, there is no clear interpretation to an angle difference that is not across a single line. We have found that mapping the measured (PMU) angles to equivalent injections yields diagrams that are easier to interpret. Of course, when this mapping is preformed one must be mindful of the changes that are introduced. To explore this mapping we first define

$$\mathbf{M} = \mathbf{B}_{po} \mathbf{B}_{oo}^{-1} \quad (5.7)$$

Now, we can see that

$$\mathbf{P}_{equiv} = \mathbf{P}_p - \mathbf{M} \mathbf{P}_o \quad (5.8)$$

which indicates that the equivalent injections are a function of the injections at PMU buses, \mathbf{P}_p , and the injections at non PMU buses modified by the matrix \mathbf{M} . The matrix \mathbf{M} describes the influence of the non PMU buses on the PMU buses. The number of rows in \mathbf{M} is equal to the number of PMU buses, and the number of columns in \mathbf{M} is equal to the number of non PMU buses. So, \mathbf{M} is a very short and wide matrix. From (5.7) it is evident that \mathbf{M} is purely a function of the subcomponents of the system \mathbf{B} matrix, which means that for a given set of PMU buses \mathbf{M} is constant.

The rows of \mathbf{M} determine how injections at non PMU buses map to injections at PMU buses. In other words, the rows of \mathbf{M} determine how loads and generation at non PMU buses show up at PMU buses. This is illustrated using the 7-bus case shown in Figure 5.1.

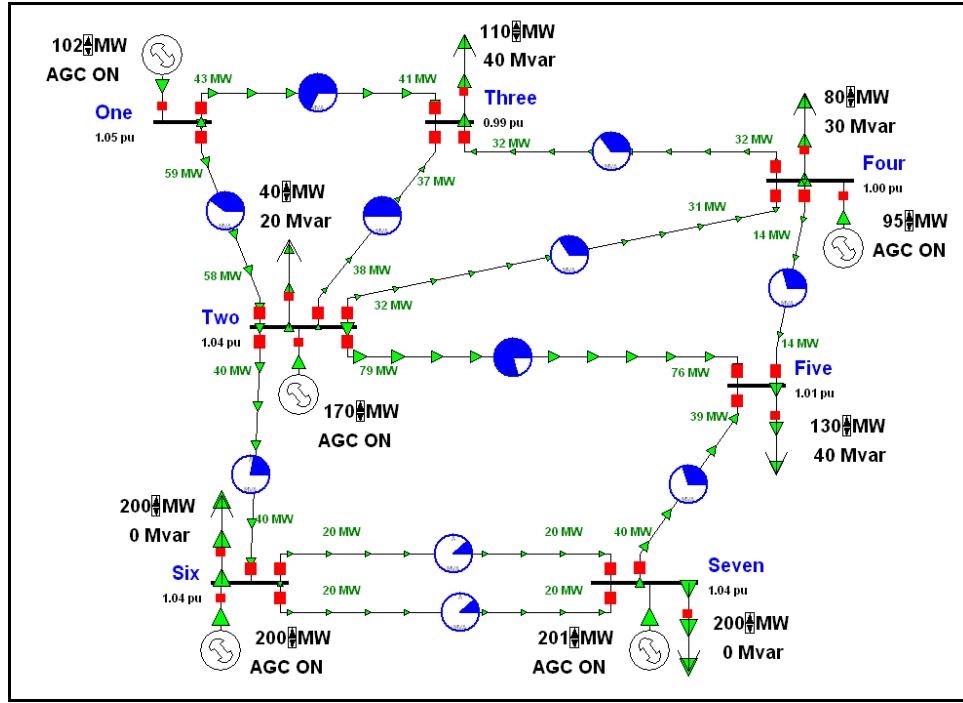


Figure 5.1: 7-bus sample case

The set of non PMU buses, P_o , is defined as buses 2, 3, 5, and 7. PMUs are at buses 1, 4, and 6. For this system the \mathbf{M} matrix can be calculated as

$$\mathbf{M} = \begin{bmatrix} -0.3463 & -0.0989 & -0.1415 & 0 \\ -0.2224 & -0.2064 & -0.8029 & 0 \\ -0.3355 & -0.0959 & -0.0433 & 0 \end{bmatrix} \quad (5.9)$$

The column of zeros corresponds to the slack bus (bus 7). The rows correspond to the PMU buses. For example, row 1 corresponds to bus 1 and row 2 corresponds to bus 4. Row 1 describes how injections at the non PMU buses (2, 3, 5, and 7) map to an injection at bus 1. Contours can be used to illustrate this. Figure 5.2 shows a contour of row 1 of (5.9). Bus 1, the blue bus, has been assigned a value of 1.0 because an injection at bus 1 will impact bus 1 with the total value of the injection. This also helps to make the bus of interest easily visible. The red shading indicates how much a bus impacts an equivalent injection at bus 1.

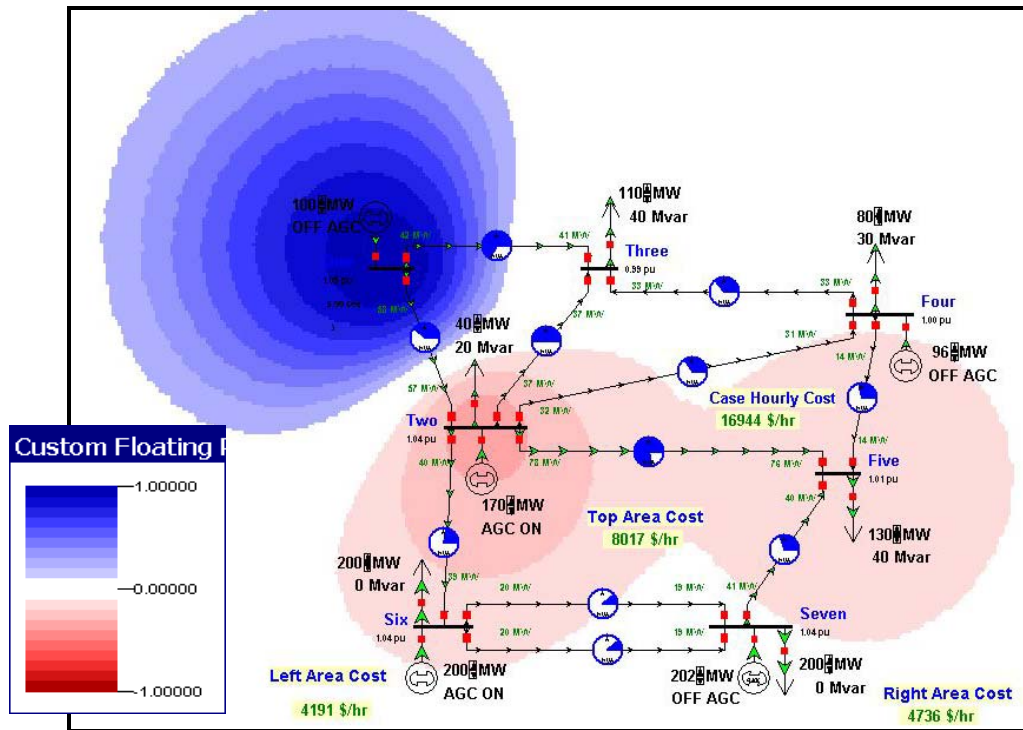


Figure 5.2: 7-bus sample case row contour

After examining Figure 5.2, it can be seen that bus 2 impacts the equivalent injection more than bus 5. This is reasonable because bus 2 is closer than bus 5. This trend remains true in larger cases as well. Figure 5.3 shows a row contour for the area surrounding the PMU bus 05KAMMER, which is located along the Ohio West Virginia border. This contour shows that the non PMU bus injections that map to the PMU bus at 05KAMMER are fairly diffuse. However, the contour is clearly darker around the high voltage buses near to the 05KAMMER bus.

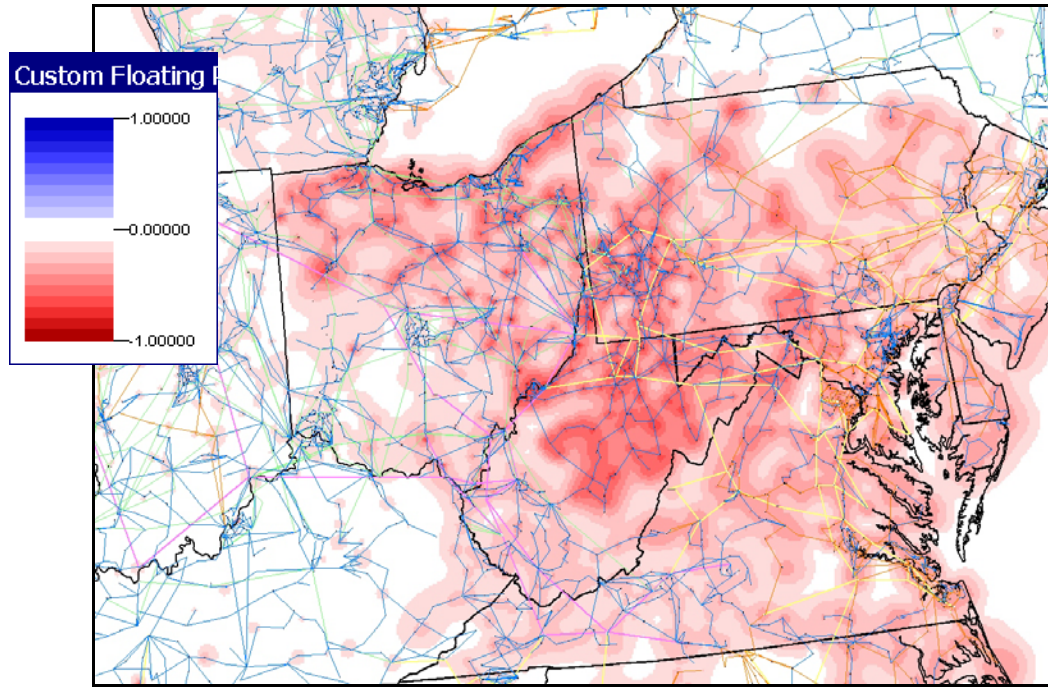


Figure 5.3: Large case row contour

The columns correspond to non PMU buses. So, column 1 of (5.9) corresponds to bus 2. The columns of M tell how PMU injections map to non PMU buses. This information can be used to answer the question: what buses are responsible for the equivalent injection at this (PMU) bus? Figure 5.3 contains a contour of the column 1 (bus 2) values. This contour shows that the injections at bus 2 are caused by injections at buses 1, 4, and 6. The contour also indicates that the closer buses have more of an impact.

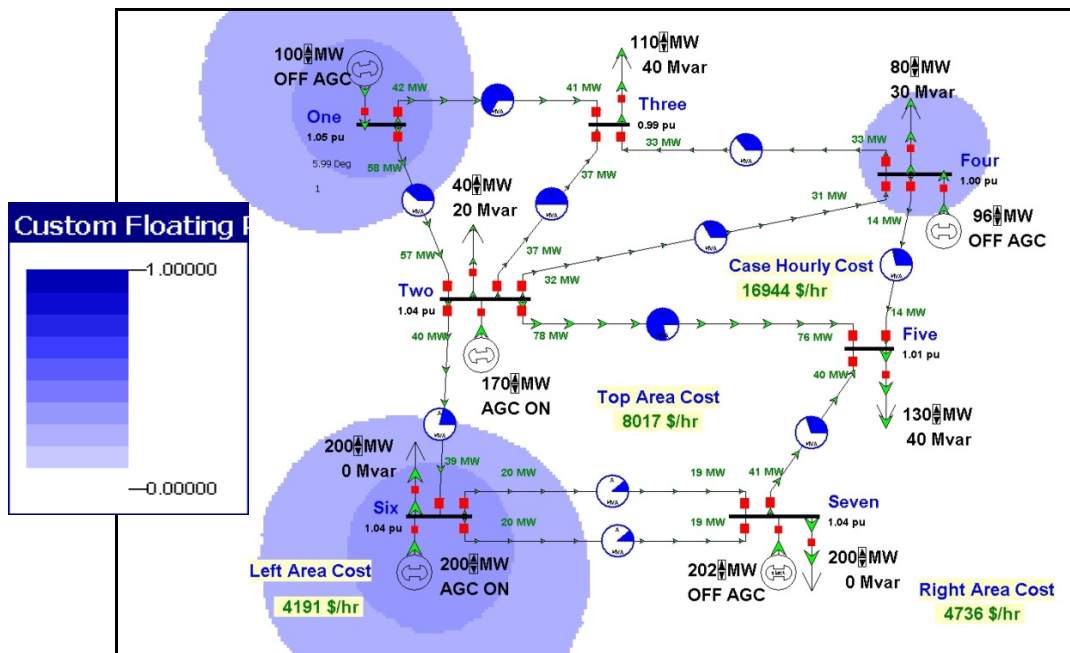


Figure 5.4: 7-bus sample case row contour

The large case column contour does not show the same diffuse properties as the large case row contour. For example, Figure 5.4, which contains the column contour corresponding to the bus 05KAMMER1, shows that the contour values are localized. 05KAMMER1 is a generator bus nearby the 05KAMMER PMU bus.

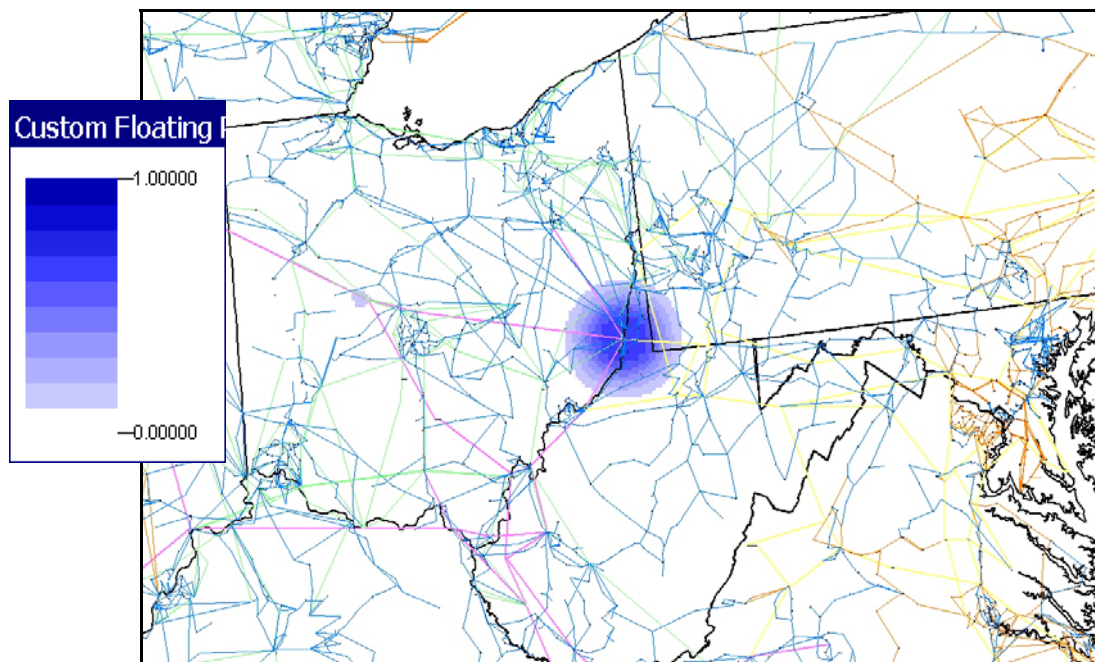


Figure 5.5: Large case row contour

5.3 Difference Contours

Because it is not possible to know the complete set of system values (e.g. line flows and bus voltages) when the only data is provided by PMU measurements, it may be more useful for operators to be alerted only when something changes. System operators are not generally concerned with the specifics of the areas outside of their control. However, when something changes, it may indicate a problem that they would like to know about. This is the motivation behind difference contours. Difference contours are simply contours—like the ones commonly done for voltages—that contour a change rather than the actual value. When everything is operating normally, the screen can be calibrated to be as empty as possible, indicating that no large changes have taken place recently.

Difference contours are a way of indicating temporal data without showing a movie. Moves are the traditional way of showing a change over time. The looping weather maps are probably the best example of this. However, in a control center this kind of display may make things very busy. Difference contours indicate change over time in a single static image by taking the difference between data points taken at two different times.

Difference contours have the advantage of brining out information that is not normally perceptible. For example, if the load at bus 2 is changed from 40 MW (left) to 45 MW (right), the change in the contours shown in Figure 5.5 are not readily visible in a contour of the bus injections. The only difference is a slight change in the hue of regions surrounding bus 2 and bus 7. There is a change at bus 7 because it is the slack bus, so it is automatically redispatched to serve the increase in load at bus 2. These small changes in color are not easy to perceive. However, when the difference is contoured, as shown in Figure 5.6 the differences are immediately apparent.

5.4 Blackout Case Results

In this section, the equivalent circuit ideas presented earlier in this chapter are combined with the difference contours. It was assumed that the voltage angles are known at PMU buses and their neighbors. For the blackout cases, there are 89 buses out of the 43,133 in the case that are reporting a voltage angle. In other words, only 0.206% of the buses have associated angle measurements. Clearly this is an extremely underdetermined system.

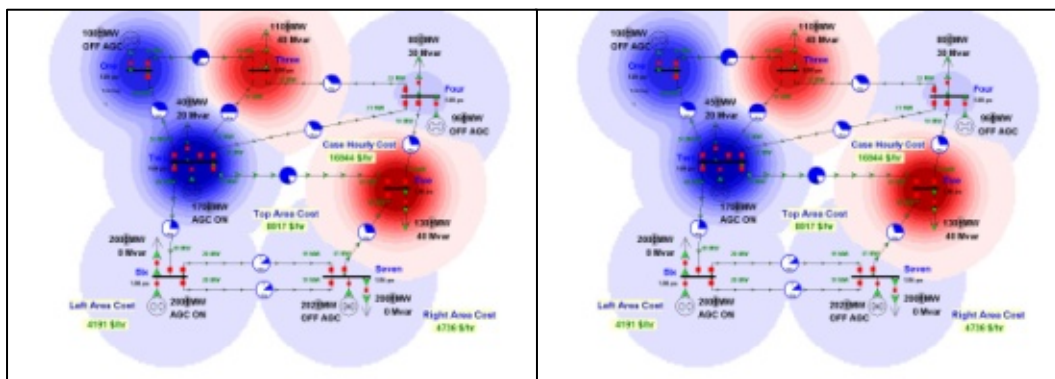


Figure 5.6: 7-bus injection contours

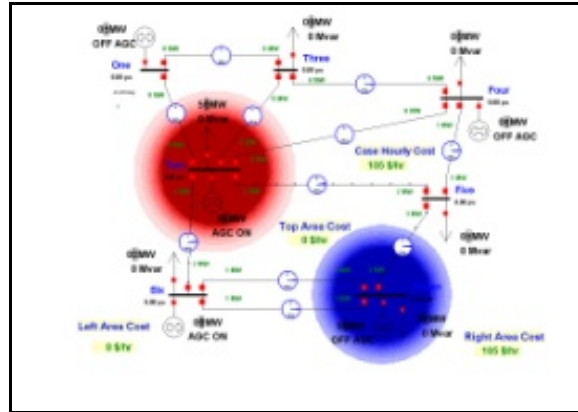


Figure 5.7: 7-bus injection difference contours

Four cases were considered from August 14, 2003. These cases are from 15:00, 15:05, 15:45, and 16:05. According to *The Blackout Report*, the system was in a relatively safe state between 15:00 and 15:05. Between 15:05 and 15:45 things begin to take a turn for the worse. During this time period, three 345 kV transmission lines opened because of contact with trees. In this time period, it is conceivable that a major blackout could have been averted. Between 15:45 and 16:05 things were out of control. Approximately 16 transmission lines were lost because of a cascade of overloads. At this point, a blackout would have been almost impossible to stop.

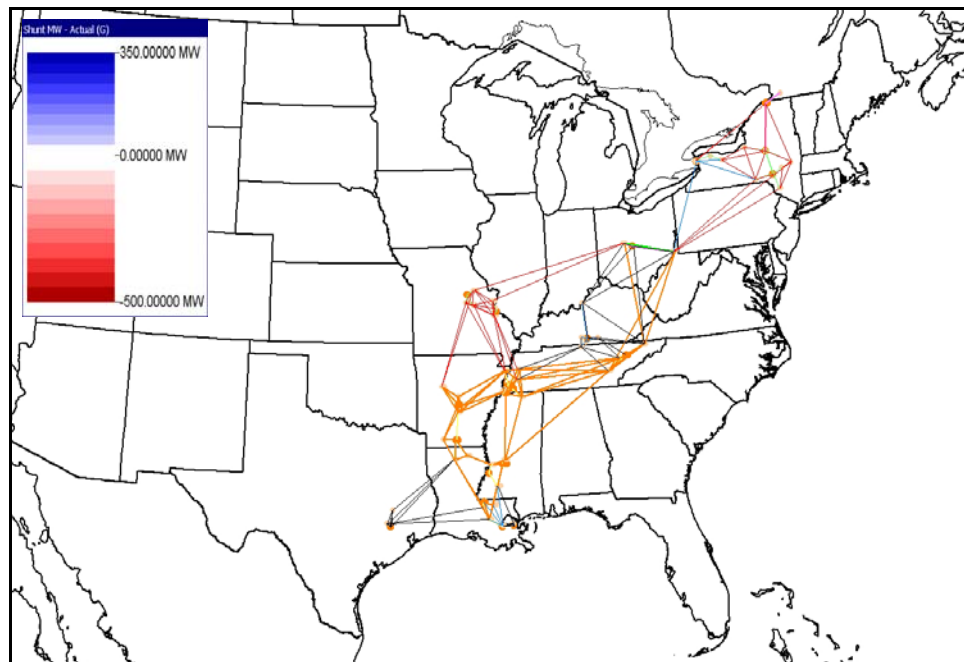


Figure 5.8: August 14, 2003 Blackout Case 1 - 15:05 to 15:00 difference

Figure 5.8 shows the difference contour for the equivalent PMU buses between 15:05 and 15:00. The difference contour does not show any significant changes occurring between 15:00 and 15:05. Indeed, there were not significant changes to the system during this period. This is reflected in the difference contour by the fact that there are no contours on the one-line diagram.

An operator seeing this diagram would be able to accurately conclude that nothing much had happened during this time period.

After the outage of the three 345 kV transmission lines, the system states had changed a good deal. This can be seen in the difference contour between 15:05 and 15:45, which is shown in Figure 5.9. It is particularly interesting that the contours show a change in the central Ohio region where conditions are beginning to deteriorate. The fact that this contour shows something significant happening in the right location gives a strong indication that the combination of the difference contours and system equivalents yields useful results. An operator who sees Figure 5.10 would not know exactly which lines had opened, but he or she would know that something was going on, prompting them to investigate further.

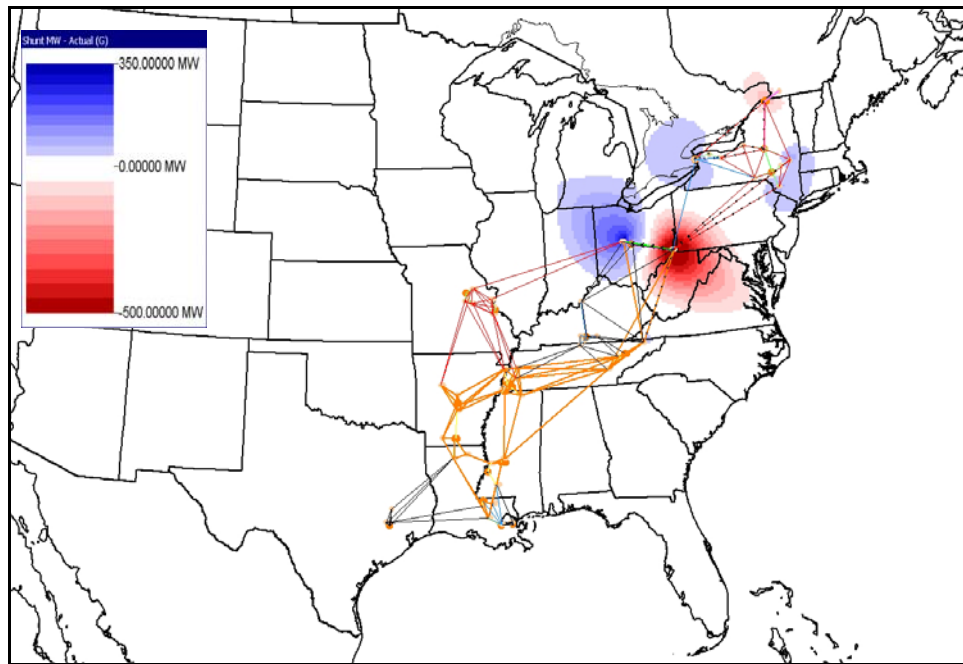


Figure 5.9: August 14, 2003 Blackout Case 2 - 15:45 to 15:05 difference

The final time period considered was between 16:05 and 15:45. This contour is shown in Figure 5.9. During this time period many small lines were outaged as the system cascaded toward the blackout that would occur in about 6 minutes. This contour does not show the same magnitude of change as the time period between 15:45 and 15:05, but there is clearly something going on. Again, the changes are seen in central Ohio and West Virginia. However, by this point, there is little time for operators to respond.

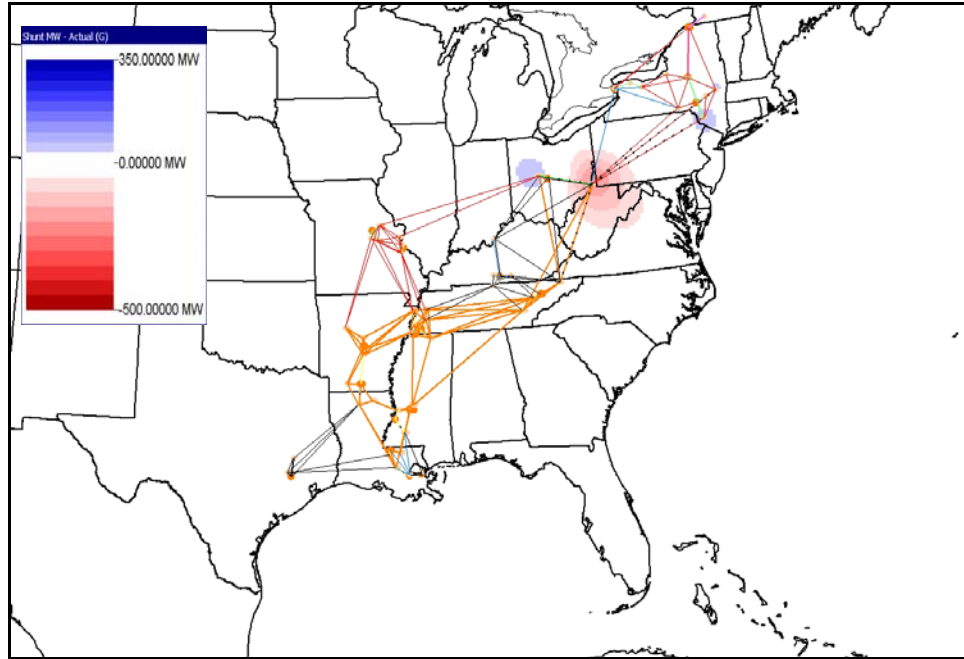


Figure 5.10: August 14, 2003 Blackout Case 3 - 15:45 to 16:05 difference

5.5 Conclusions

PMUs are beginning to provide direct measurement of the phase angles on the power system. This chapter has explored methods to tease useful information out of this data. Circuit equivalents were used to reduce the system down to a small system consisting only of PMU angles and equivalent injections. The idea of differencing contours was introduced to show trends without the need for movies and looping. This helps to keep the visual clutter down. Finally, the circuit equivalents and difference contours were combined and applied to several cases from the August 14, 2003 blackout. The difference contours of the equivalent blackout cases showed something happening in the right place at the right time.

5.6 Future Work

The results presented in this paper are for several static snapshots (i.e. four blackout cases). Once enough PMU data has been obtained, the ideas presented in this chapter can be tested using real data. When this is done it will be necessary to consider the effects of missing data and the incoming data rate. It would also be useful to extend these methods to allow for the display of limit violations. Further work is also needed to explore the effects of errors in the B matrix on the resulting equivalent flows.

6.0 Human Factors Testing

The human factors contributions to this research consisted of evaluation of the Line Overload Correction Form (LOCF) from Chapter 2, including how it is used with the one-line diagram, and development of a prototype demonstrator display that incorporated key human factors principles in its design.

6.1 Human factors challenges in display design

The primary challenge in the design information displays for power transmission control room applications is the mapping of system variables to graphical variables, subject to the constraints of human perceptual and cognitive capabilities. This challenge arises from the asymmetry between the very large number of system variables operators must monitor and the very limited number of graphical elements than can be used on the displays. Two main problems that degrade the readability of displays and that are to be avoided in display design are visual ‘noise’, which may result from careless use of animation and color, and clutter, resulting from displaying too much information in too small display space. These present-day challenges are further aggravated by the future need to display predicted values (to augment human working memory in extrapolating system states into the future), visualizing dynamic information, and in particular, rate of change information, and displaying of uncertain (probabilistic) and old (unreliable) information. Figure 6.1 illustrates the display design problem of mapping system variables into (visual) graphical variables, subject to the human factors design guidelines.

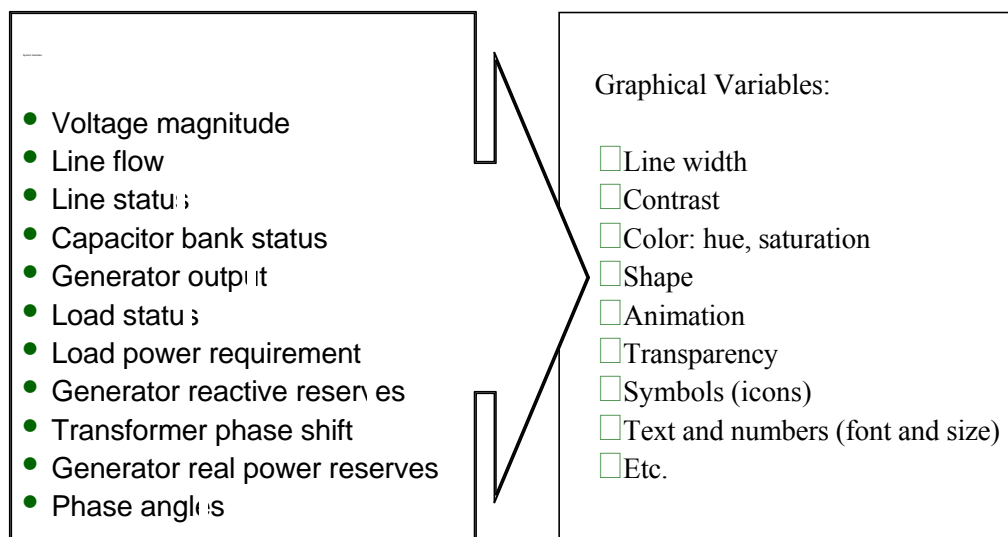


Figure 6.1: Illustration of display design problem

To determine the most important system variables to be displayed on the prototype display, a survey was done at the ABB User's Group Spring 2006 Meeting in Chicago, IL, on June 12, 2006. The survey consisted of 19 power systems variables and the respondents were asked to rank them according to their importance to them. Altogether 16 operators (including both reliability coordinators and transmission operators) responded, the results are depicted in Table 6.1. below.

Table 6.1 Ranking of power systems variables

by importance (1) by experienced power system operators (n = 16).

Mean Rank	Variable name and units
3.8	Voltage magnitude: p.u. (per unit)
4.4	Line flow
4.5	Line status: Open or Closed
4.6	Line flow: % loading, (MVA/max MVA)
4.8	Generator output: MW or MVAR
4.9	Generator status: Disconnected or Connected to the grid
4.9	Line flow: real power (MW)
5.1	Line flow: current (A)
5.6	Line flow: complex power (MVA)
5.9	Line flow: reactive power (MVAR)
7.1	Generator reactive reserves (delta MVAR)
7.3	Load status: Disconnected or Connected to the grid
7.9	Load power requirement: MW or MVAR
8.3	Capacitor bank status: MVAR;
8.3	Generator real power reserves (MW)
10.5	Phase angles (degrees or radians)
10.5	Phase angle differences between buses
12.2	Transformer phase shift (degrees or radians)
12.3	Transformer turns ratio

6.2 Human factors principles in display design

The purpose of information displays in control room applications is twofold: they should enhance human capabilities on one hand and alleviate their limitations on the other. A particularly critical aspect of information displays and a useful metric in their evaluation is Information Access Cost (IAC). IAC may be quantified in different ways, for example number of saccades (rapid eye movements) necessary to locate information the operator is seeking and the dwell time needed to perceive and understand the information, or the number of menus and mouse-clicks necessary to find the information if it is not immediately visible. A general and very versatile way of measuring IAC is in terms of time required to obtain a given piece of information from the display. Information display design should hence seek to reduce IAC in during emergencies and in situations subjected to time pressure. Displays should further prevent human errors, or help in error detection, or mitigate error consequences. Novel display designs should never introduce new types of errors.

Human information processing has enjoyed sustained attention since the World War II, and results of these research efforts have been documented in many handbooks and manuals (for example, [6]). Many display design principles are so fundamental to human perceptual and cognitive performance that they are generalizable across domains and specific applications. These principles are reproduced here in the next three sections.

6.2.1 Basic display design principles

In [7] thirteen of the most basic display design principles are arranged in four groups, according to the components of the human information processing system:

i. Perceptual principles:

(1) Principle of *legibility* (or, *audibility*): Clearly, for the display to be useful, the information on it must be legible to those using it and under the conditions it is used. Many factors affect legibility, however: the visual angle subtended by details (e.g., text and symbols), luminance, glare, and contrast (both color- and spatial contrast).

(2) Principle of *absolute judgment limits*: Operators should not be required operators to make decisions based on a single dimension of a variable, for example, judge the hue of color without a reference. See also P5.

(3) Principle of *top-down processing*: Operator experience and existing conventions should be heeded in display design, that is, the design should conform to operators' expectations.

(4) Principle of *redundancy gain*: Whenever possible, redundant coding of critical variables should be provided, for example, color should be accompanied with unique shape or position of the signal. See also P2.

(5) Principle of *discriminability*: Similar signals can be confused; therefore different signals must be clearly differentiated.

ii. Mental model principles:

(6) Principle of *pictorial realism*: The display should look like what it is representing, for example the geographic data view (GDV) presenting power transmission lines on a map closely approximating the physical layout of the power grid.

(7) Principle of the *moving part*: Movement (animation) on the display should be compatible with existing mental models and population stereotypes (e.g., movement up and to the right indicate increasing values). Animation of power flows in the GDV is a good example, with direction of the transmission line animation corresponding to the direction of flow in the physical system.

iii. Principles based on attention:

(8) Principle of *minimizing information access cost* (IAC): Display efficiency can be measured by how quickly or with how little effort operators are able to glean information they need from displays. This factor is particularly critical when operators are responding to emergency situations or are otherwise under time pressure.

(9) Principle of *proximity compatibility*: Information from several sources must often be mentally integrated for proper decisions; to facilitate such mental integration, the information sources should be in close physical proximity on the display, or linked together in some other fashion (e.g., color coding, arranging them into a pattern, etc.). Good proximity compatibility will help minimize IAC (P8).

(10) Principle of *multiple resources*: As was mentioned before, at times amounts of visual information presented on displays will exceed human capabilities to attend it all in a given (limited) time; hence, off loading the visual perceptual channel by presenting some of the information via auditory channels should be considered.

iv. Memory principles:

(11) Principle of *knowledge in the world*: Due to the limitations of human working memory and the human propensity for errors in retrieval of information from the long-term memory, all information they need for their tasks should be readily available in the display.

(11) Principle of *predictive aiding*: Predicting future, or extrapolating system states into the future is a cognitively demanding task depending heavily on working memory and therefore susceptible to errors. Computers, however, can easily process complex algorithms and display resulting predictions, changing the resource-demanding cognitive task into a simple perceptual one for the human operator.

(13) Principle of *consistency*: Finally, humans are creatures of habit and deviations from learned procedures or visual display elements invite errors of habit. Therefore, it is important that display design is consistent across different displays or display modes (cf. P8) as well as conforms to old display conventions (cf. P3).

The above principles can easily be extended into situations where the operators are required to monitor and work with multiple displays. These display layout principles can be summarized as follows:

- Frequency of use principle: Minimize information access cost (P8) by placing most frequently used displays in the operators' primary visual area (PVA).
- Display relatedness or sequence of use principle: This is closely related to the proximity compatibility principle (P9) above; related displays or displays that are viewed in a given sequence should be placed in close proximity and grouped in a manner that allows their systematic reading according to the task demands.
- Organizational grouping principle: This principle is closely related to the previous one and should be followed to help minimize IAC (P8)
- Stimulus-Response (S-R) compatibility principle: Display should be close to its associated control; in modern applications displayed information and associated controls are easy to integrate, with controls operated directly on the display by a mouse or some other pointing device.
- Clutter avoidance principle: Clutter reduces the legibility of displays and increases IAC and should therefore be avoided.

6.2.2 Design principles for the use of color in visual displays

Further principles for the use of color in displays are found in [8] and detailed specifications in [9]. Although these guidelines and specifications have been developed for the particular application domain of air traffic control, they are readily generalizable to other domains, too, and in fact can be directly applied in electric transmission control room displays.

(1) Displays must be designed for specific tasks they need to support and the environment in which they will be used, including color-coding scheme. Color displays also need to be designed for the lighting environments in which they will be used.

(2) Whenever color is used to code critical information, there must be some other signal to the meaning other than color.

(3) Limit the number of colors that need to be identified to six. More colors results in confusion and make it difficult to remember the entire color-coding scheme. This does not preclude the use of more than six colors on a display, however, but the use of additional colors should be limited to tasks that depend on being able to tell the difference between two or more colors that are always present, rather than tasks that depend upon identifying any single color (cf. P2)

(4) Adequate chromatic and luminance contrast that particular colors (foreground and background) will yield for legibility is 8:1 for items that need to be read; for details that do not need to be read, a contrast ratio of 3:1 (sometimes less) is acceptable. These guidelines were originally developed in [10].

(5) Obey color conventions: Red for danger, alert, or warning, green should indicate an 'OK' status; yellow is typically used to convey caution.

(6) Do not use pure blue for fine detail of background: when short wavelengths are in focus, all other wavelengths are slightly out of focus and vice versa; small blue symbols or text can appear fuzzy.

(7) Use bright and saturated colors sparingly to preserve the conspicuity of high luminance and to avoid 'visual noise'.

(8) Use of color must be consistent across all of the displays that a single operator will use; meanings assigned to individual colors need to be compatible across displays (cf. P3 and P13 above).

(9) Color set should be selected for each type of display (e.g., CRT, LCD, plasma, or projection) and for the ambient environment. For dimly lit environments, a dark background is preferred, but an absolute black background should be avoided because of the glare that it invites.

(10) Any implementation of color must be tested in the environment in which it is intended to be used.

6.2.3 Ecological interface design principles.

Ecological interface design (EID) is theoretical framework for interface design and an attempt to extend the benefits of traditional direct-manipulation interfaces (DMI) to complex human-machine systems [11]. EID is based in two fundamental concepts: (1) the Abstraction Hierarchy (AH), and (2) the Skills-, Rules-, and Knowledge (SRK) framework [12]. The abstraction hierarchy describes the level of understanding the operators may have of systems under their control, ranging from the functional purpose of the system (e.g., production flow models, system objectives) at the highest level to the physical appearance and anatomy of system components (the 'nuts & bolts') at the lowest. The SRK framework describes human behavior on three levels: Skill-based behavior (SBB) consists of sensory-motor performance during acts that (after a

statement of intention) take place without conscious control as smooth, automated, and highly integrated patterns of behavior. It is used for diagnostic troubleshooting by a direct match between the features of the problem observed and patterns previously experienced and stored in the long-term memory (LTM), and it is fast, requires little cognitive activity, accurate. The rule-based behavior (RBB) is controlled by a stored rule; performance is goal-oriented, but the goal may not be explicitly formulated but is found implicitly in the situation that released the stored rules. Diagnosis is done by applying sets of rules stored in LTM, e.g., sequence of steps and the procedures for doing so. The knowledge-based behavior (KBB) is explicitly goal-controlled performance in unfamiliar situations where no rules or know-how are available; functional reasoning based on mental models. It relies on iterative diagnostic testing and subsequent analyses necessary for problem-solving.

In complex human-machine systems the range of events operators must respond can be organized in three classes: (1) Familiar events for which they have necessary skills through repeated exposure (most frequently), (2) unfamiliar but anticipated events; lack of operator skill compensated by tools and aids anticipated by the designer (infrequently), and (3) unfamiliar and unanticipated events even by designers; hence, no procedures, tools, or aids are available but solutions must be improvised. In these situations cognitive control may rely on a repertoire of automated behavioral patterns (SBB), a set of cue-action mappings (RBB), or problem-solving operations on symbolic representations (KBB).

The EID guidelines for display design are also grouped by the SRK framework: In SBB, the operator should be able to act directly on the display (i.e., direct manipulation device preferred over command-language interface). In RBB the display should provide consistent one-to-one mapping between the work domain constraints and the cues or signs provided by the interface (i.e., provide the operators signs they can use to select appropriate actions), allowing operators rely on perceptual cues instead of having to resort to KBB and take advantage of the economy of RBB while preserving the wide applicability of KBB. Finally, the display design should support KBB by revealing the problem space in the form of an AH presentation, providing the operators a normative model of the work domain, supporting experimentation, and relieving the operators of the burden of keeping track of causal nets within which they are reasoning.

The specific EID design guidelines can be summarized as follows:

- (1) Support experimentation by making boundaries of acceptable performance visible and their effects observable and reversible.
- (2) Provide feedback to support understanding and KB monitoring during RB performance, make visible latent constraints upon action.
- (3) At the RB level, the display should represent cues for action as readily interpretable signs and indicate the preconditions to their validity (i.e., signs should have symbolic content)
- (4) To assist operators in coping with unanticipated situations at the KB level, provide tools for experimentation and hypothesis-testing without a need to impact the plant, or make these actions reversible
- (5) Provide users with overview displays by which SB routines can be peripherally monitored
- (6) At RB level, avoid procedural traps (strong-but-wrong rules) by providing integrated patterns as cues for action

- (7) At the KB level, support memory by externalized schematics of mental models
- (8) Present information based on available data that is simultaneously suitable for SB, RB, and KB processing
- (9) Provide an externalized mental model to aid in causal reasoning
- (10) Provide external memory aids for items, acts, and data that are not part of the present operational ‘gestalt.’

All of the above principles were used in the evaluation of the current version of LODF and in developing the prototype display.

6.3 Evaluation of Line Overload Correction Form (LOCF)

Formal evaluation of the one-line diagram used with the LOCF followed a modified human factors checklist from [13]. In addition, we performed a hierarchical task analysis (HTA) on the LOCF itself, and interviewed TVA operators on March 7-9, 2007.

6.3.1 Task analysis

Task analysis is defined as “A process for determining in detail the specific behaviors required of the personnel involved in a human-machine system” [14], or, in other words, a way of systematically describing a system to better understand how to match the demands of the system with human capabilities. Task analysis is hence a critical element of any human-machine system design, for it allows for representation of the operators’ needs for completing their tasks safely and efficiently, which consequently provides system designers guidelines for meeting these needs. Task analysis does not refer to any particular method, but rather to a collection of techniques for describing how people interact with systems.

The specific task analysis technique chosen for this project was hierarchical task analysis (HTA). This technique produces a hierarchy of operations, different subtasks people need to do within a system, and plans, which describe the conditions necessary to undertake the operations [15]. The HTA performed on the line overload solver tool is depicted in Table 6.. The procedure and results of the HTA are detailed in the following paragraphs as well.

The purpose of the one-line diagram environment studied (see Figure 2.15 for an example) is to easily recognize, diagnose, and solve line overloads on a power line grid. There are no alternate functions associated, other than simply monitor the grid run smoothly, rather than search for line overloads. Line overloads trigger specific alerts in any case, greatly simplifying the monitoring task.

As the operator monitors the system on the one-line, locating any line overloads should such arise is quite simple due to the very salient visual alerts. In further identifying these overloads, it is essential that the operator find the overload with the largest value (will be given in a percent.) (Should the operator accidentally mislabel an overload as the largest, the process will still function without a problem. The reasoning behind starting with the largest one is that upon compensating the generators’ outputs for that specific overload, it could in turn fix some of the smaller overloads as well.) Assuming the operator has found the largest overload, he is to then open the *Correct Line Overload* dialog box by right-clicking on the error icon, then left-clicking on *Correct Line Overloads*.

The next step is to pick the two best generators for fixing this line overload – one will have its output increased, the other will have its output decreased. This task has essentially been done

through the use of complex mathematical formulas. The final column in each category ranks the generators' effectiveness based on a combination of their availability of power to be increased or decreased (pending which category is being inspected) and their sensitivity (how much the increase or decrease in power output will affect the generator's performance – note: higher sensitivity is better). Once the best generator in each category has been determined, the operator is to left-click on each of them.

The final step is to adjust the power output of the selected generators. After the generators have been selected, left-click “Select MW amount” towards the top right corner of the dialog box. Now comes the most important aspect of the task. The operator must inspect two values in the subsequent dialog box (that appears upon clicking on Select MW amount.) And those two values are labeled *Max Generation Change* and *Generation Change to Fully Correct*. Simply put, the *Max Generation Change* is the maximum combined amount of power that can be altered from the selected generators. The *Generation Change to Fully Correct* is the minimum amount of power required to solve the overload. After comparing those two values, if the *Max Generation Change* value is larger than the *Generation Change to Fully Correct*, click OK, then click on *Make Requested Generation Changes and Solve Power Flow*. Then close the *Correct Line Overload* dialog box and look at the system. If the *Max Generation Change* is smaller than the *Generation Change to Fully Correct*, still click OK, but this means the power output of additional generators must be altered before this specific line overload is solved. To do this, return to the previous steps of how to select the best generators, then continue on. If the next pair of generators does still not provide enough power to fix the overload, choose another pair. When there is finally enough of a total change in power output for the *Max Generation Change* to be larger than the *Generation Change to Fully Correct*, simply follow those steps provided above.

Following these procedural steps should solve the specified line overload. If there are other overloads as well, simply begin the process again. Although, as mentioned previously, solving one specific line overload may consequently solve additional overloads in the process, so do not be confused if the total amount of overloads decreased by more than one.

The necessary time required to fix a specific line overload is (not necessarily linearly) proportional. If the overload is larger, it would require to be fixed quicker than a smaller overload. The exact ‘time limit’ is not known, but as in most cases, it is best not to wait and potentially let things worsen. That being said, it is also best not to rush since the task does not need to be completed within a matter of seconds.

Table 6.2: Task Analysis

Superordinate	Task Analysis Plans/Operations	Notes
0	<p>SOLVE LINE OVERLOAD(S)</p> <p><i>Plan 0:</i></p> <p><i>Do: 1-6; if multiple errors, repeat beginning at 3</i></p> <ol style="list-style-type: none"> 1. Open simulator environment 2. Watch system 3. Locate error(s) 4. Open “Correct Line Overloads” dialog box 5. Select best 2 generators 6. Adjust generators’ output to eliminate overload 	<p>Can be multiple</p> <p>No time limit</p> <p>Can be multiple</p>
3	<p>LOCATE ERROR(S)</p> <p><i>Plan 3:</i></p> <p><i>Do: 1, 2; 2 MUST be done before proceeding</i></p> <ol style="list-style-type: none"> 1. Find all errors 2. Find error with largest overload 	<p>Value will be given in %</p>
4	<p>OPEN “CORRECT LINE OVERLOADS” DIALOG BOX</p> <p><i>Plan 4: Do: 1, 2</i></p> <ol style="list-style-type: none"> 1. “Right-click” on largest error 2. “Left-click” on correct line overloads 	<p>Drop-down menu choice</p> <p>All subsequent indicated Clicks will be left clicks</p>
5	<p>SELECT BEST 2 GENERATORS</p> <p><i>Plan 5: Do: 1, 2</i></p> <ol style="list-style-type: none"> 1. Identify best generator in each category by (decreasing) rank in last column 2. Physically click on the top generator in each category 	
6	<p>ADJUST GENERATORS’ OUTPUT TO ELIMINATE OVERLOAD</p> <p><i>Plan 6:</i></p> <p><i>Do: 1, 2, compare values to determine which is greater, 3, if “Max Generation Change” is greater than “Generation Change to Fully Correct” then do 4, 5. If Max Generation Change is less than Generation Change to Fully Correct, then stop and begin at plan 5</i></p> <ol style="list-style-type: none"> 1. Click “Select MW amount” 2. Inspect Max Generation Change value against Generation Change to Fully Correct value 3. Click “OK” 4. Click “Make Requested Generation Changes and Solve Power Flow” 5. Close Correct Line Overload dialog box 	

6.3.2. Display evaluation

To evaluate the display in more detail, we used a human factors checklist, which was modified from [13]. This checklist represents an exhaustive review of human factors guidelines and standards pertinent to air traffic control (ATC) systems. As the ATC task environment has much in common with generic control room task environments and human supervisory control settings, the checklist was easy to modify for development and evaluation of electric power transmission control room displays. In the display development phase, design decisions should be made in a manner that each item in the list can be answered in the affirmative (= true). System evaluation or usability testing must be performed to validate the design in its intended task environment and by its intended users; any items answered in the negative (= false) warrant redesign. The display was in compliance with the majority of the items in the checklist (over 225 individual items); recommendations for improvement follow.

II.A.3. Essential operational information is never blocked or obstructed by other information.

True ☐ False ☒ N/A ☐

Comments: When opening the “correct line overload” dialog box, it can cover the map of displayed overloads. While the box can be moved and shrunk as need be, perhaps it can be designed so the map is still viewable concurrently.

II.A.4. All information that an operator needs to accomplish a task that is essential and time-critical is located on a single page or in a single window.

True ☐ False ☒ N/A ☐

Comments: See prior comment.

II.A.6. Display clutter is not a problem.

True ☐ False ☒ N/A ☐

Comments: The line overload icons, as well as the icons indicating which lines are disabled can be too large. While they are adjustable, it is still difficult because they can cover the part of the map beneath them. Perhaps they could be designed to be translucent.

II.A.12. The operator will not need to identify more than five colors (i.e., to interpret the meaning of the color when it stands alone).

True ☐ False ☒ N/A ☐

Comments: There are more than 5 colors displayed, but it is within reason I believe. Green arrows, Red error circles, White line failure circles, Gray state borders, Yellow Pink Blue and Orange power lines indicating power of the line.

II.A.15. Saturated (i.e., vivid) red and blue are never presented next to each other.

True ☐ False ☒ N/A ☐

Comments: In the overload correction graphical display, red and blue “triangles” can be displayed within close proximity of each other.

II.A.16. Colors are far enough apart in perceptual terms that they are not confusable even when "washed out" by sunlight, if applicable.

True ☐ False ☒ N/A ☐

Comments: *In the overload correction graphical display, when there is less sensitivity in the generator, the color is displayed as more washed out. It can be difficult to distinguish between the highly washed out reds and blues.*

II.A.19. To acquire needed information, the operator only needs to look at a single, localized display i.e., switching back and forth between two or more displays is not necessary to perform an individual task.

True ☐ False ☒ N/A ☐

Comments: *If the operator is in the line correction overload dialog box and wishes to see the "error map" displayed, he needs to move the dialog box so the other screen is displayed.*

II.A.31. Acronyms in the new display system have the same meanings as in the previous system.

True ☐ False ☐ N/A ☒

Comments: *I am not familiar with the old display system. I would assume they do, as that is where the acronyms come from, but since I am not sure, I will indicate N/A.*

II.A.32. Terms in the new display system have the same meanings as in the previous system.

True ☐ False ☐ N/A ☒

Comments: *See #31.*

II.A.33. Symbols in the new display system have the same meanings as in the previous system.

True ☐ False ☐ N/A ☒

Comments: *See #31.*

II.A.36 If size coding is used, it is limited to two widely different sizes.

True ☐ False ☐ N/A ☒

Comments: *I do not believe size coding is used.*

II.A.48 The heights and widths of characters appearing at the center and the four corners of the displays do not vary by more than 10 percent.

True ☐ False ☒ N/A ☐

Comments: *Pending how large or small the error icons are changed to (on the map), they text within them can be larger or smaller than other text on the screen.*

II.A.51. All colors are 8 times brighter than the static background symbology.

True ☐ False ☒ N/A ☐

Comments: *Some of the lines (gray state lines, possibly blue power lines) can be difficult to discern.*

II.B.2. High-priority alerts and other critical information are located within the central display area (i.e., the central 15 degrees of the area where the operator normally looks, given the normal viewing position).

True ☒ False ☐ N/A ☐

Comments: *They can appear anywhere on the grid, but the red error against the background color should be enough to distinguish it immediately.*

II.B.6. The color red is used only for warning/danger.

True ☐ False ☒ N/A ☐

Comments: *Red is used in the graphical display of the correct line overloads map to indicate the generator's ability to be increased.*

II.B.11. For a time-critical warning system (such as a conflict detection or resolution advisory), the operator response time that is assumed by the algorithm has been measured.

True ☐ False ☐ N/A ☒

Comments: *Time is critical, but since it is not required within seconds there is no algorithm measured.*

IV.A.2. The design assists the operator in detecting errors in data entry.

True ☐ False ☒ N/A ☐

Comments: *More could be done in the correct line overload tabular display. For instance, if 2 generators are selected that do not meet the requirements to solve the selected overload, I feel it should be displayed. And similarly if they do meet the requirements.*

IV.A.3. The design assists the operator in correcting errors in data entry.

True ☐ False ☒ N/A ☐

Comments: *See #2.*

IV.A.5. This design helps the operator to integrate information from multiple sources, if the information is not already integrated before it is presented to the operator.

True ☐ False ☒ N/A ☐

Comments: *In the tabular and graphical view of the correct line overload dialog box, it is required to remember the map and the location of the subsequent errors.*

IV.A.34. When timesharing is necessary, the tasks to be timeshared are spread across the operator's resources, that is, visual, auditory, and manual capacities, instead of loading up on just one or two capacities.

True ☐ False ☒ N/A ☐

Comments: *No auditory capacity required (ie: no auditory alerts – perhaps there could be?). So the burden seems to be solely upon visual capacities.*

IV.A.36. Procedural task sequences are interruptable at any point.

True ☐ False ☒ N/A ☐

Comments: *The process of correcting a line overload can be cancelled at any point up until the submission of the correction.*

IV.B.4. Automated features provide explanation of their intentions, recommendations, and actions in ways that are readily understood by operators

True ☐ False ☐ N/A ☒

Comments: *The help file in the simulator does not appear to be working, but everything that is required to explain the automation should be in there.*

IV.B.5. With this design, reversion to manual control will be easy; that is, the operator will have no problem stepping in when the computer cannot deal with a situation or when the automation fails

True ☒ False ☐ N/A ☐

Comments: *Only if the operator is experienced enough to have an understanding of where each generator is located, and it's associated power output and sensitivity.*

V.D.1. Error messages are provided whenever needed

True ☐ False ☒ N/A ☐

Comments: *See IV:A, #2.*

VI.F.4. The mouse is equally usable with the left or right hand

True ☒ False ☐ N/A ☐

Comments: *Lefties just need to use their middle finger for the "left-click" and index finger for the "right-click" functions of the mouse. Or they may use the mouse with their right hand. Or some special mouse may be designed (if it does not already exist) where it is a mirror of the right-handed mouse.*

Recommendations:

1. Upon selecting 'correct line overload', perhaps the dialog box could be displayed side-by-side with the display map. In other words, each window would occupy one-half of the total screen and that ratio could be adjusted as needed simply by expanding or minimizing each window as is normally done.
2. In the 'correct line overload' dialog box (either tabular or graphical), there could be an indication of whether or not the selected generators will suffice in correcting the selected overload. Perhaps a green checkmark for a sufficient selection or a red X for an insufficient selection would be simple enough. This would be especially useful if multiple combinations of generators are required to fix a specific overload.
3. If the algorithm of the system could be redesigned to include the location of each generator as a parameter for finding the best possible combination of generators, it could become more efficient. This could in turn help solve multiple line overloads in fewer steps.
4. On the overview map, I feel it would be more beneficial if the error containing the largest overload was more easily distinguishable from the rest of the errors. Maybe it could default to being slightly larger, or a slightly different shade of red.
5. When trying to zoom in on the overview map, the error icons do not get seem to move. They remain the same size while lying over top of the map, making it virtually

impossible to see beneath them. Icons should enlarge or shrink with the relative zoom of the map.

6. In using the ‘correct line overload’ dialog box (both tabular and graphical), the selections do not reset after completing the selections. For example: In the tabular display, if one chooses the 2nd generator from the top in both columns and make the changes, then go to select another pair of generators, the cursor remains highlighting the 2nd generators in both columns. The same principle is applied in the graphical display (the previously used generators remain highlighted). The cursors should return to the top of the columns regardless of the prior selection in the tabular display, and they should reset completely in the graphical display (in other words – nothing should be highlighted any more.) Figure 6.2 illustrates overlapping line overload indications masking the line information behind them.

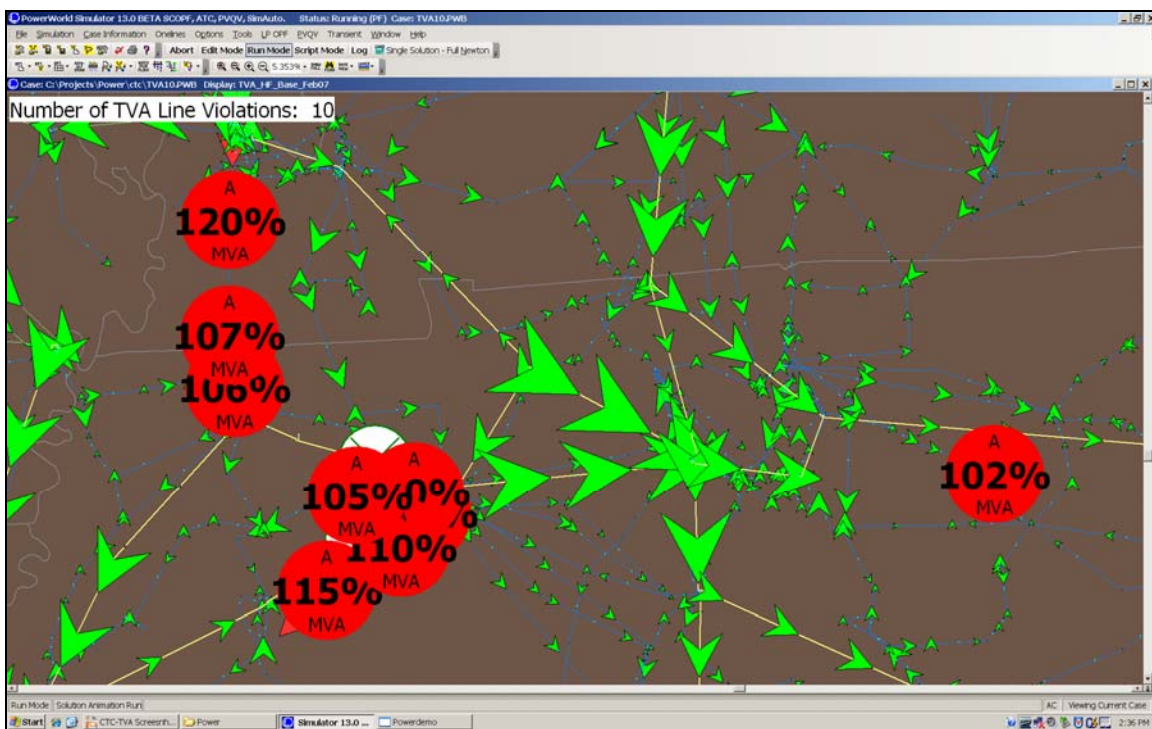


Figure 6.2: Line overload indications

6.4 Design of the prototype display.

New display solutions were developed from ‘scratch’ according to the general display design guidelines as described above. There were two primary goals for the prototype display: (1) Reduction of ‘visual noise’ by avoidance of bright and saturated colors (reserved for alerts) and making animation less conspicuous, and (2) reduction of clutter by design of symbol and icon sizes and re-scaling display elements during zoom (i.e., the zoom function doubled as a declutter function).

6.4.1 Specifications for a Prototype Wide-Area Power Transmission Display

(1) Units: The main units to be displayed are real power (MW) and reactive power (MVAR); both should be displayed on alternate displays, with a pull-down menu where the operator may choose the units to be displayed.

The background map color was specified to be light tan; all colors were defined on the Hue, Saturation, Brightness scale. Hence, the background color was defined as H: 50°, S: 50%, B: 90%. The neutral background color allowed for adequate contrast with other display elements.

A generator that is disconnected shall be represented by a solid black circle; a generator connected shall be represented by an open circle. Generator output was displayed as concentric circles of varying size and color under the generator-substation symbols. The size of the colored circle was scaled to the size of the max output circle around the generator (see Fig.) and scaled by area to the percent output of the generator. The maximum output of a generator was depicted as a dashed circle around the generator symbol; the size of the circle corresponded to the maximum output of the generator. Hence the circles around different generators adhere to a common scale.

Substation symbols were solid white (connected) or black (disconnected to the grid) squares. Load power requirement units were MW (for real power consumed) and MVAR (for reactive power consumed). Load power requirement were displayed as concentric circles of varying size and color under the substation symbol. The size of the colored circle started from twice the diameter of the substation symbol and increased at equal increments for each increment in load power requirement. At each increment the previous circle also changed color, creating a contour effect of a 'valley' centered at the substation. The main idea behind representation of generator output and load requirement as defined is to create an image of topography on the map, generators mimicking high ground and load consumed low ground (flow is then from 'high' to 'low' areas on the map).

The transmission lines displayed had the following nominal kV ratings: 500 kV, 230 kV, 161 kV, 138 kV, and 115 kV. These lines were differentiated by the line width. Transmission lines that were closed (energized) appeared white; lines that were open (de-energized) appeared black.

Line flow was represented by bright, animated (moving) segments on the line. The variables represented will be direction of the flow by direction of the movement of the segments, and percent loading, represented by the spacing of the segments. Even spacing of the segments represented 50% loading; as the loading increases, the proportion of the bright segments to the underlying line increased correspondingly so that when the line loading reached 100%, the entire line is highlighted in bright. When the line loading exceeded 100% the line alternated between bright and regular line colors to attract attention.

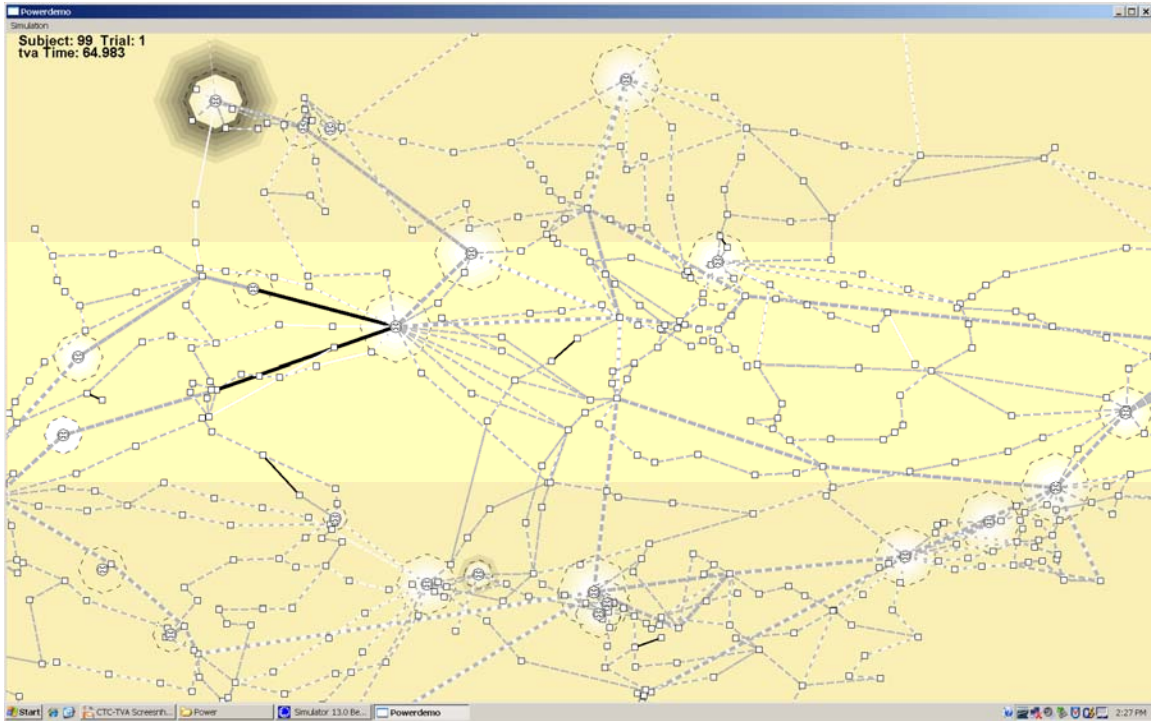


Figure 6.3: Prototype Wide Area Display

6.4.2 Future Directions

One of the greatest obstacles to decluttering the proposed wide-area displays is the geographical realism of the location of substations/generators and the transmission lines between them. A valid and indeed critical research question therefore is: How important GDV is to the operators, and how far one could deviate from veridical geographic representation of the transmission grid on wide area displays without detrimental effects on operator performance. It may very well be that the benefits of decluttering the display would outweigh any loss of geographical realism. If this were the case, the map could be redrawn by transforming the latitude and longitude coordinates of substations and drawing transmission lines as straight lines between these, regardless of their true paths over terrain, so that the following criteria are met: (1) the transmission lines should be either vertical or horizontal so that (a) intersection between lines and (b) turns in them are minimized; (2) different substation symbols and transmission lines must not overlap; (3) the relative positions between substations is preserved; and (4) the magnitude of positional change for the substations from natural geographical to the schematic coordinates per the above constraints is minimized.

This appears to be a problem that could be solved iteratively by a computer, possibly modeled as a mixed integer program and solved by a commercial solver (CPLEX). Redrawing the map in this manner would also offer opportunities for additional decluttering algorithms, and schemata for adding detail to become visible at higher zoom ratios.

7.0 Utilization and Visualization of GPS-synchronized Data for Stability Monitoring

Monitoring the operating state of the system and assessing its stability in real time has been recognized as a task of paramount importance and a tool to avert blackouts. It is also recognized that when real time data are used to derive the real time dynamic model of the system, it is possible to predict the behavior of the system and therefore will enable preventive action. This report presents work in this area. The work is focused on the utilization of the available data for extracting a real time dynamic model which in turn is used to determine the stability of the system via energy functions. The described procedures are decentralized, i.e. the data are utilized at each substation/generating substation of the system and they are globally valid. It is shown that if GPS-synchronized data are available at each substation this is possible. We describe the technology of GPS-synchronized measurements first. The utilization of this data for extracting the real time dynamic model is described next. It is important to note that phasor data do not provide the rotor position of the generators directly. We have developed a dynamic estimation method that extracts the rotor position of all generators. In addition the estimated model is used to evaluate the total energy of the system and to extract and predict system stability.

An important issue is the accuracy of the available data. Specifically, GPS-synchronized equipment (PMUs) is in general higher precision equipment as compared to typical SCADA systems. Conceptually, PMUs provide measurements that are time tagged with precision better than 1 microsecond and magnitude accuracy that is better than 0.1%. This potential performance is not achieved in an actual field installation because of two reasons: (a) different vendors use different design approaches that result in variable performance among vendors, for example use of multiplexing among channels or variable time latencies among manufacturers result in timing errors much greater than one microsecond, and (b) GPS-synchronized equipment receives inputs from instrument transformers, control cables, attenuators, etc. which introduce magnitude and phase errors that are much greater than the precision of PMUs. For example, many utilities may use CCVTs for instrument transformers. We refer to the errors introduced by instrument transformers, control cables, attenuators, etc. as the instrumentation channel error. The end result is that “raw” phasor data from different vendors cannot be used as highly accurate data.

GPS-synchronized data offer the possibility of dramatically improved applications, such as real time monitoring of the system, improved state estimation, direct state measurement, precise disturbance monitoring, transient instability prediction, wide area protection and control, voltage instability prediction and many others. For proper functioning of each one of these applications, a certain precision of the data is required. The table below illustrates the data precision required for different applications in a qualitative way.

Table 7.1: Applications and Required Accuracy

Application	Required Accuracy
Steady State Monitoring	Low
Disturbance Monitoring	Moderate
State Measurement	High
State Estimation	High
Wide Area Protection	Moderate
Transient Instability Monitoring	High

Conceptually, the overall precision issue can be resolved with sophisticated calibration methods. This approach is quite expensive and faces difficult technical problems. Specifically, it is extremely difficult to calibrate instrument transformers and the overall instrumentation channel in the field. Laboratory calibration of instrument transformers is possible but a very expensive proposition if all instrument transformers need to be calibrated. In the early 90's the authors directed a research project in which we developed calibration procedures for selected NYPA's high voltage instrument transformers [9]. From the practical point of view, this approach is an economic impossibility. An alternative approach is to utilize appropriate filtering techniques for the purpose of correcting the magnitude and phase errors, assuming that the characteristics of the various GPS-synchronized equipment are known and the instrumentation feeding this equipment is also known.

We propose a viable and practical approach to correct for errors from instrumentation, system imbalances and data acquisition systems. It is important also to note that this process is integrated with the process of estimating the real time dynamic model of the system. The overall approach is based on an estimation process at the substation level for correcting these errors. Specifically, we propose a methodology that performs as a "super-calibrator". This computational procedure may reside at the substation, and it can operate on the streaming data. The method can be implemented using standard communication protocols, such as the IEC 61850. The process is fast and therefore it can be applied on real time data on a continuous basis introducing only minor time latencies. The proposed methodology is based on a statistical estimation methodology that requires (a) the characteristics of GPS-synchronized equipment (PMUs), (b) a detailed model of the substation including the model of the instrumentation, and (c) the detailed model of generating units. Subsequent paragraphs present the models of the GPS-synchronized equipment as well as the substation and generating unit(s) model with the instrumentation channels.

7.1 Method Description

The methodology is based on a detailed, integrated model of the power system, instrumentation channel and data acquisition system. The power system model is a detailed three-phase, breaker oriented model and includes the substation, the generating units and the interconnected transmission lines. The instrumentation channel model includes instrument transformers, control cables, attenuators, burdens, and A/D converters. The modeling approach is physically based, i.e. each model is represented with the exact construction geometry and the

electrical parameters are extracted with appropriate computational procedures. As the data stream, each set of data at a specific time tag is processed via a general state estimation process that “fits” the data to the integrated model. The procedure provides the best estimate of the data as well as performance metrics of the estimation process. The most important metric is the expected value of the error of the estimates. The best estimate of the data is used to regenerate the streaming data flow (this data is now filtered). The overall approach is illustrated in Figure 7.1.

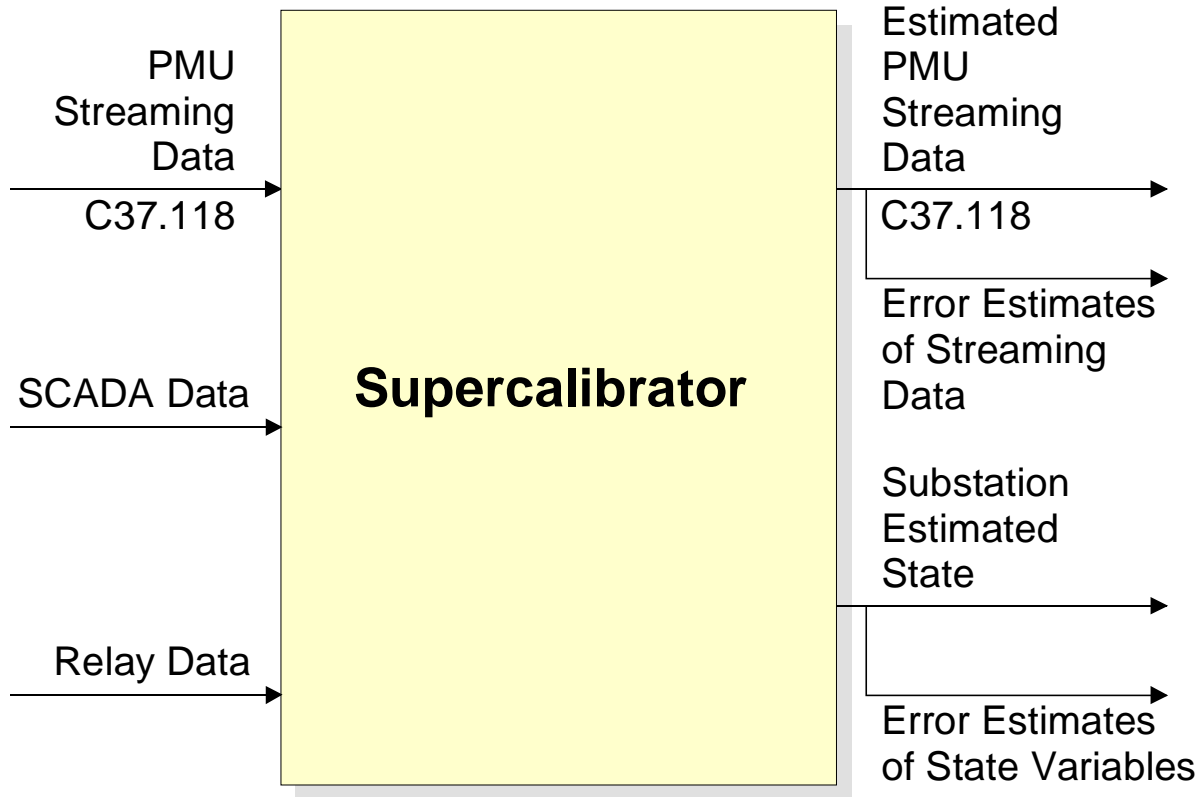


Figure 7.1: Inputs and Outputs of the Super-Calibrator as Dynamic State Estimator

7.2 Generating Substation State Estimation

The purpose of the generating substation state estimation is to extract the precise model of the generating system in real time. The model utilized in the estimation process is illustrated in the Appendix. Note that the form of the model is generically described as follows:

$$\begin{aligned} i &= f_1(x, y, z) \\ 0 &= f_2(x, y, z) \\ 0 &= \frac{dz}{dt} + f_3(x, y, z) \end{aligned}$$

where the functions f_1, f_2, f_3 are algebraic function of degree no greater than 2. The vector i are the terminal currents of the generator, x, y and z represent the state of the generator. The

measurements in this system are: terminal voltages and currents (phasors), frequency and rate of frequency change. The model equations are given in Appendix A. A conceptual view of the system and measurements is illustrated in Figure 7.2. The state of the system is defined as the minimum number of independent variables that completely define the state of the system. For the substation of Figure 7.1 the state of the system consists of: (a) the phasor voltages of phases A, B and C of the two buses (transformer high side and low side), and (b) the generator speed (frequency) and acceleration (frequency rate of change). In summary, the state of the generating substation of Figure 7.2 is defined in terms of 6 complex variables and two real variables.

The number of measurements for this system from GPS-synchronized equipment, relays and standard SCADA system is quite large. Typically, the direct voltage measurements alone will have a redundancy of two to three, i.e. two to three times the number of voltage states. The available current measurements will generate a much larger redundancy considering that there will be CTs at each breaker, transformer, reactors, etc. For the system of Figure 7.2, and with a typical instrumentation, there will be more than 120 measurement data. This represents a redundancy level of 850%.

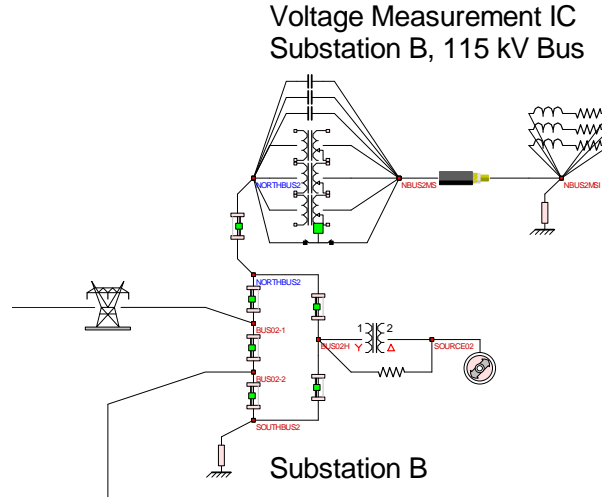


Figure 7.2: Breaker-Oriented Three-Phase Generating Substation Model

The state of the system, expressed with the variables x , y and z , is defined as the phasors of the phase voltages at each bus, the generator speed (frequency) and acceleration (rate of change of frequency) for each generating unit and a number of internal generator variables as described in Appendix A. A bus k will have three to five nodes, phases A, B and C, possibly a neutral and possibly a ground node. Under normal conditions the voltage at the neutral or ground will be very small and it will be assumed to be zero for this application. The state of the system at this bus is the node voltage phasors. We will use the following symbols:

The state vector x represents the voltage phasors:

$$\tilde{V}_{k,A} = \tilde{V}_{k,A} = V_{k,A,r} + jV_{k,A,i}$$

$$\tilde{V}_{k,B} = \tilde{V}_{k,B} = V_{k,B,r} + jV_{k,B,i}$$

$$\tilde{V}_{k,C} = \tilde{V}_{k,C} = V_{k,C,r} + jV_{k,C,i}$$

The state vector z represents the frequency (speed) and rate of frequency change (acceleration):

$$f_{gi}, \text{ and } \frac{df_{gi}}{dt}$$

The state vector y represents internal state variables needed for the quadratization of the model.

The measurements can be GPS-synchronized measurements, relay data or usual SCADA data. A typical list of measurement data is given in Table 7.1. The measurements are assumed to have an error that is statistically described with the meter accuracy.

Table 7.2: List of Measurements

Phasor Measurements Description	Non-synchronized Measurements Description
Voltage Phasor, \tilde{V}	Voltage Magnitude, V
Current Phasor, \tilde{I}	Real Power Flow, P_f
Current Inj. Phasor, \tilde{I}_{inj}	Reactive Power Flow, Q_f
Frequency	Real Power Injection, P_{inj}
Rate of frequency change	Reactive Power Inj., Q_{inj}

For monitoring the stability of the system it is imperative that the state of the generator is identified as accurately as possible. In this respect it is necessary to recognize that the instrumentation channel introduces substantial errors much higher than the errors introduced by the measuring device itself. For this reason the instrumentation channel model is included in the overall approach. Specifically, the instrumentation channel is modeled and each measurement is related to the state of the system via the transfer function of the instrumentation channel. We write:

GPS synchronized measurements:

$$z_{rj} + jz_{ij} = g_j(x, y, z), \text{ for measurement } j$$

Non-synchronized measurements:

$$z_k = g_k(x, y, z), \text{ for measurement } k$$

The model of the instrumentation channel and its gain function is obtained from the physical characteristics of the instrument transformers, control cable, termination impedances, A/D conversion devices, etc.

It is also important to recognize that it is not practical to measure the generator internal states. In this case it may appear that we do not have enough measurements to perform a state estimation. This is not true. We do have a number of equations that relate the internal generator states to other states. Each one of these equations can be viewed as a measurement with

certainty. We refer to these as pseudomeasurements which are added to the measurement set. A partial list of pseudomeasurements is provided below.

1. Pseudo-measurements of the voltages at the remote end of lines
2. Pseudo-measurements from Kirchoff's current law
3. Pseudo-measurements of individual phase voltages
4. Pseudo-measurements of neutral/ground voltage
5. Pseudo-measurements of neutral/ground currents
6. Etc.

7.3 Description of the Dynamic State Estimator

Given a set of measurements, the state of the system is computed via the well known state estimation approaches. We elected to apply a least square approach to this problem as follows. First the differential equations are integrated with the quadratic method [1]. This procedure makes the system model a set of algebraic equations in which the dynamic states assume discrete values at specific time instances. We denote the algebraic equations with the state vector $h(x)$.

Then a measurement z_i will be expressed as:

$$z_i = g_i(h_i(x))$$

The state is computed from the solution of the following optimization problem.

$$\text{Min } J = \sum_i \left(\frac{z_i - g_i(h_i(x))}{\sigma_i} \right)^2$$

where σ_i is the meter accuracy.

Note that the above simple procedure has converted a dynamic estimation problem to a static state estimation problem. Solution methods for above problem are well known. In subsequent paragraphs, the models of the measurements and the details of the hybrid state estimator are described. By manipulating the above equations, the measurements will have a general form as follows:

GPS-synchronized measurements:

$$z_s = H_s x + \eta_s$$

Non-synchronized measurements

$$z_n = H_n x + \{x^T Q_i x\} + \eta_n$$

The pseudomeasurements are in general quadratic equations, similar to above equations (in form).

Now, the state estimation problem is formulated as follows:

$$\text{Min } J = \sum_{v \in \text{phasor}} \frac{\tilde{\eta}_v^* \tilde{\eta}_v}{\sigma_v^2} + \sum_{v \in \text{non-syn}} \frac{\eta_v \eta_v}{\sigma_v^2}$$

Using the above quadratic formulation and the separation of the measurements into phasor, non-synchronized and pseudomeasurements as has been indicated earlier, the general form of the measurements is:

$$\begin{aligned} z_s &= H_s x + \eta_s, & \text{GPS-synchronized measurements} \\ z_n &= H_n x + \{x^T Q_i x\} + \eta_n, & \text{non-synchronized} \\ z_p &= 0 = H_p x + \{x^T Q_i x\} + \eta_p, & \text{pseudomeasurements} \end{aligned}$$

In above equations, the subscript s indicates phasor measurements, the subscript n indicates non-synchronized measurements and the subscript p indicates pseudomeasurements. The best state estimate is given by:

Case 1: Phasor measurements only.

$$\hat{x} = (H_s^T W H_s)^{-1} H_s^T W z_s$$

Case 2: Phasor, non-synchronized and pseudomeasurements.

$$\hat{x}^{v+1} = \hat{x}^v + (H^T W H)^{-1} H^T W \begin{bmatrix} z_s - H_s \hat{x}^v \\ z_n - H_n \hat{x}^v - \{\hat{x}^{v^T} Q_i \hat{x}^v\} \end{bmatrix}$$

where:

$$W = \begin{bmatrix} W_s & 0 \\ 0 & W_n \end{bmatrix}, \quad H = \begin{bmatrix} H_s \\ H_n + H_{qn} \end{bmatrix}$$

7.4 Implementation

The proposed methodology for correcting errors from various manufacturers is being implemented into a general state estimation method. The computer model has been named the SuperCalibrator. Presently the methodology operates on the data from one substation at a time. The overall approach is shown in Figure 7.3. Details of the SuperCalibrator approach can be found in [26].

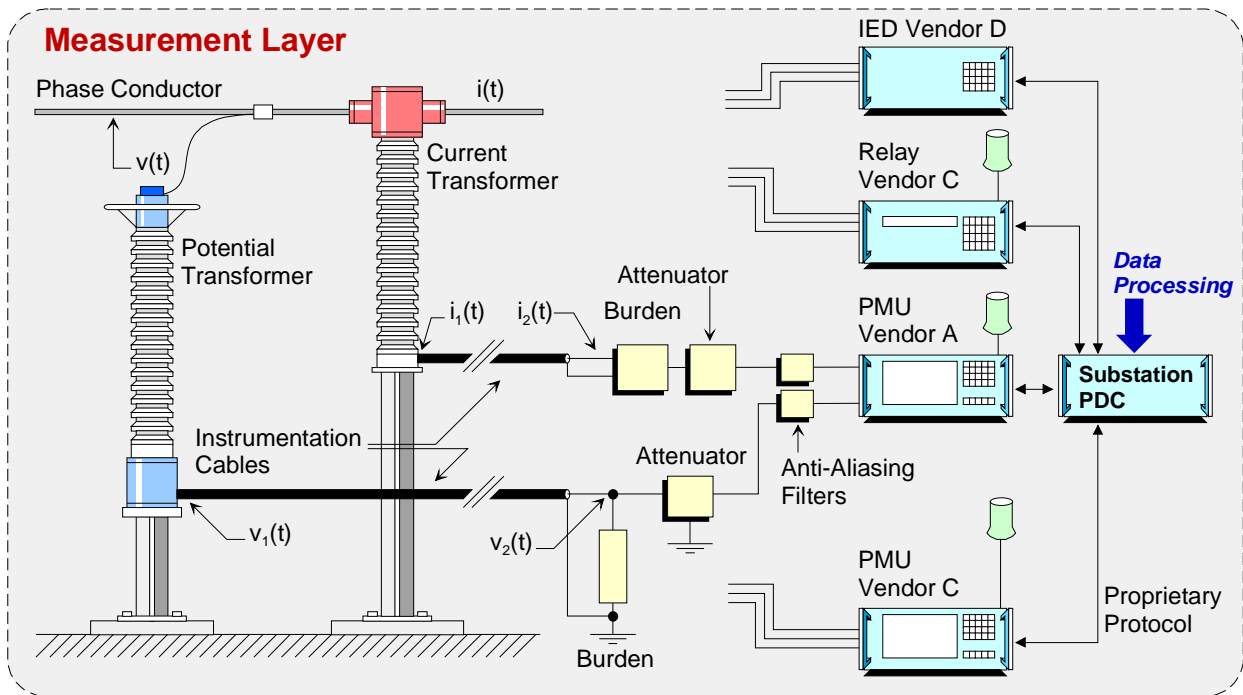


Figure 7.3: Conceptual Illustration of the SuperCalibrator

7.5 Applications

The described dynamic state estimator within the SuperCalibrator provides the basis for many applications. In this report we describe two applications: (a) stability monitoring for electric power systems and (b) a new out of step protection scheme. These applications are discussed in this section.

7.5.1 Stability Monitoring

The output of the SuperCalibrator is the state of the substation including the full operating condition of the generators in case of a generating substation. Specifically, the generator speed, torque angle and acceleration is obtained from the SuperCalibrator. This information is enough to monitor the dynamics of the generator. Use of visualization techniques can display this information in a meaningful way to system operators. As examples, Figure 7.4 illustrates a visualization of generators with respect to the center of oscillations with displaced and moving balls, while Figure 7.5 illustrates a dynamic visualization of a system with pie charts for the generators in the system and Figure 7.6 illustrates the voltages during a transient swing. Note that the visualization shows many generators as it will be the case in a typical system. The visualization shows the position of each generator according to its torque angle. In addition the speed of the generator (above or below synchronous speed) is shown with arrows that are proportional to the numerical value of the speed. Note that as the information is updated from the SuperCalibrator, the visualization provides an animation of the motion of the system. Specifically, the SuperCalibrator may “run” at a rate of 60 times per second thus updating the visualization 60 times a second. This refresh speed is more than adequate to provide an excellent animation of the dynamics of the system in real time.

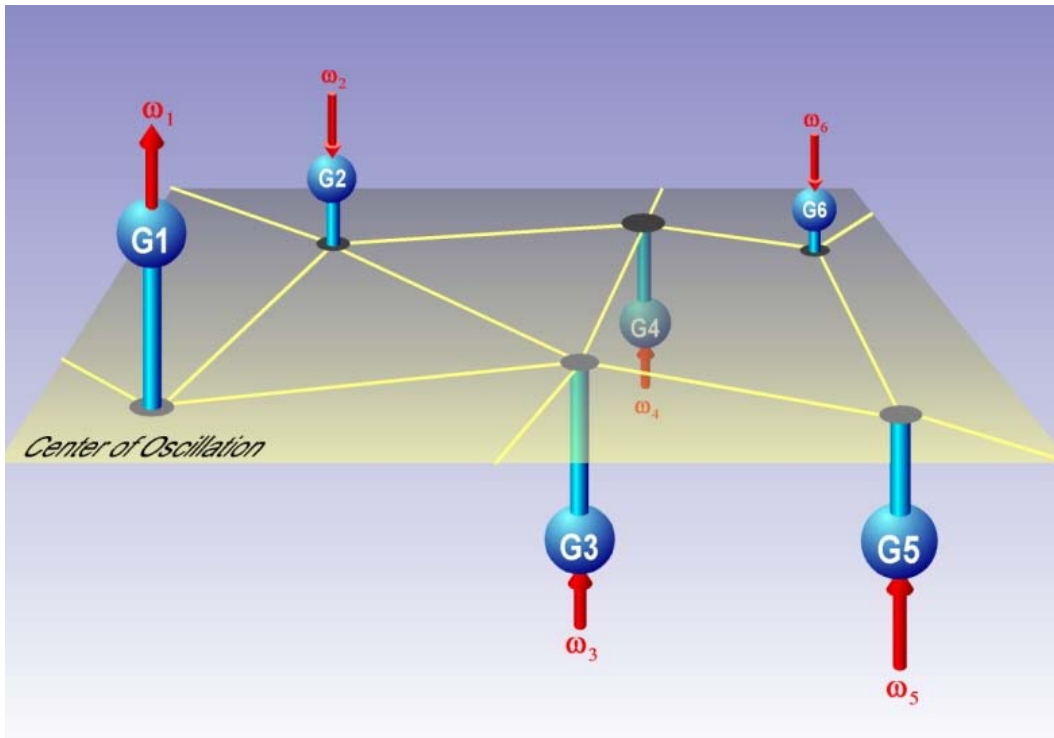


Figure 7.4: Visualization of Generator Real Time State

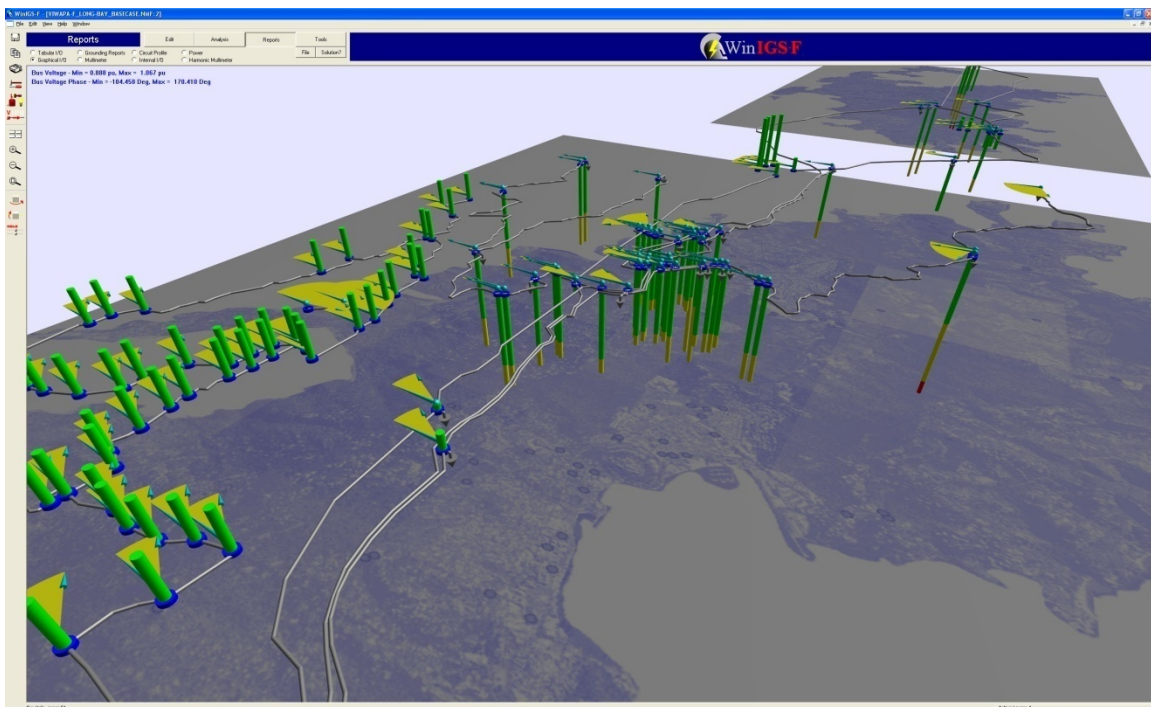


Figure 7.5: 3-D Visualization of System Phase Angles during a Transient Swing

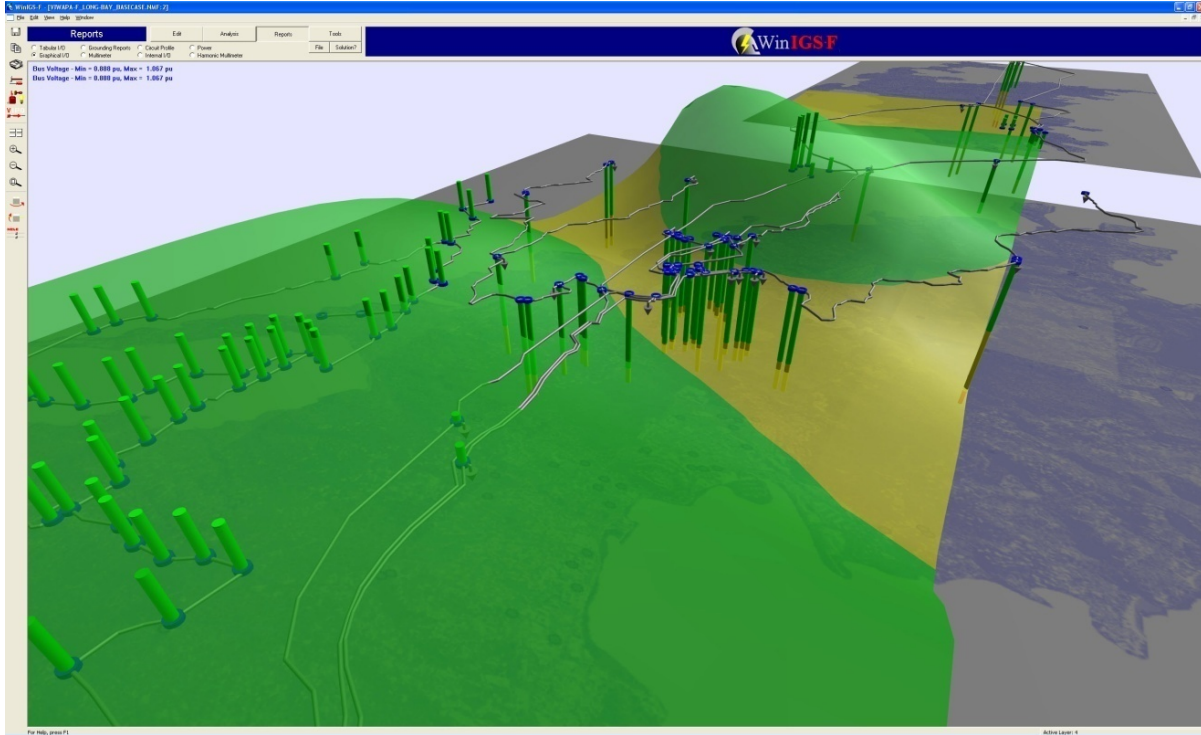


Figure 7.6: 3-D Visualization of System Voltage Magnitude During a Transient Swing

The output of the SuperCalibrator is also used for another important task. Specifically, this information is used to predict the stability of the system. For this purpose we use the output of the SuperCalibrator to compute the total energy of the system. Note that the total energy of the system is defined in terms of generator torque angle and speed. Using the quadratic formulation of this paper the energy function is also a quadratic equation of the form (defined in the usual way of the sum of the potential energy plus the kinetic energy):

$$V(x(t)) = P_1^T x_N + x_N^T(t) P_2 x_N(t)$$

Note that this form includes the state variables c and s see appendix which are transcendental equations (sines and cosines). They define the stability region in the usual way via the separatrix. The total energy can be separated into kinetic energy and potential energy. Then, having this information a number of visualizations are implemented. For example Figure 7.7 illustrates the operating condition of the generator as a blue dot superimposed on a 2-D visualization of the potential energy function. Figure 7.7 also provides a visualization and animation of the stability status of the system and in particular the generator that is involved. For example if the blue dot is above the barrier of the potential energy function, then the generator is stable and will return to a stable equilibrium once the disturbance has been removed. If above the generator is unstable and eventually will have to be disconnected from the system. This particular property naturally leads to a device for the protection of generators against out of step conditions. Because the phenomena are so fast, operator action is not a possibility. The out of step protection concept is provided next.

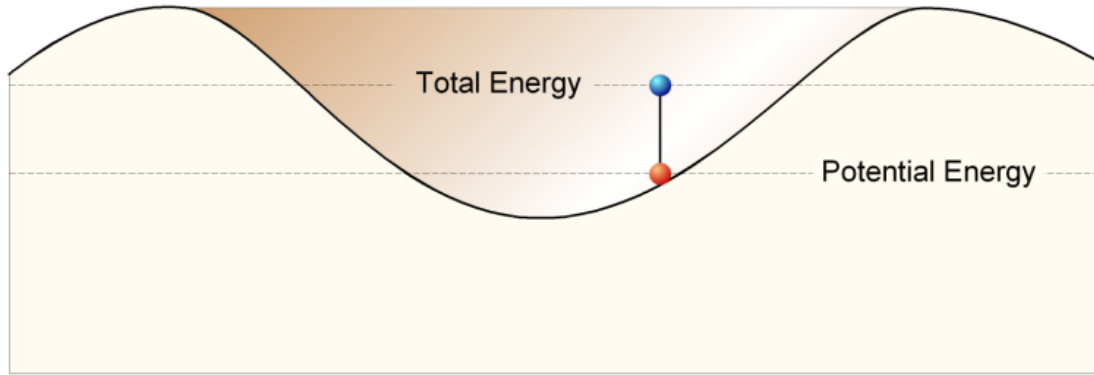


Figure 7.7: 2-D Visualization of Generator Operating Point and Potential Energy

7.5.2 Out of Step Relaying

The best estimate of the dynamic state of the system provides the necessary information for monitoring the stability of the system and as a consequence it provides an elegant method for out of step relaying. This procedure will be demonstrated with an example. The test system consists of two generating substations, two step-up transformers and a two section overhead transmission line as is illustrated in Figure 7.8. The parameters of the system are presented in Table 7.2.

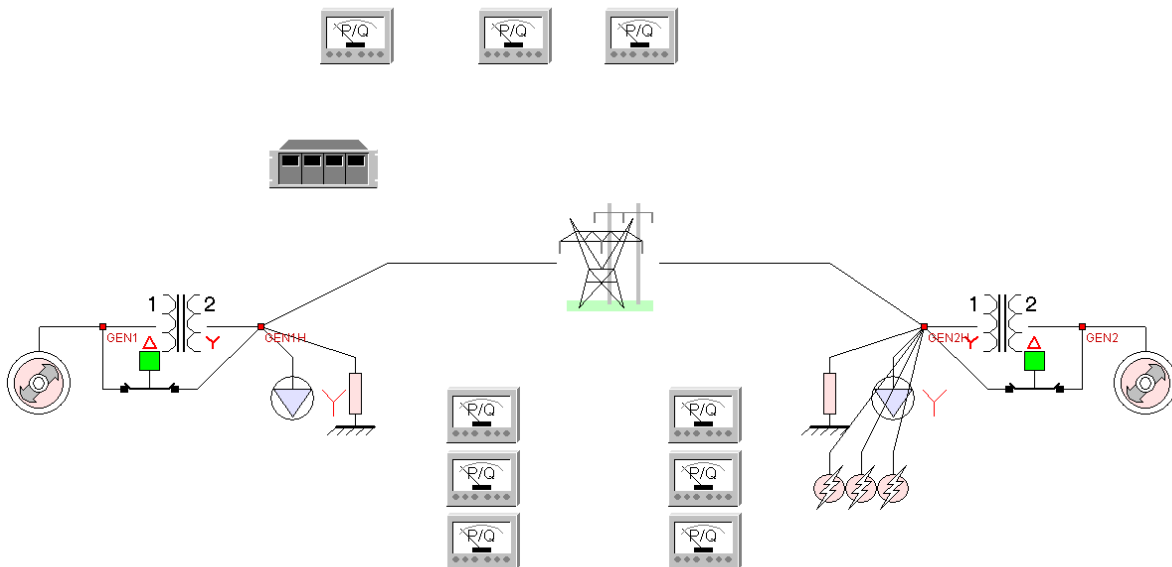


Figure 7.8: Test System Illustration

Table 7.3: Test System Parameters

Gen1	100MVA	$z= 0.001+j0.18$ pu	H=2.5 sec
Gen2	300MVA	$z= 0.001+j0.18$ pu	H= 3.0 sec
XFMR1	100MVA	$z=0.001+j0.07$ pu	15 kV/115kV
XFMR2	300MVA	$z=0.001+j0.08$ pu	115 kV/18kV
Transmission Line		$z=0.024+0.2346$ pu	115 kV
Load 1		$S=1.33+j0.1$ pu	115 kV
Load 2		$S=0.56+j0.1$ pu	115 kV
Common $S_{base}=100$ MVA			

The Lyapunov theory is used to evaluate the stability of the system after the occurrence of a fault, using information from the dynamic model of the generators. In particular, the potential energy function is computed as a function of the difference between the angles of the two generators using the best estimate of the system state. The best estimate of the real time model is used to compute the equilibrium point in the post fault conditions. Specifically, the best estimate of the real time model provides the following system model:

$$\frac{2H_1}{\omega_s} \frac{d\delta_1^2}{dt^2} = P_{m1} - P_{e1}(\delta_1 - \delta_2)$$

$$\frac{2H_2}{\omega_s} \frac{d\delta_2^2}{dt^2} = P_{m2} - P_{e2}(\delta_1 - \delta_2)$$

The generator real power equations are evaluated to be:

$$P_{e1}(\delta_1 - \delta_2) = P_{e1}(\delta) = 0.5222 - 1.75748 \cdot \cos(\delta + 100.008)$$

$$P_{e2}(\delta_1 - \delta_2) = P_{e2}(\delta) = 0.7248 - 1.7592 \cdot \cos(-\delta + 100.008)$$

Above equations are manipulated to provide:

$$M \frac{d^2\delta}{dt^2} = M \frac{\omega_s}{2H_1} (P_{m1} - P_{e1}(\delta)) - M \frac{\omega_s}{2H_2} (P_{m2} - P_{e2}(\delta))$$

where M is the two generators equivalent mass:

$$M = \frac{2H_1 \cdot H_2}{(H_1 + H_2) \cdot \omega_s}$$

Upon substitution the following swing equation is obtained.

$$M \frac{d^2\delta}{dt^2} = 0.29563 + 1.375363 \cdot \cos(\delta + 100.008) \\ - 0.0598 - 0.38242 \cdot \cos(-\delta + 100.008)$$

The equilibrium point is computed to be at:

$$\delta_s = \delta_{s1} - \delta_{s2} = 1.6142^\circ \text{ at the synchronous speed.}$$

Note that above model is provided in real time from the dynamic state estimator.

The above model permits the evaluation of the potential energy part of the Lyapunov function:

$$E_{potential} = - \int_{\delta_{s1}-\delta_{s2}}^{\delta} [M \frac{\omega_s}{2H_1} (P_{m1} - P_{e1}(\delta)) - M \frac{\omega_s}{2H_2} (P_{m2} - P_{e2}(\delta))] d\delta$$

which for the specific system is given by the following formula:

$$E_{potential} = -0.23583 \cdot \delta + 1.73214 \\ -1.375363 \cdot \sin(\delta + 100.008) - 0.38242 \cdot \sin(-\delta + 100.008)$$

The kinetic energy of the system is:

$$E_k = \frac{1}{2} M (\omega_1 - \omega_2)^2$$

where $\delta = \delta_1 - \delta_2$ is the difference of the generators' torque angles and ω_1, ω_2 are the generators' speeds.

Two example cases are presented for this system, one corresponding to a disturbance that results in a stable system and another that leads to an unstable system. Table 7.3 provides the rotor location and rotor speed at the time of fault clearing for the two cases.

Table 7.4: Generators' Torque Angles & Speeds at Fault Clearing time

Stable Case	Unstable Case
$\delta = \delta_1 - \delta_2 = 108.17^\circ$	$\delta = \delta_1 - \delta_2 = 155.028^\circ$
$\omega = \omega_1 - \omega_2 = 7.3953 \text{ rad/sec}$	$\omega = \omega_1 - \omega_2 = 8.8404 \text{ rad/sec}$

Specifically, a three phase fault that will be cleared at 0.5 seconds after the fault initiation results in a stable system. We shall refer to this case as “stable case”. A three phase fault that will be cleared at 0.6 seconds after fault initiation will result in an unstable system. We refer to this case as the “unstable case”. Figure 7.9 illustrates the total energy superposed on the graph of the potential energy function of the “stable case” at the time that the fault was cleared. Note that the total energy is below the highest value of the potential energy, indicating a stable system. Figure 7.10 illustrates the total energy superposed on the graph of the potential energy function of the “unstable case” at the time that the fault was cleared. Note that the total energy is above the highest value of the potential energy, indicating an unstable system.

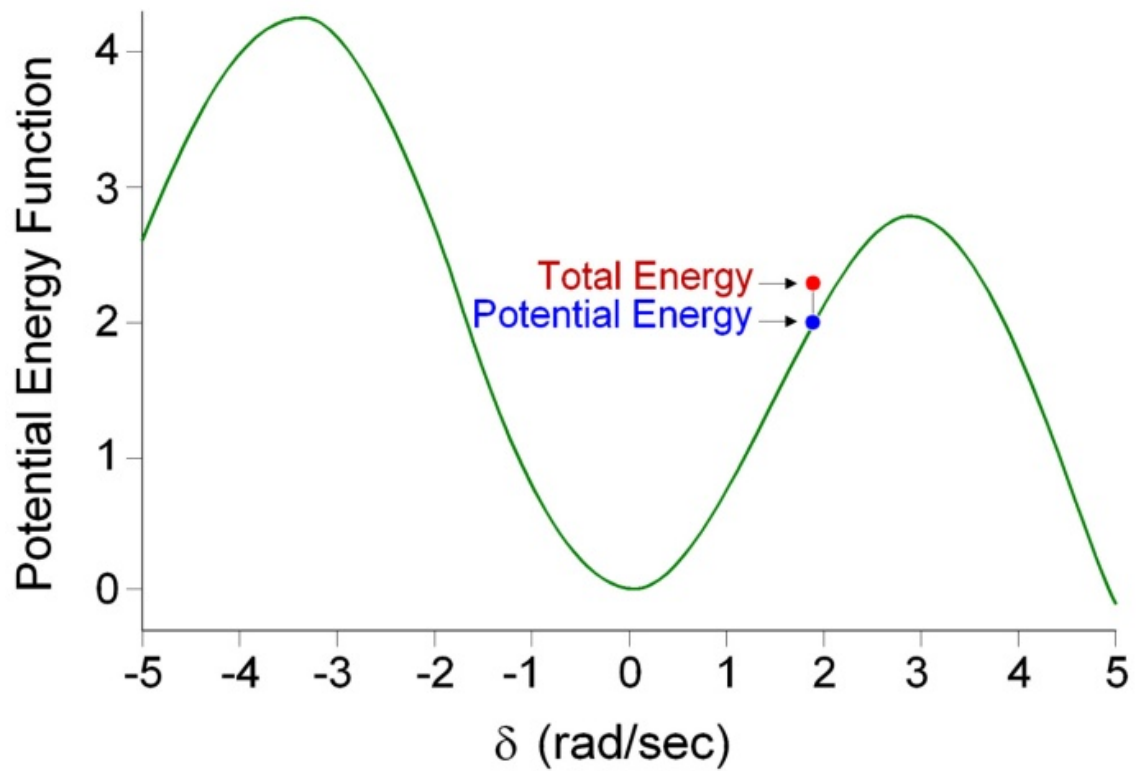


Figure 7.9: Total and potential system energy-stable case

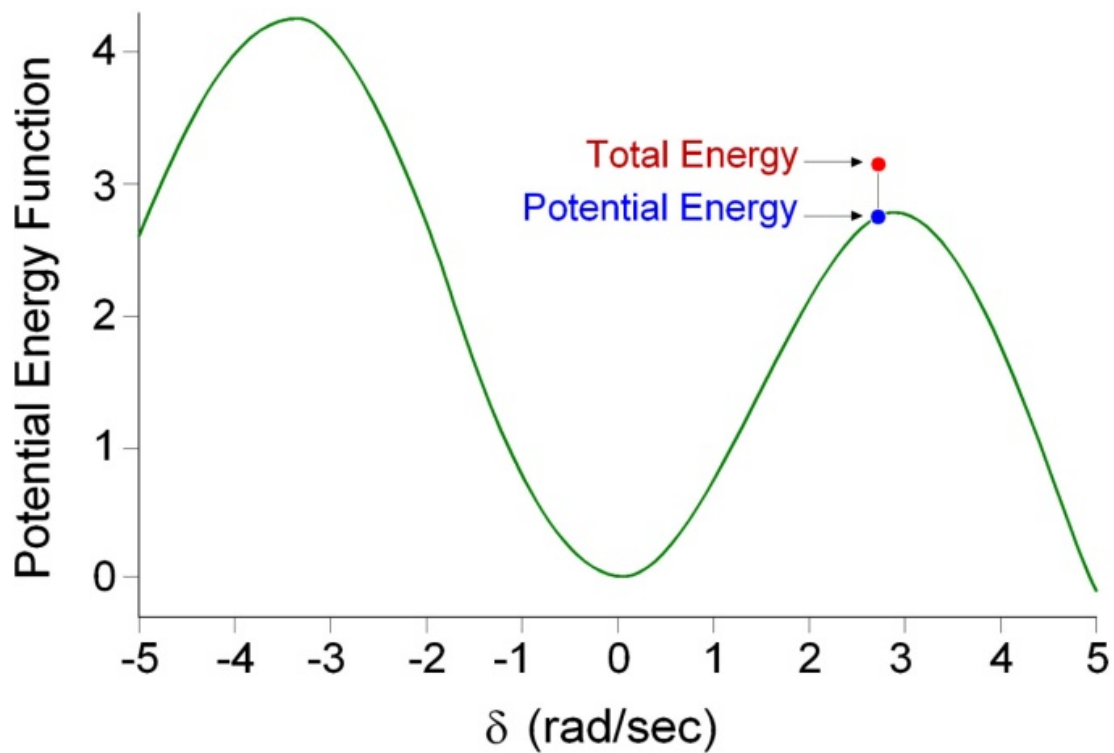


Figure 7.10: Total and potential system energy-unstable case

An important feature of the presented method is the ability to determine the time at which the system becomes unstable since it is a real time monitoring method. Figure 7.11 illustrates the trajectory of the total energy of the system as the disturbance is evolving. The instant that the total energy crosses the maximum value of the potential energy the system has become unstable. The total energy crosses the maximum value of the potential energy at 0.545 seconds after fault initiation. Thus the critical clearing time for this system is 0.545 seconds.

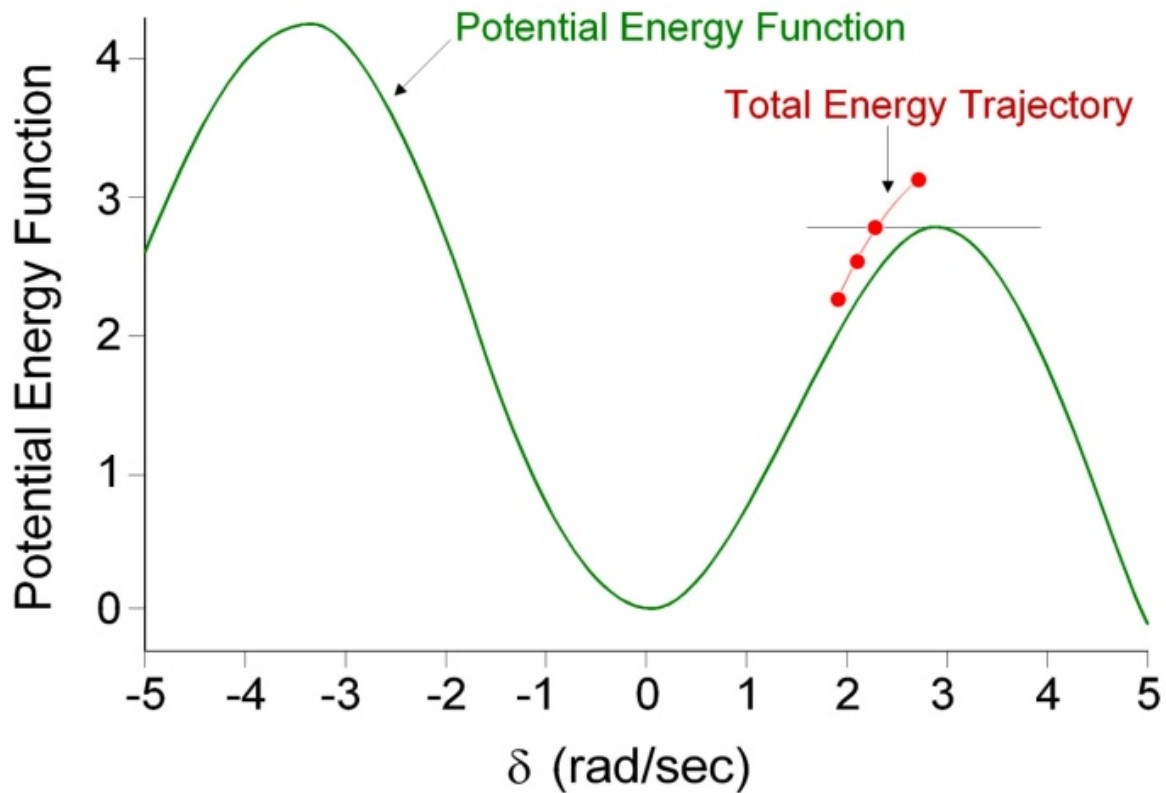


Figure 7.11: Test System Total Energy Trajectory

It is illustrated in Figure 7.9 that the total energy is below the maximum value of the system's potential energy, thus the system is stable, whereas for the second case the total energy is greater than the maximum value of the system's potential energy, and thus the system is unstable.

As a result, we presented an energy method based on the Lyapunov function of the system, from which we can evaluate whether the system is going to be driven out of synchronism or not, providing an out-of-step relay protection scheme. Note that only the post fault system equilibrium points have been used, along with the system trajectory (as it is obtained by the dynamic state estimator) during the fault phase, and in particular the state values at the fault clearing instant. No dynamic information and data of the post fault system are necessary.

The methodology described previously can be extended and applied in actual power systems. In particular, the dynamic state estimator provides the center of oscillation of the actual system, and the swing equation of a generator can be evaluated in terms of the center of oscillation. Thus the methodology can be applied to each generating unit individually no matter how many units exist in the system. Figure 7.12 illustrates visualization and comparison of the Impedance Trajectory based Out of Step Relaying and the Proposed Generator Stability Monitoring Method.

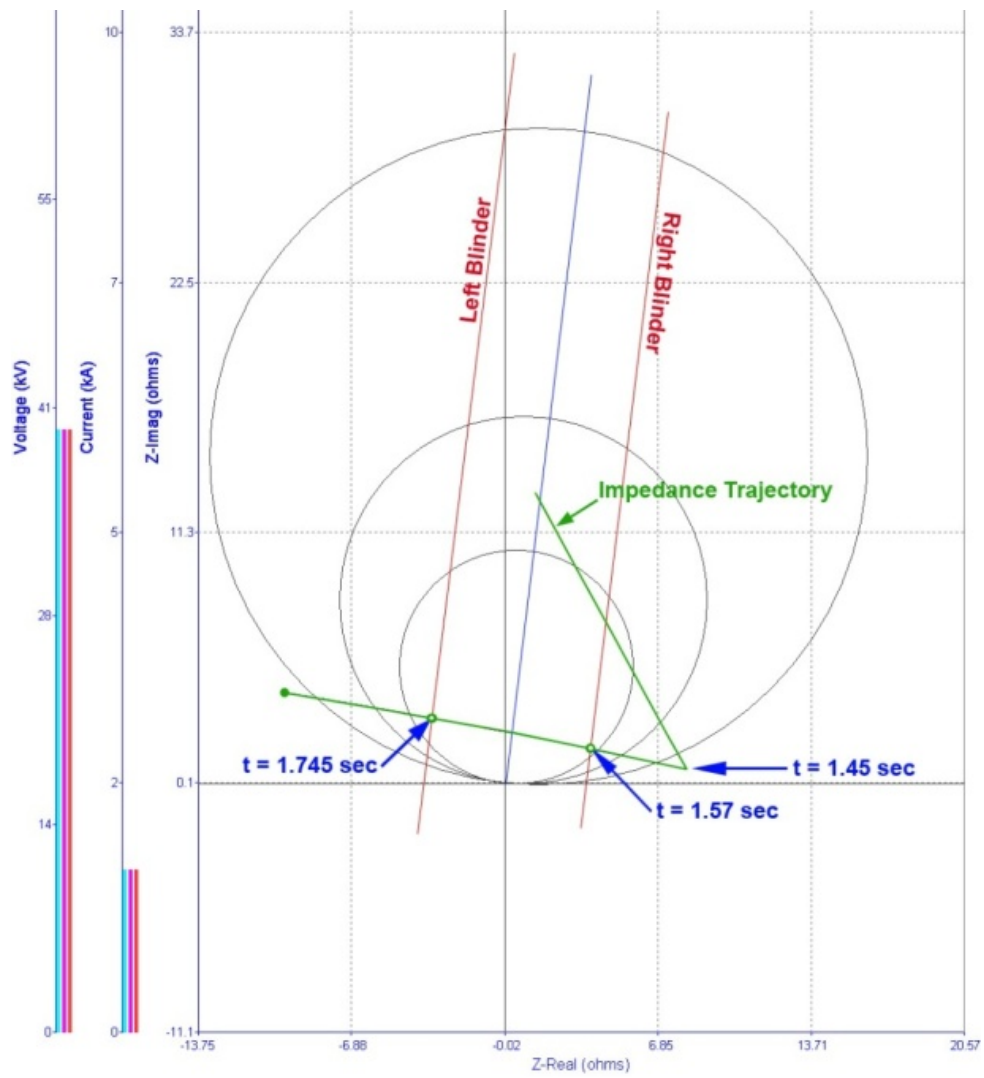


Figure 7.12: Visualization and Comparison of the Impedance Trajectory

8.0 Conclusion

Visualization has, and will continue to play an important role in the safe and reliable operation of large scale power systems. This research project has 1) developed a new method for visualization of such systems through its introduction of geographic data views, 2) introduced two new algorithms to reduce the time needed to produce power system controls, 3) provided new algorithms and insights on the use of phasor measurement unit data, and 4) provided insight and analysis in the human factors aspects of power system visualization. Clearly much has been accomplished.

Nevertheless, significant challenges remain. Certainly we have just scratched the surface with respect to how the geographic data view concept can be applied to power system visualizations. More research is needed to more fully develop and demonstrate this approach. The use of the parallel processing power of the graphics processing units (GPUs) has just begun to be exploited. While this project demonstrated how the GPU can be used to significantly increase contouring performance, there are probably other power system applications as well. The application of PMUs data for on-line operations is certainly still in its infancy with several other uses still waiting to be discovered. Finally, the application of human factor techniques to power system visualization continues to be an area rich in research potential. Hence while we believe this project has been a success, more research is certainly needed to continue moving forward.

Appendix A: Basic Problem in Dynamic State Estimation

A basic problem in dynamic state estimation is to develop the mathematical model of synchronized measurements in one end of the line in terms of the dynamic state of the system at the two ends of the line. The solution of this problem provides estimates of the dynamic states of the system at the remote end of a transmission circuit from local information, thus avoiding the need for communications and the usual time latencies associated with the communication scheme. This appendix describes this problem. The problem is simplified to one simple single phase transmission line. It is assumed that PMU measurements are taken at one end of the line. The algorithm provides the relationship of all the local measurements to the dynamic states at both ends of the line. It is important to note that this model/algorithm is incorporated within the overall estimation algorithm of the SuperCalibrator.

A.1 Description of the transmission line model

The model of the transmission line is illustrated by Figure A.1.

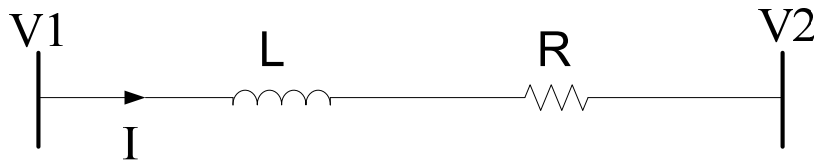


Figure A.1: The Transmission Line Model

The transmission line model is described by the following equations:

$$\begin{cases} Ri_{12a}(t) + L \frac{di_{12a}(t)}{dt} = V_1(t) \cos[w_s t + \delta_1(t) + \varphi_1] - V_2(t) \cos[w_s t + \delta_2(t) + \varphi_2] \\ i_{12a}(t) = I(t) \cos[w_s t + \delta(t) + \varphi] \end{cases}$$

So by substituting the second equation in to the first equation and define several internal variables, we will have the following model,

$$\left\{ \begin{array}{l} RI(t) + L \frac{dI(t)}{dt} c(t) + LI(t)s(t)(w_s + w(t)) = V_1(t)c_1(t) - V_2(t)c_2(t) \\ \frac{d c(t)}{dt} = -s(t)(w_s + w(t)) \\ \frac{d c_1(t)}{dt} = -s_1(t)(w_s + w_1(t)) \\ \frac{d c_2(t)}{dt} = -s_2(t)(w_s + w_2(t)) \\ \frac{d s(t)}{dt} = c(t)(w_s + w(t)) \\ \frac{d s_1(t)}{dt} = c_1(t)(w_s + w_1(t)) \\ \frac{d s_2(t)}{dt} = c_2(t)(w_s + w_1(t)) \\ \frac{d \delta(t)}{dt} = w(t) \\ \frac{d \delta_1(t)}{dt} = w_1(t) \\ \frac{d \delta_2(t)}{dt} = w_2(t) \end{array} \right.$$

Where we have define,

$$\left\{ \begin{array}{l} c(t) = \cos[w_s t + \delta(t) + \varphi] \\ s(t) = \sin[w_s t + \delta(t) + \varphi] \\ c_1(t) = \cos[w_s t + \delta_1(t) + \varphi_1] \\ s_1(t) = \sin[w_s t + \delta_1(t) + \varphi_1] \\ c_2(t) = \cos[w_s t + \delta_2(t) + \varphi_2] \\ s_2(t) = \sin[w_s t + \delta_2(t) + \varphi_2] \end{array} \right.$$

A.2 States definition and Measurements definition

We have the measurements as following:

$V_1^m(t)$: magnitude measurement of voltage $V_1(t)$

$\varphi_{V_1}^m(t)$: phase measurement of voltage $V_1(t)$

$w_1^m(t)$: frequency measurement of voltage $V_1(t)$

$\alpha_1^m(t)$: change ratio of the frequency of voltage $V_1(t)$

$I^m(t)$: magnitude measurement of current on line 1-2

$\varphi_I^m(t)$: phase measurement of current on line 1-2

$w_l^m(t)$: frequency measurement of current on line 1-2

$\alpha_l^m(t)$: change ratio of the frequency of current on line 1-2

The state is defined with:

$$X^T = [X_1^T \ X_2^T \ X_l^T]$$

with

$$X_1^T = [V_1(t), \ w_1(t), \ \delta_1(t), \ c_1(t), \ s_1(t)]$$

$$X_2^T = [V_2(t), \ w_2(t), \ \delta_2(t), \ c_2(t), \ s_2(t)]$$

$$X_g^T = [I(t), \ w(t), \ \delta(t), \ c(t), \ s(t)]$$

A.3 Estimation model

The estimation problem is defined in terms of 15 states as follows:

The system states is

$$X^T = [X_1^T \ X_2^T \ X_l^T]$$

with

$$X_1^T = [V_1(t), \ w_1(t), \ \delta_1(t), \ c_1(t), \ s_1(t)]$$

$$X_2^T = [V_2(t), \ w_2(t), \ \delta_2(t), \ c_2(t), \ s_2(t)]$$

$$X_g^T = [I(t), \ w(t), \ \delta(t), \ c(t), \ s(t)]$$

The estimation model is as following. Please notice that the left side of the equation is a value, whether a measured value or a estimated value from the former steps while the right side of the equation is an expression of the state variables. Please also notice that if the at the end of the right side of the equation there is an error η , it means this equation represents a actual measurement and otherwise it is a pseudo measurement.

$$V_1^m(t) = V_1(t) + \eta$$

$$\cos(\phi_{V_1}^m(t)) = c_1(t) + \eta$$

$$\sin(\phi_{V_1}^m(t)) = s_1(t) + \eta$$

$$w_1^m(t) = w_1(t) + \eta$$

$$\frac{h}{6} \alpha_1^m(t) + \frac{2h}{3} \alpha_1^m(t_m) + \frac{h}{6} \alpha_1(t-h) + w_1(t-h) = w_1(t) + \eta$$

$$-\frac{h}{24} \alpha_1^m(t) + \frac{h}{3} \alpha_1^m(t_m) + \frac{5h}{24} \alpha_1(t-h) + w_1(t-h) = w_1(t_m) + \eta$$

$$I^m(t) = I(t) + \eta$$

$$\begin{aligned}
\cos(\varphi_I^m(t)) &= c(t) + \eta \\
\sin(\varphi_I^m(t)) &= s(t) + \eta \\
w_I^m(t) &= w(t) + \eta \\
\frac{h}{6} \alpha_I^m(t) + \frac{2h}{3} \alpha_I^m(t_m) + \frac{h}{6} \alpha_I(t-h) + w(t-h) &= w(t) + \eta \\
-\frac{h}{24} \alpha_I^m(t) + \frac{h}{3} \alpha_I^m(t_m) + \frac{5h}{24} \alpha_I(t-h) + w(t-h) &= w(t_m) + \eta \\
R \frac{h}{6} I(t-h)c(t-h) - LI(t-h)c(t-h) - L \frac{h}{6} I(t-h)s(t-h)(w_s + w(t-h)) - \frac{h}{6} V_1(t-h)c_1(t-h) + \frac{h}{6} V_2(t-h)c_2(t-h) \\
&= \frac{h}{6} V_1(t)c_1(t) - \frac{h}{6} V_2(t)c_2(t) - (R \frac{h}{6} + L)I(t)c(t) + L \frac{h}{6} I(t)s(t)(w_s + w(t)) \\
&\quad + \frac{2h}{3} V_1(t_m)c_1(t_m) - \frac{2h}{3} V_2(t_m)c_2(t_m) - R \frac{2h}{3} I(t_m)c(t_m) + L \frac{2h}{3} I(t_m)s(t_m)(w_s + w(t_m)) \\
\left[c_1(t-h) - \frac{h}{6} s_1(t-h)(w_s + w_1(t-h)) \right] &= c_1(t) + \frac{h}{6} s_1(t)(w_s + w_1(t)) + \frac{2h}{3} s_1(t_m)(w_s + w_1(t_m)) \\
\left[c_2(t-h) - \frac{h}{6} s_2(t-h)(w_s + w_2(t-h)) \right] &= c_2(t) + \frac{h}{6} s_2(t)(w_s + w_2(t)) + \frac{2h}{3} s_2(t_m)(w_s + w_2(t_m)) \\
\left[s_1(t-h) + \frac{h}{6} c_1(t-h)(w_s + w_1(t-h)) \right] &= s_1(t) - \frac{h}{6} c_1(t)(w_s + w_1(t)) - \frac{2h}{3} c_1(t_m)(w_s + w_1(t_m)) \\
\left[s_2(t-h) + \frac{h}{6} c_2(t-h)(w_s + w_2(t-h)) \right] &= s_2(t) - \frac{h}{6} c_2(t)(w_s + w_2(t)) - \frac{2h}{3} c_2(t_m)(w_s + w_2(t_m)) \\
\left[\delta_1(t-h) + \frac{h}{6} w_1(t-h) \right] &= \delta_1(t) - \frac{h}{6} w_1(t) - \frac{2h}{3} w_1(t_m) \\
\left[\delta_2(t-h) + \frac{h}{6} w_2(t-h) \right] &= \delta_2(t) - \frac{h}{6} w_2(t) - \frac{2h}{3} w_2(t_m) \\
\left[c(t-h) - \frac{h}{6} s(t-h)(w_s + w(t-h)) \right] &= c(t) + \frac{h}{6} s(t)(w_s + w(t)) + \frac{2h}{3} s(t_m)(w_s + w(t_m)) \\
\left[s(t-h) + \frac{h}{6} c(t-h)(w_s + w(t-h)) \right] &= s(t) - \frac{h}{6} c(t)(w_s + w(t)) - \frac{2h}{3} c(t_m)(w_s + w(t_m)) \\
\left[\delta(t-h) + \frac{h}{6} w(t-h) \right] &= \delta(t) - \frac{h}{6} w(t) - \frac{2h}{3} w(t_m) \\
R \frac{5h}{24} I(t-h)c(t-h) - LI(t-h)c(t-h) - L \frac{5h}{24} I(t-h)s(t-h)(w_s + w(t-h)) - \frac{5h}{24} V_1(t-h)c_1(t-h) + \frac{5h}{24} V_2(t-h)c_2(t-h) \\
&= -\frac{h}{24} V_1(t)c_1(t) + \frac{h}{24} V_2(t)c_2(t) + R \frac{h}{24} I(t)c(t) - L \frac{h}{24} I(t)s(t)(w_s + w(t)) - LI(t_m)c(t_m) \\
&\quad + \frac{h}{3} V_1(t_m)c_1(t_m) - \frac{h}{3} V_2(t_m)c_2(t_m) - R \frac{h}{3} I(t_m)c(t_m) + L \frac{h}{3} I(t_m)s(t_m)(w_s + w(t_m))
\end{aligned}$$

$$\begin{aligned}
\left[c_1(t-h) - \frac{5h}{24} s_1(t-h)(w_s + w_1(t-h)) \right] &= c_1(t_m) - \frac{h}{24} s_1(t)(w_s + w_1(t)) + \frac{h}{3} s_1(t_m)(w_s + w_1(t_m)) \\
\left[c_2(t-h) - \frac{5h}{24} s_2(t-h)(w_s + w_2(t-h)) \right] &= c_2(t_m) - \frac{h}{24} s_2(t)(w_s + w_2(t)) + \frac{h}{3} s_2(t_m)(w_s + w_2(t_m)) \\
\left[s_1(t-h) + \frac{5h}{24} c_1(t-h)(w_s + w_1(t-h)) \right] &= s_1(t_m) + \frac{h}{24} c_1(t)(w_s + w_1(t)) - \frac{h}{3} c_1(t_m)(w_s + w_1(t_m)) \\
\left[s_2(t-h) + \frac{5h}{24} c_2(t-h)(w_s + w_2(t-h)) \right] &= s_2(t_m) + \frac{h}{24} c_2(t)(w_s + w_2(t)) - \frac{h}{3} c_2(t_m)(w_s + w_2(t_m)) \\
\left[\delta_1(t-h) + \frac{5h}{24} w_1(t-h) \right] &= \delta_1(t_m) + \frac{h}{24} w_1(t) - \frac{h}{3} w_1(t_m) \\
\left[\delta_2(t-h) + \frac{5h}{24} w_2(t-h) \right] &= \delta_2(t_m) + \frac{h}{24} w_2(t) - \frac{h}{3} w_2(t_m) \\
\left[c(t-h) - \frac{5h}{24} s(t-h)(w_s + w(t-h)) \right] &= c(t_m) - \frac{h}{24} s(t)(w_s + w(t)) + \frac{h}{3} s(t_m)(w_s + w(t_m)) \\
\left[s(t-h) + \frac{5h}{24} c(t-h)(w_s + w(t-h)) \right] &= s(t_m) + \frac{h}{24} c(t)(w_s + w(t)) - \frac{h}{3} c(t_m)(w_s + w(t_m)) \\
\left[\delta(t-h) + \frac{5h}{24} w(t-h) \right] &= \delta(t_m) + \frac{h}{24} w(t) - \frac{h}{3} w(t_m)
\end{aligned}$$

Appendix B: Triangulation Methods for Visualization of Power System Data

The visualization of various quantities of a transmission grid is achieved by rendering a smooth 3D interpolated surface. The surface can be rendered as a smooth surface (Figure B.3), 3D IsoSurface (Figure B.4), or a 2D IsoSurface (Figure B.5). (Figure B.1 is Bounded Butterfly subdivision. Note that the height of the new vertices is contained within the original vertices). The complete algorithm is outlined below. Experimentation with these algorithms shows an effective and efficient methodology using triangulation techniques. The methods have been used for the visualizations in the main body of the report. Here we present the algorithms with examples of their performance.

Input consists of the x, z locations of the sites where readings are available. At each of these sites the corresponding voltages are available. These are represented by the y coordinate for the sites.

- i) Perform a 2D Delaunay triangulation of the sites using only the x, z coordinates and generate a triangle mesh 'M'. Each site is represented by a vertex in this mesh.
- ii) Update the mesh M with the 'y' coordinates of the corresponding sites to get a rough 3D triangulated surface.
- iii) Use the butterfly subdivision to add interpolated vertices in the triangle mesh. Implemented naively the inserted vertices may be above or below the vertices from which it is interpolated. This would be misleading so we bound location of the new vertex within the minimum and maximum of the vertices from which it was interpolated.
- iv) Apply the smoothing using the tuck operation as described earlier, but restrict it to the set of new vertices and keep the location of the original sites intact. Since we do not move the original sites we might see some discontinuity in the surface near the original sites. We fix this by tweaking the normals of the vertices adjacent to the original site. This is done by aligning the normals of the interpolated vertices with the normal of the original vertex which is adjacent to it. If the position of the interpolated vertices goes above or below the original vertices we clamp the position to the original vertex.
- v) We perform repeated subdivision and smoothing to get a visually pleasing 3d surface.

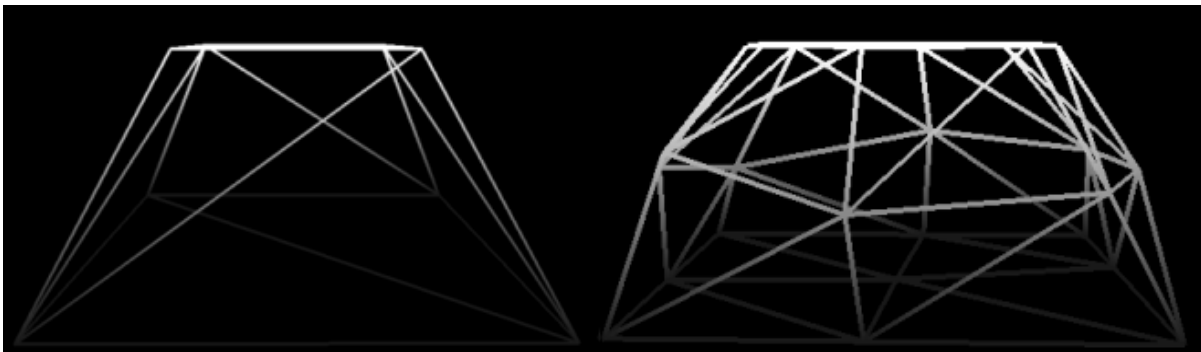


Figure B.1: Bounded Butterfly subdivision

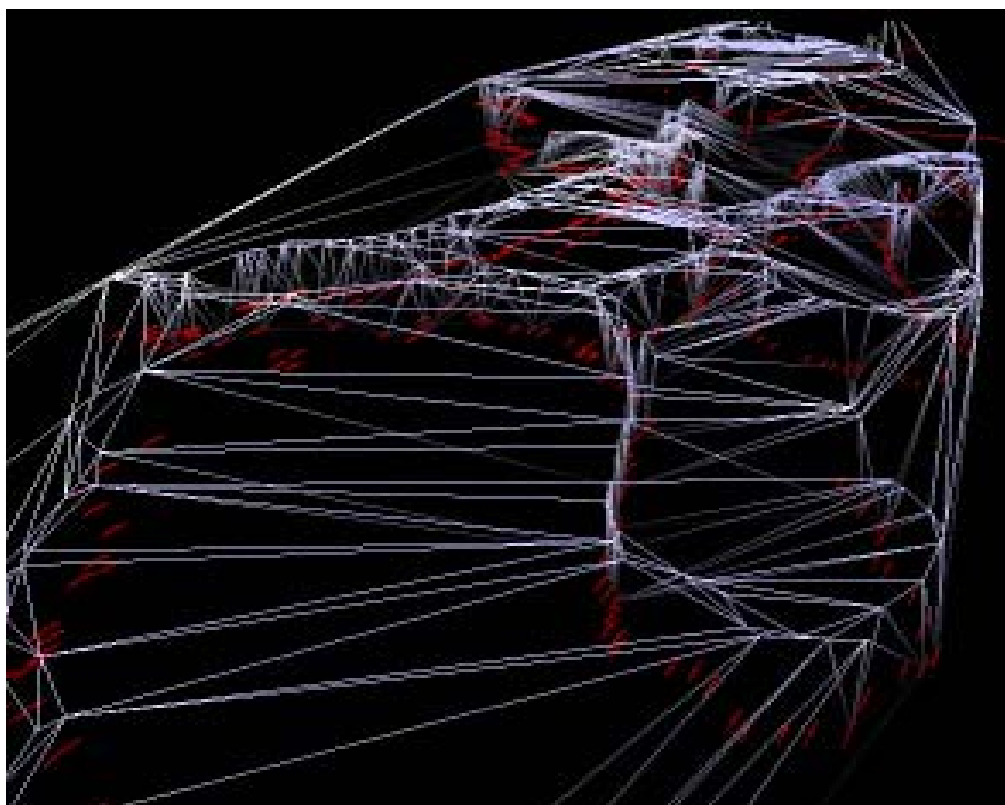


Figure B.2: Delaunay Triangulation of Points

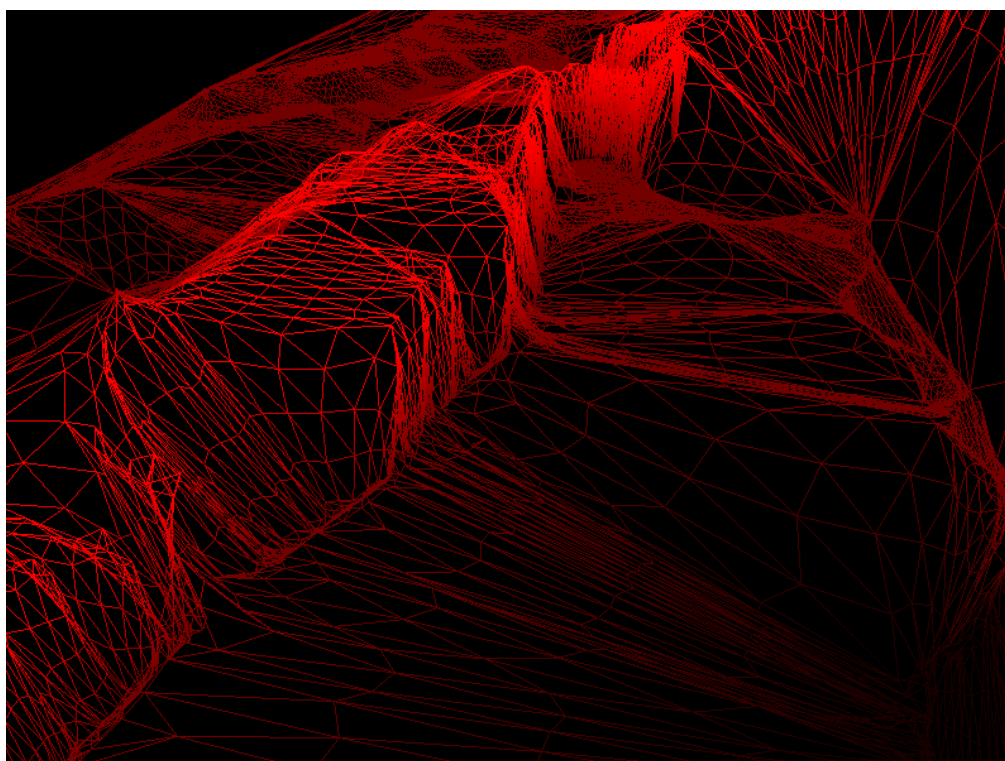


Figure B.3: After Bounded Butterfly subdivision and Smoothing

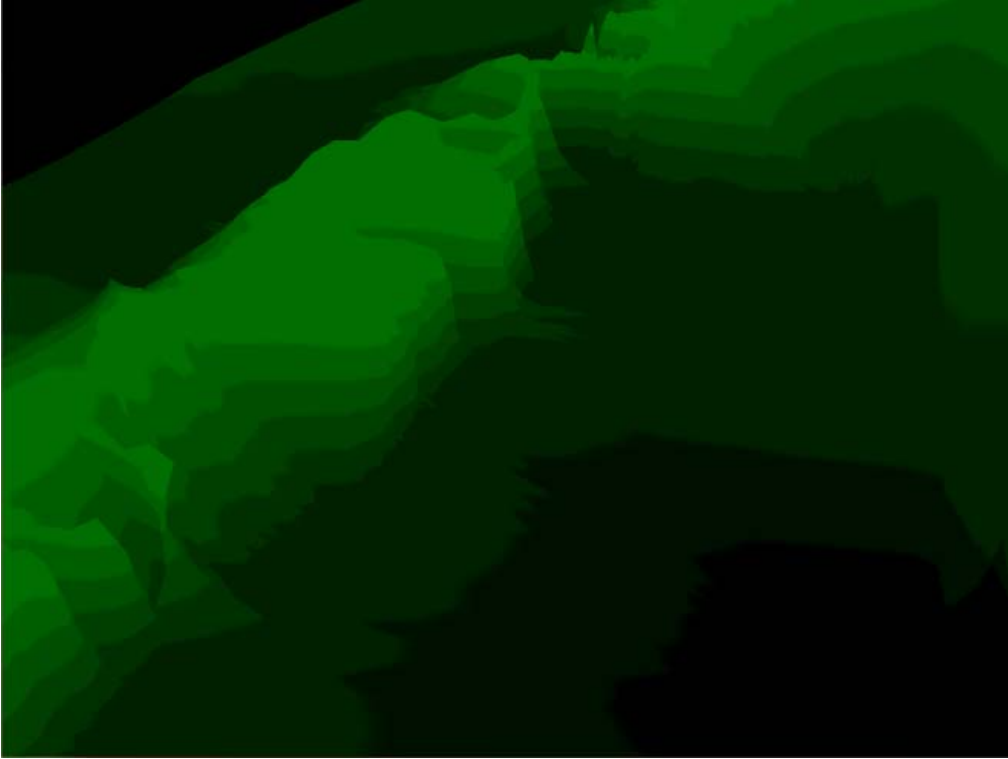


Figure B.4: 3D Iso-Surface with 8 levels

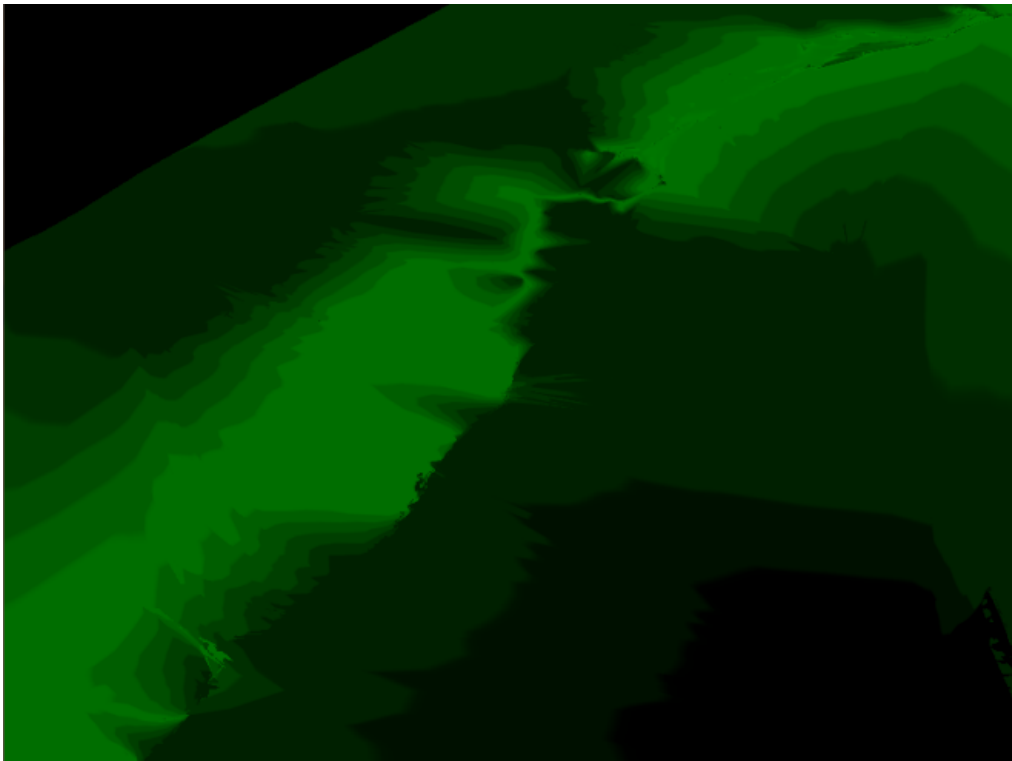


Figure B.5: Flat Iso-Surface with 8 levels

B.1 Rendering the IsoSurface

The smooth surface rendered in Figure B.2 might not be easy to comprehend though it is pleasing to the eye. We also show the surface as IsoSurface with different levels based on the height(voltage). Given the number of desired IsoSurface, we generate an OpenGL Texture which is mapped to the 3D triangle mesh surface to render the iso-surface. The texture map will have as many entries as there are isoSurfaces. The texture color at location 0,0 is the lowest IsoSurface and the color at location 1,0 is the highest IsoSurface color. Example for 8 IsoSurfaces we will have 8 different colors in the texture map. To map these colors to the surface and render the IsoSurface, the texture coordinate for a vertex is computed using its height ($=\text{vertexheight}/\text{MaxHeight}$). Ideally to generate the Iso-Surface we will have to compute the intersection of the IsoCurves with each of the triangle of the 3D mesh. But OpenGL texture mapping takes care of this for us if we set the correct texture mapping parameters. Example of the rendered IsoSurface is shown in Figures B.4 and B.5. Now we give the details of the steps described above.

B.2 Delaunay Triangulation

Given a set of planar points P, a Delaunay triangulation is a triangulation such that none of the triangle's circumscribing circle contains any point from P. Some nice properties of Delaunay triangulation are

- Compared to any other triangulation of the points, the smallest angle in the Delaunay triangulation is at least as large as the smallest angle in any other. Thus it maximizes the minimum angle of all the angles of the triangles in the triangulation. However, the Delaunay triangulation does not necessarily minimize the maximum angle.
- The triangulation is unique if no 4 points lie on the same circumcircle and no three points are on the same line. If 4 points lie on the same circle there can be multiple triangulations depending upon number of such occurrences in the point set P.
- It has at most $3n-6$ edges and at most $2n-5$ triangles.
- Efficient Algorithms exist to compute the Delaunay triangulation.

The incremental insertion algorithm of Delaunay triangulation in 2D is very popular due to its simplicity and stability. This algorithm repeatedly adds one vertex at a time and re-triangulates the affected triangles. The steps are outlined below.

- 1) Start with a triangle large enough to contain all the input points. Since this is the only triangle it satisfies the Delaunay property.
- 2) A new vertex 'P' is added to the existing Delaunay triangulation as follows:
 - i) Find the triangle which contains the new vertex V. Let the three points of the triangle be A,B,C. This can be done by starting from arbitrary triangle and moving in the direction of P.
 - ii) Delete the triangle ABC and create three new triangles which have the vertices as ABP, BCP and CAP.
 - iii) The edges of the old triangle ABC are inspected to verify that they still satisfy the empty circumcircle condition. If the condition is satisfied the edge remains intact. If

the condition is violated then the edge is flipped as shown in Figure B.6. Each flipping may result in two more edges becoming candidates for flipping. In worst case all edges have to be flipped. But usually if the vertices are inserted in a random order only a few edges get flipped.

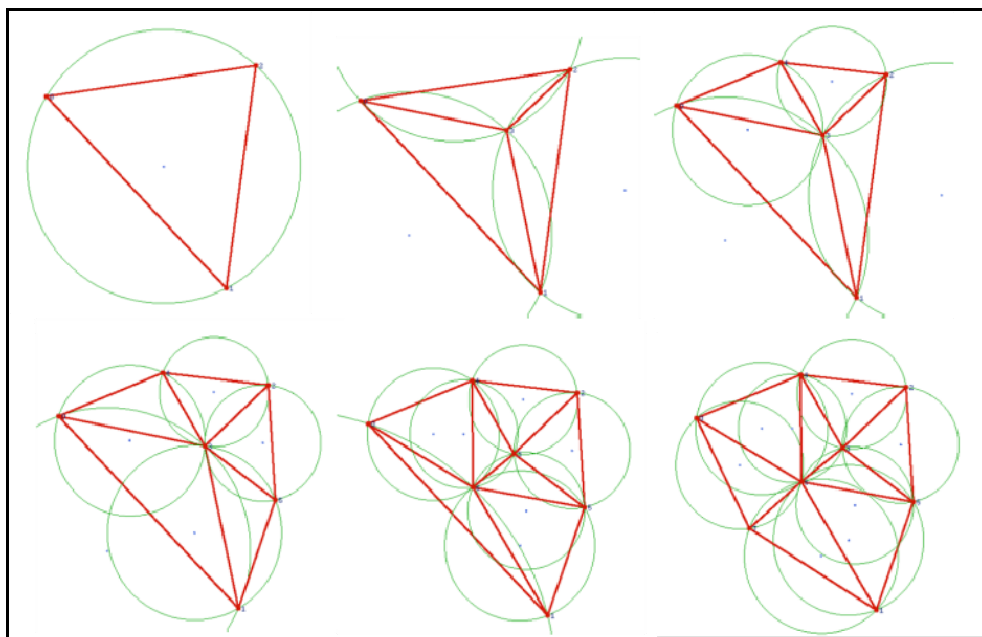


Figure B.6: Inserting points one-by-one

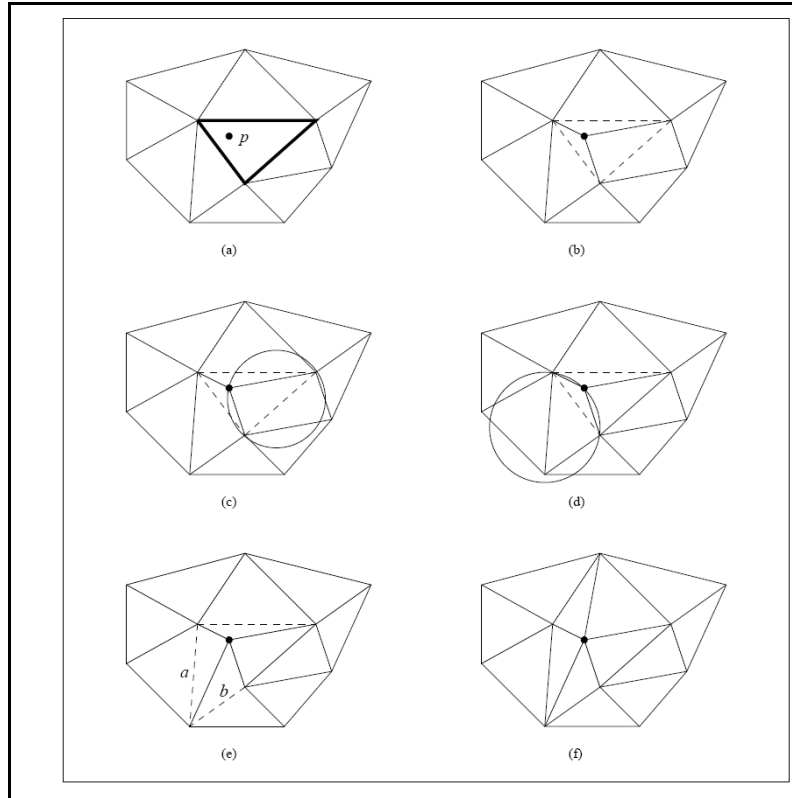


Figure B.7: Delaunay Triangulation - Inserting points

B.3 Data Structure used for the insertion algorithm

The Corner Table [1] provides a compact data structure to represent triangle meshes: A triangle mesh is defined by specifying the set G of its vertices and a set T of its triangles. A triangle is defined by the IDs of the three vertices that it interpolates. The V-table stores the vertex indices of G in sets of three. Each of these set represents a triangle. The association of a vertex with a triangle is denoted as a corner. So a triangle can be represented by choosing its corresponding three corners. The three corners of a triangle are stored in clockwise order. Given this ordering and a corner we can get the previous or next corner. Every triangle has three neighbors. The corner table captures this information in the 'O' (opposite) table. For every corner 'c' the corner 'o' of the neighboring triangle opposite to corner 'c' is stored. We use the following notation for the corner table implementation:

$G[]$: Stores vertex coordinates

$V[]$:(V-table):Stores triplets of indices forming a triangle. The corresponding vertex coordinates of the triangle can be accessed by using these three indices into G .

$O[]$:(O-table): Stores the opposite corner for every corner corresponding to V .

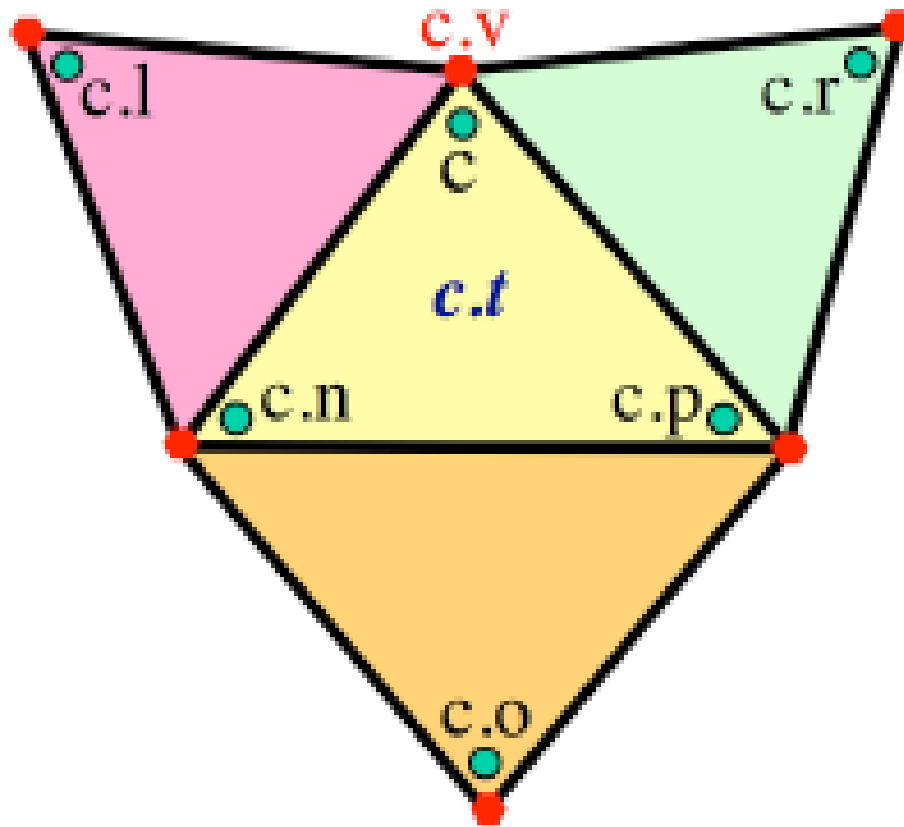


Figure B.8: Corner Table operations

Using the V and O tables, given a corner, c , we can access (See Figure B.7 - Inserting a point into the triangulation. Dashed lines indicate edges that need to be inspected. (e) is the result of flipping the dotted edge inside the circle in (d)).

$c.t$: its triangle.

$c.v$: its vertex

$c.p$: previous corners in $c.t$

$c.n$: next corner in $c.t$

$c.o$: opposite corner

$c.l$: left neighboring corner ($c.p.o$)

$c.r$: right neighboring corner ($c.n.o$)

The 2 main steps of the incremental algorithm are:

- i) Finding the triangle containing the newly inserted point
- ii) Create new triangles trivially and flip the edges if required to satisfy the Delaunay circumcircle criteria.

The corner table is very handy for the incremental Delaunay triangulation algorithm. The corner table provides an easy method to walk through the triangle mesh and access the connectivity information. We briefly discuss how to do the above two operations using the corner table.

B.4 Finding the triangle containing the new inserted point (see Figure B.8)

- i) Start from any arbitrary triangle. We need to reach triangle t_1 containing the point P which is to be inserted. (Figure B.8).
- ii) Make a line segment which starts inside triangle t_0 and ends at P (red line shown in Figure B.8). Let this be denoted as 'L'. Find the edge of t_0 which intersects the line segment 'L'. Let 'c' be the corner opposite to this edge.
- iii) Find the edge of t_0 which intersects the line segment 'L'. Let 'c' be the corner opposite to this edge.

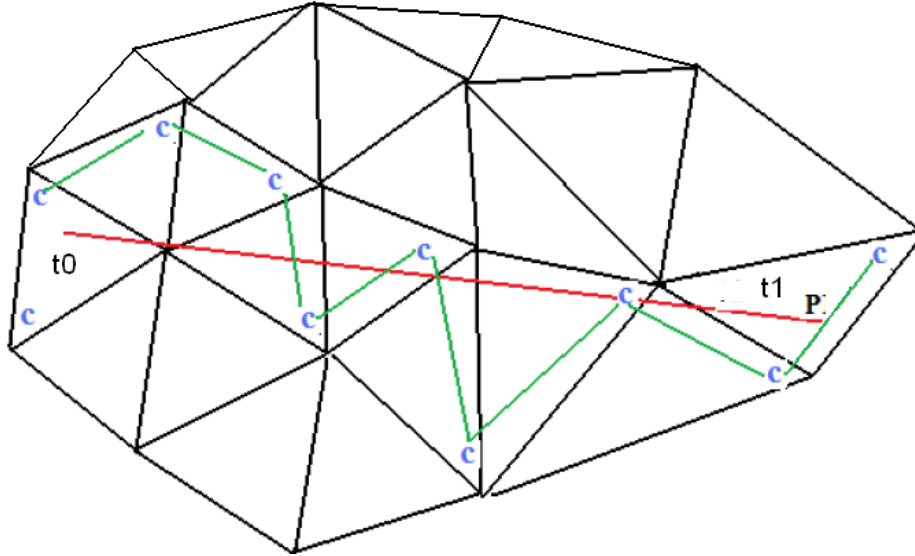


Figure B.9: Traversing the triangle mesh

- iv) $c = c.n$ (next corner) .
- v) if($g(v(c)).isLeftOf(L)$) .
 $c = c.r$; /*(o(n(c))) move to right triangle*/
else $c = c.l$; /*o(p(c)) move to left triangle*/
- vi) Check if $c.t$ contains the point P . If yes then we found the triangle containing P else repeat step v).
- vii) Figure B.2 - Traversing the triangle mesh using the corner table approach for locating the triangle containing the point to be inserted

B.5 Inserting the new point into an existing triangle

Figure B.10 shows the configuration of the corner table after inserting the new vertex. Addition of this new vertex results in addition of 9 new corners. Instead of deleting the old corners $c, c.p$ and $c.n$ we re-use them for one of the new triangles. (Inserting a point in an existing triangle. Three new triangles are added and the old triangle is deleted. The V-table and O-table are updated as show in the Figure B.10).

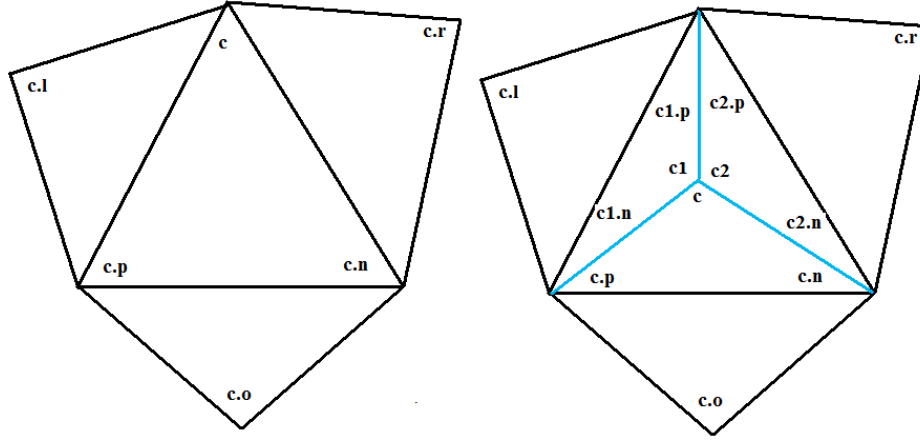


Figure B.10: Inserting a point in an existing triangle

B.6 Flipping an edge of the triangle

In Figure B.11, the red edge needs to be flipped. Corner 'c' is opposite to this red edge. The neighboring corners are marked using the operations on corner table described earlier. The result of flipping the edge is shown in the right configuration. The locations of the old corners are shown as well. (Flipping an edge using the corner table operators. The V-table and O-table are updated as show in the F).

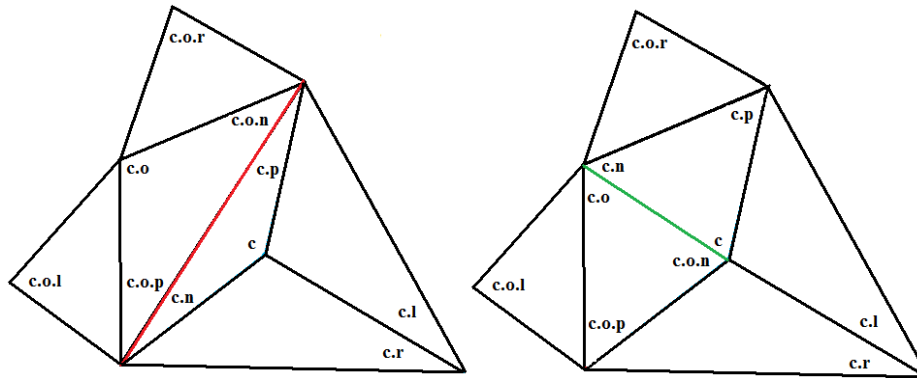


Figure B.11: Flipping a triangle edge using the corner table operators

B.7 Butterfly Subdivision

Once we have the triangulation of the points we use a customized butterfly subdivision scheme to subdivide the 3D surface. The main steps in the butterfly subdivision scheme are as follows:

- i) Insert a new vertex in the middle of each edge.
- ii) Split each triangle into 4 triangles
- iii) At each step, adjust the position of the new vertices, using the butterfly rule (See Figure B.12).

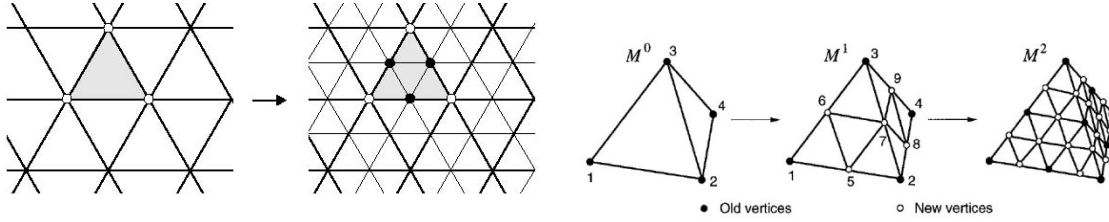


Figure B.12: Butterfly subdivision

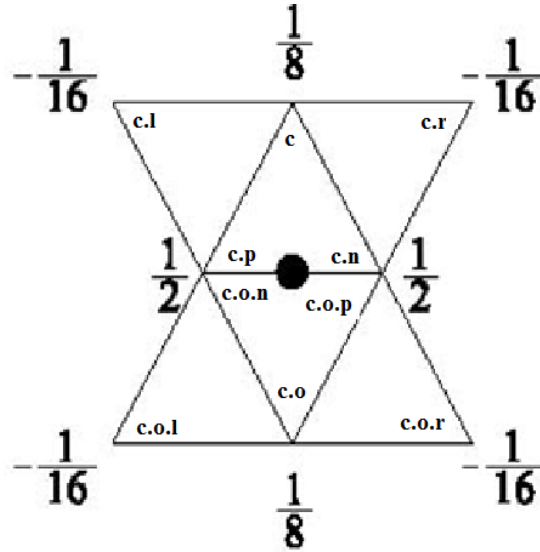


Figure B.13: Butterfly Mask

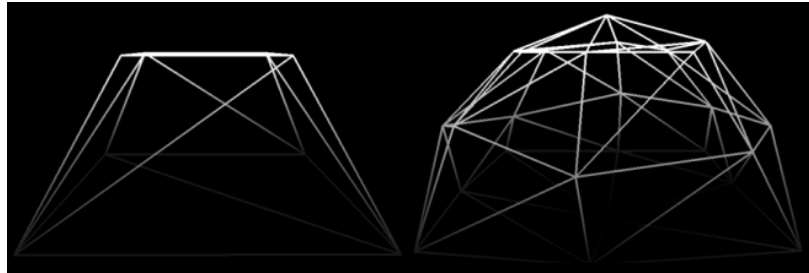


Figure B.14: Example butterfly subdivision

Though the butterfly subdivision attempts to produce smooth meshes we do not have control over the degree of smoothness. This is a problem because the introduced vertex might overshoot or undershoot the original vertices of the surface. For our purpose this can be misleading as the height can represent voltages. So we want the interpolated voltage to be contained within range of the original vertices. We modify the butterfly subdivision scheme by clamping the ‘y’ coordinates of the newly introduced vertices within the original vertices. (Figure B.13 - Butterfly Mask, the position of the new vertex (black dot) is calculated using the weights as shown in the Figure B.13).

B.8 Smoothing

We use the following smoothing scheme in addition to the butterfly subdivision to control the smoothness of the triangle mesh surfaces. We define an operation tuck as follows

tuck(s): displace each vertex by a fraction 's' of its normal.

The triangle meshed can be smoothed using the tuck operation by:

```
computeVertexNormals();  
tuck(0.6);  
computeVertexNormals();  
tuck(-0.6);
```

Project Publications

- [A] J. P. Stovall, B. J. Kirby, T. J. Overbye, J. S. Thorp, A. G. Phadke, "Issues Associated with the Development of a Wide-Area Analysis and Visualization Environment," accepted for presentation at 39th Hawaii International Conference on System Sciences, January 2006, Kauai, HI.
- [B] D. A. Wiegmann, T. J. Overbye, S. M. Hoppe, G. R. Essenberg, Y. Sun, "Human factors aspects of 3-dimensional visualizations of power system information," IEEE PES 2006 General Meeting, Montreal, Quebec, June 18-22, 2006.
- [C] G. J. Cokkinides, A. P. Meliopoulos, George Stefopoulos, Ramiz Alaileh and Apurva Mohan, "Visualization and Characterization of Stability Swings via GPS-Synchronized Data", *Proceedings of the of the 40st Annual Hawaii International Conference on System Sciences*, Kona, Hawaii, January 3-6, 2007.
- [D] D. O. Savageau, T. J. Overbye, "Adaptive influence distance algorithm for contouring bus-based power system data," *Proceedings of the of the 40st Annual Hawaii International Conference on System Sciences*, Kona, Hawaii, January 3-6, 2007.

References

- [1] T.J. Overbye, A.P. Meliopoulos, D.A. Wiegmann, G.J. Cokkinides, "Visualization of Power Systems and Components," PSERC Publication 05-65, November 2005; available online at http://www.pserc.org/ecow/get/publicatio/reports/2005report/overbye_visualization_final_report_sl8_2005.pdf
- [2] T.J. Overbye, D.A. Wiegmann, "Reducing the risk of major blackouts through improved power system visualization," *Proc. 2005 Power Systems Computational Conference (PSCC)*, Liege, Belgium, August 2005.
- [3] P. M. Mahadev and R. D. Christie, "Envisioning power system data: Concepts and a prototype system state representation," *IEEE Trans. Power Systems*, vol. 8, no. 3, pp. 1084-1090, Aug. 1993.
- [4] J. D. Weber and T. J. Overbye, "Voltage contours for power system visualization," *IEEE Trans. Power Systems*, vol. 15, no. 1, pp. 404-409, Feb. 2000.
- [5] D. Shepard, "A two-dimensional interpolation function for irregularly-spaced data," in *Proc. of the 23rd ACM National Conference*, New York, NY, 1969, pp. 517-523.
- [6] Boff, D. R., & Lincoln, J. E. (1988). *Engineering Data Compendium: Human Perception and Performance*. Wright-Patterson AFB, OH: AAMRL. <http://www.hsiiac.org>.
- [7] Wickens, C., Lee, J., Liu, Y., & Gordon-Becker, S. (2004). *An Introduction to Human Factors Engineering*, 2nd ed. Upper Saddle River, NJ: Pearson Prentice Hall
- [8] Cardosi, K. & Hannon, D. (1999). *Guidelines for the use of color in ATC displays* (DOT/FAA/AR-99/52). Washington, DC: Office of Aviation Research.
- [9] Xing, J. (2006). Color and visual factors in ATC displays (DOT/FAA/AM-06/15). Washington, DC: Office of Aerospace Medicine.
- [10] International Civil Aviation Organization (ICAO; 1993). *Human factors digest number 8: Human factors in air traffic control* (Circular 241-AN/145). Montreal, Canada: ICAO.
- [11] Vicente, K. J., & Rasmussen, J. (1992). Ecological interface design: Theoretical foundations. *IEEE Transactions on Systems, Man & Cybernetics*, SMC-22(4), 589-606.
- [12] Rasmussen, J. (1983). Skills, rules, knowledge: Signals, signs, and symbols and other distinctions in human performance models. *IEEE Transactions in Systems, Man, and Cybernetics*, SMC-13, 257-267.
- [13] Cardosi, K. M., & Murphy, E. D. (1995). *Human factors checklist for the design and evaluation of air traffic control systems*. DOT/FAA/RD-95/3.1, DOT-VNTSC-FAA-95-3.1. Washington, DC: Office of Aviation Research.
- [14] *McGraw-Hill Dictionary of Scientific and Technical Terms*. McGraw-Hill Companies, Inc., 2003.
- [15] Kirwan, B., & Ainsworth, L.K. (Ed.) (1992) *A Guide to Task Analysis*. London: Taylor & Francis.
- [16] A. P. Meliopoulos, G. J. Cokkinides, George K. Stefopoulos, "Quadratic Integration Method", *Proceedings of the 2005 International Power System Transients Conference (IPST 2005)*, p. xx (pp. x-x), Montreal, Canada, June 19-23, 2005.
- [17] A. P. Sakis Meliopoulos and G. J. Cokkinides, "Visualization and Animation of Instrumentation Channel Effects on DFR Data Accuracy", *Proceedings of the 2002 Georgia Tech Fault and Disturbance Analysis Conference*, Atlanta, Georgia, April 29-30, 2002.

- [18] T. K. Hamrita, B. S. Heck and A. P. Sakis Meliopoulos, 'On-Line Correction of Errors Introduced By Instrument Transformers In Transmission-Level Power Waveform Steady-State Measurements', *IEEE Transactions on Power Delivery*, Vol. 15, No. 4, pp 1116-1120, October 2000.
- [19] A. P. Sakis Meliopoulos and George J. Cokkinides, "Virtual Power System Laboratories: Is the Technology Ready?", *Proceedings of the 2000 IEEE/PES Summer Meeting*, Seattle, WA, July 16-20, 2000.
- [20] A. P. Sakis Meliopoulos and George J. Cokkinides, 'A Virtual Environment for Protective Relaying Evaluation and Testing', *Proceedings of the 34th Annual Hawaii International Conference on System Sciences*, p. 44 (pp. 1-6), Wailea, Maui, Hawaii, January 3-6, 2001.
- [21] A. P. Sakis Meliopoulos, George J. Cokkinides, "Visualization and Animation of Protective Relays Operation From DFR Data", *Proceedings of the 2001 Georgia Tech Fault and Disturbance Analysis Conference*, Atlanta, Georgia, April 30-May 1, 2001.
- [22] A. P. Meliopoulos and J. F. Masson, "Modeling and Analysis of URD Cable Systems," *IEEE Transactions on Power Delivery*, vol. PWRD-5, no. 2, pp. 806-815, April 1990.
- [23] G. P. Christoforidis and A. P. Sakis Meliopoulos, "Effects of Modeling on the Accuracy of Harmonic Analysis," *IEEE Transactions on Power Delivery*, vol. 5, no. 3, pp.1598-1607, July 1990.
- [24] A. P. Meliopoulos, F. Zhang, S. Zelingher, G. Stillmam, G. J. Cokkinides, L. Coffeen, R. Burnett, J. McBride, 'Transmission Level Instrument Transformers and Transient Event Recorders Characterization for Harmonic Measurements,' *IEEE Transactions on Power Delivery*, Vol 8, No. 3, pp 1507-1517, July 1993.
- [25] B. Fardanesh, S. Zelingher, A. P. Sakis Meliopoulos, G. Cokkinides and Jim Ingleson, 'Multifunctional Synchronized Measurement Network', *IEEE Computer Applications in Power*, Volume 11, Number 1, pp 26-30, January 1998.
- [26] A. P. Sakis Meliopoulos and G. J. Cokkinides, "Phasor Data Accuracy Enhancement in a Multi-Vendor Environment", *Proceedings of the 2005 Georgia Tech Fault and Disturbance Analysis Conference*, Atlanta, Georgia, April 25-26, 2005.
- [27] F. Darema, "Dynamic Data Driven Application Systems," Presentation at Purdue University, May 4, 2004, <http://www.cise.nsf.gov/eia/dddas>.
- [28] L. Tsoukalas, R. Gao, T. Fieno, X. Wang, "Anticipatory Regulation of Complex Power Systems," *Proc. of European Workshop on Intelligent Forecasting, Diagnosis and Control- IFDICON 2001*, Santorini, Greece, June 2001.
- [29] A.P. Sakis Meliopoulos and George J. Cokkinides, "A Virtual Environment for Protective Relaying Evaluation and Testing", *IEEE Transactions of Power Systems*, Vol. 19, No. 1, pp. 104-111, February, 2004.
- [30] Rossignac, Safonova, Szymczak 3D- Compression Made Simple: Edgebreaker on a Corner-Table.
- [31] P. Cignoniz, C. Montaniz, R. Scopigno, DeWall: A Fast Divide & Conquer Delaunay Triangulation Algorithm in E^d .
- [32] Wikipedia, the free encyclopedia, Delaunay triangulation, http://en.wikipedia.org/wiki/Delaunay_triangulation